ABSTRACT

Title of dissertation: SEARCH FOR NATURALLY OCCURRING SUPERCONDUCTIVITY AND NOVEL PHENOMENA: MAGNETIC TRANSITIONS IN NATURAL TRANSITION METAL COMPOUNDS

Renxiong Wang, Doctor of Philosophy, 2017

Dissertation directed by: Professor Johnpierre Paglione
Department of Physics

Transition metal chalcogenides and transition metal arsenides are important families of natural mineral compounds widely distributed in the natural world. With similar structural and electronic properties of transition metal oxides, natural transition metal compounds are expected to have similar novel phenomena. With an ongoing project for searching natural superconductors in collaboration with Department of Mineral Science, Smithsonian Institution, we had a chance to investigate several natural minerals from the Smithsonian Museum in order to study previously unexpected naturally occurring mineral compounds for interesting ground states.

We found several interesting magnetic transitions in these natural occurring mineral samples. Some of the magnetic transitions are not reported, some of the transitions are associated with other unreported novel quantum phenomena. In this thesis, I will discuss Bornite (Cu_5FeS_4), Berthierite ($FeSb_2S_4$), Nagyagite

($Pb_5Au(Te,Sb)_4S_{5-8}$), Maucherite ($Ni_{11}As_8$) and related experiments in detail.

Bornite (Cu_5FeS_4) has a semiconductor-insulator transition accompanied with an antiferromagnetic transition. As shown by our ability to tune the transition temperature and low-temperature metallicity by applying external pressure, Bornite may be a good candidate for Mott system and searching new superconductors.

Berthierite ($FeSb_2S_4$) is a quasi-1-dimensional antiferromagnet. With strong anisotropic physical properties, berthierite may provide a very good system for understanding the low dimensional magnetic material.

A Ferromagnetic order was found in natural nagyagite ($Pb_5Au(Te,Sb)_4S_{5-8}$) samples. The magnetic order, the weak anti-localization property with strong spin-orbital coupling and the 2-dimensional structure of this compound make it a very interesting system for realizing topological properties in a natural compound.

The magnetic order and transitions in both natural and synthetic maucherite ($Ni_{11}As_8$) samples show interesting finite-size scale effects. It gives us a different approach to understand the differences in some physical properties between natural and synthetic compounds.

Also, we will present a summary of other magnetic transitions and magnetic properties of more than 40 minerals for this study and show the relation and similarities between strongly correlated transition metal oxide materials and other quantum materials. We will also make a list of other transition metal minerals that are worthy of investigation based on our research experience.

SEARCH FOR NATURAL OCCURRING SUPERCONDUCTIVITY AND NOVEL PHENOMENA: MAGNETIC TRANSITIONS IN NATURAL TRANSITION METAL COMPOUNDS

by

Renxiong Wang

Dissertation submitted to the Faculty of the Graduate School of the
University of Maryland, College Park in partial fulfillment
of the requirements for the degree of
Doctor of Philosophy
2017

Advisory Committee:
Professor Johnpierre Paglione, Chair/Advisor
Professor Richard Greene
Professor Nicholas P. Butch
Professor Efrain Rodriguez
Professor Ichiro Takeuchi

Foreword

The results of my graduate studies have contributed to the following published works, with the publications/preprints that have portions represented in this thesis notified with an asterisk:

⋆ Renxiong Wang, Xiuquan Zhou, Kefeng Wang, I-Lin Liu, Tristin Metz, Shanta Saha, Jeff Post, Cara Santelli, Efrain E. Rodriguez,and Johnpierre Paglione "Anisotropic magnetization in natural quasi-one-dimension antiferromagnet: berthierite $FeSb_2S_4$," *pre-print*

⋆ Renxiong Wang, I-Lin Liu, Xiuquan Zhou, Kefeng Wang, Tristin Metz, Shanta Saha, Jeff Post, Cara Santelli, Efrain E. Rodriguez,and Johnpierre Paglione. "Suppression the antiferromagnetic insulating state by applying pressure to Bornite Cu_5FeS_4," *pre-print*

⋆ Renxiong Wang, Xiuquan Zhou, Kefeng Wang, Tristin Metz, Shanta Saha, Jeff Post, Cara Santelli, Efrain E. Rodriguez,and Johnpierre Paglione. "Magnetic and transport properties of 2D natural occurring mineral nagyagite $(Pb_5Au(Te,Sb)_4S_{5-8})$," *pre-print*

⋆ Renxiong Wang, Xiuquan Zhou, Kefeng Wang, Jeff Post, Cara Santelli, Efrain E. Rodriguez,and Johnpierre Paglione. "Potential size-dependent magnetic transition in natural maucherite $Ni_{11}As_8$," *pre-print*

Yasuyuki Nakajima, ⋆ Renxiong Wang, Tristin Metz, Xiangfeng Wang, Limin Wang, Hyunchae Cynn, Samuel T Weir, Jason R Jeffries, Johnpierre Paglione. "High-temperature superconductivity stabilized by electron-hole interband coupling

in collapsed tetragonal phase of KFe_2As_2 under high pressure," *Physical Review B* **91**, (6), 060508

Yasuyuki Nakajima, Rongwei Hu, Kevin Kirshenbaum, Alex Hughes, Paul Syers, Xiangfeng Wang, Kefeng Wang, ⋆ Renxiong Wang, Shanta R Saha, Daniel Pratt, Jeffrey W Lynn, Johnpierre Paglione. "Topological RPdBi half-Heusler semimetals: A new family of noncentrosymmetric magnetic superconductors," *Science advances* **1**, (5), e1500242

Yasuyuki Nakajima, Paul Syers, Xiangfeng Wang, ⋆ Renxiong Wang, Johnpierre Paglione. "One-dimensional edge state transport in a topological Kondo insulator," *Nature Physics* **12**, (3), 213-217

Dedication

To JP, to Jing, and to my parents for their support.

Acknowledgments

I would first like to thank my advisor Professor Johnpierre Paglione and Professor Richard Greene for their kind support. I still remember the first day I came to the Center for Nanophysics and Advanced Materials, JP showed me around and answered my questions patiently. The pleasant environment in JP's lab and this center breaks the boundaries between different disciplines so that I can learn from different people with diverse backgrounds to do my research.

I would like to thank Dr. Yasuyuki Nakajima now at UCF; he taught me a lot about low-temperature measurement techniques. Running the dilution fridge overnight and testing the systems, again and again, will be my precious memory. I would also like to thank Dr. Kefeng Wang and Dr. Shanta Saha; they show me a lot about crystal growth and I was enjoyed working on it. I also want to acknowledge the help from our collaborators Jeff Post and Cara Santelli from Smithsonian Institute who provided the excellent mineral samples, Xiuquan Zhou from Rodriguez group for his valuable discussion.

Also, I was so fortunate to work with a group of friendly and smart people for five years. The post-docs, Limin Wang, Xiangfeng Wang, Halyna Hodovanets, Hyunsoo Kim, were always very patient with teaching me and helping me. I was lucky to start with the graduate students, Kevin Kirshenbaum, Tyler Drye, Paul Syers and Steve Ziemak; I learned a lot with them. I appreciate the experience working with the graduate students, Connor Rongaioli, I-lin Liu, Tristin Metz, Chris Eckberg and Daniel Campbell; it was such a pleasant experience.

I would like to thank my parents. I have left my hometown for twelve years since high school; I cannot go that far without their endless support. I appreciate my father Kefeng Wang and my mother Yunhua Wang for getting me interested in engineering and science when I was young and their support and encouragement. Interestingly, my father's name has the same pronunciation with the name of my labmate Dr. Kefeng Wang but with different Chinese characters. My father's name means the 'mountain summit of science' and Dr. Wang's means 'blade of science' if they are translated directly from Chinese. I was lucky to have 'science' along with my life.

In the end, I want to express my appreciation to Jing Wang, and she changed my life.

Table of Contents

List of Tables

List of Figures

List of Abbreviations

CNAM	Center for Nanophysics and Advanced Materials
NIST	National Institute of Standards and Technology
TM	Transition metal
MIT	Metal insulator transition
FM	Ferromagnetic
AFM	Antiferromagnetic
PM	Paramagnetic

Chapter 1: Introduction

1.1 Smithsonian National Museum and Natural Superconductors

Discovering and understanding the properties of natural minerals has become part of human beings' history. In the pre-historical periods, our ancestors learned to use stones to make tools; and it made them a little bit different from other lives. Later they knew how to get bronze and metals from the rock to make better tools. Maybe at the same time, they also got some gems, silver, and gold for decoration, even found that they could make some colors and paints from the minerals, all these are about beauty, art, power, and treasures. Some ancient Chinese people made compass while playing with the mineral Magnetite, and later it was used to discovering the world. The steam engines were driven by the energy from coals hundreds of years ago. And now, we are not able to live in a world without products form the petroleum. A lot of discoveries in natural minerals has become milestones in the history of civilization.

A mineral is a naturally occurring chemical compound or material, usually of crystalline form and abiogenic in origin. A mineral has one specific chemical composition. In natural mineral samples from ores and rocks, the crystal quality can be as good as some beautiful single crystals like pyrite, gold, and some gems.

Also, it can be as bad as a rock of mixture of the primary phase and some impurities. Nowadays more than 5000 minerals are formally recognized on earth, and every year some new types of natural minerals are discovered by geologist and mineralogist, most of which were hidden in rocks for million years. They are classified into many classes according to the chemical composition. For example the native element minerals, sulfide minerals, sulfosalt minerals, organic minerals and so on. Most of them were studied with some traditional techniques in mineralogy and geophysics.

In mineralogy and mineral physics, most of the mineral samples are use to provide insights into plate tectonics, mantle convection and related phenomena. The structure and mechanical properties are studied in these areas. What if we look into the minerals with a view of modern condensed matter physicist by measuring their magnetic and electronic properties? First, most of the extreme condition properties (low temperature and high pressure) of minerals are not clear. Second, the mineral physicists or mineralogist may not think about the novel physical properties, like superconductivity and metal-insulator transition, of natural specimens. In the end, even we can synthesize a lot of samples in a lab; the formation of natural mineral samples still have a lot of differences with the techniques in lab considering the time, for instance, the high pressure and temperature from earth. Is it possible to discover some functional materials even new superconductors in the naturally occurring samples? With this idea and goal, we start a project about minerals to try to search superconductors in natural minerals in collaboration with Department of Mineral Science, Smithsonian National Museum of Nature and History. To have a better understanding of our plan and how we selected the mineral samples, an

introduction about the background and the project will be made in the first chapter.

Since our target is discovering a natural superconductor. I will first introduce some theoretical and experimental study about superconductivity and some reported natural mineral superconductors.

In 1911, Heike Kamerlingh Onnes reported a sudden drop in the electrical resistivity of mercury at 4.2 K, as shown in Figure 1.1. This phenomenon named as "Superconductivity" by Onnes, with a perfect diamagnetic state has been discovered many times while cooling down different materials.

Superconductivity has become one of the most important aspects of condensed matter physics. It has since been defined as a state of matter in which the resistivity of material drops to exactly zero and the material begins to show diamagnetic behavior at a critical temperature (T_c). In 1935, brothers Fritz and Heinz London developed the London equation to explain the superconducting state phenomenally [5]. Later another phenomenological model Ginzburg-Landau Theory, named after Vitaly Lazarevich Ginzburg and Lev Landau was proposed and could explain the superconducting phenomenon very well. In 1956, the BCS theory of superconductivity, named after John Bardeen, Leon N Cooper and John Robert Schrieffer was published, presenting a microscopic theoretical model for superconductors [6] and introduced the concepts of Cooper pairs. The BCS theory was such a success that can explain almost all the superconductivities before the 1980s. But, Alex Muller and Georg Bednorz, working at IBM in Switzerland, discovered the first cuprate superconductivity in Lanthanum barium copper oxide (LBCO) at 35K while looking for superconductivity in Jahn-Teller perovskites in 1986 [7]. In the next year, Paul

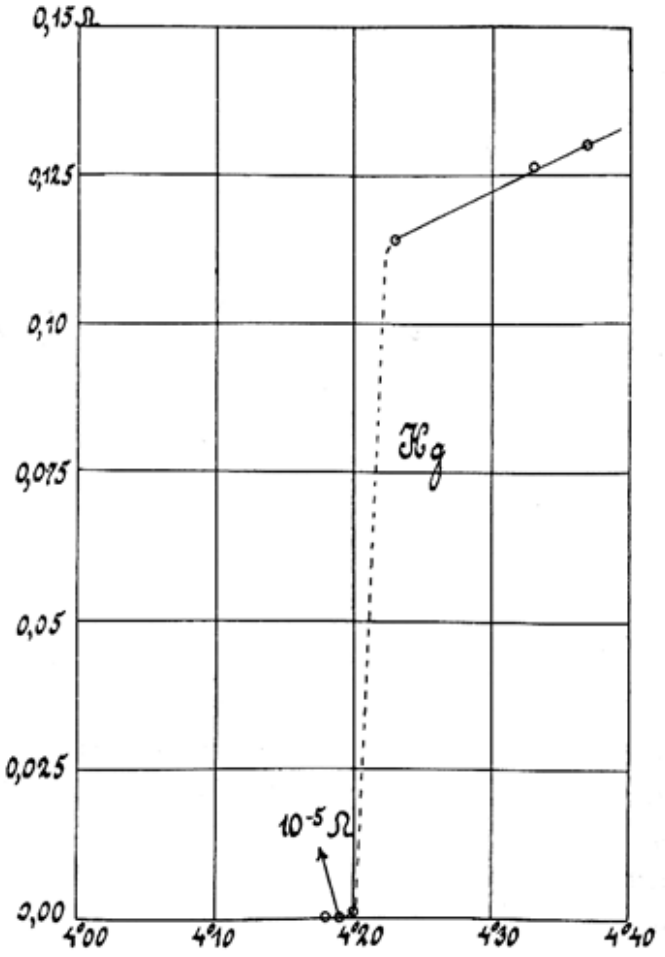

Figure 1.1: Superconducting transition at 4.2 K in Hg. The resistivity becomes zero at the transition temperature.

Chu's group in Houston first discovered superconductivity in Yttrium barium copper oxide (YBCO) with T_c above 77 K (boiling point of liquid nitrogen) [8]. However, these newly discovered superconductors (named cuprates due to the common CuO_2 plane structure in the materials) were found not follow the predictions of BCS theory which will be discussed in details in next part. These cuprates defined a new class of unconventional high-temperature superconductors. In 2006, another new class of superconductors, Fe-based superconductor, was discovered [9] while searching proper touchscreen materials. Figure 1.2 shows a graph of the highest known T_c as a function of the year of discovery. This new type of superconductors is based on conducting layers of iron and a pnictide instead of CuO_2 layers and doesnt follow the BCS theory either. The mechanism of these unconventional superconductors is still under debating, so it is still imperative to discover more superconductors for both understanding the superconductivity theory and future application. In this paper, we will discuss our attempts for searching new superconductors in natural mineral samples inspired by the experimental phenomena of these unconventional superconductors as well as other novel magnetic properties.

To search new superconductors, one approach is making new crystals in the lab; another way is to look at the existed compounds like minerals. The low-temperature characteristics of most of the natural mineral compounds are not well investigated. Also, in high-temperature superconductor cuprate and iron-based superconductor, the Cu-O and Fe-As layers play an essential role in the superconductivity. Most of the natural mineral compounds are chalcogenides and pnictides associated with transition metal elements which also have similar correlated struc-

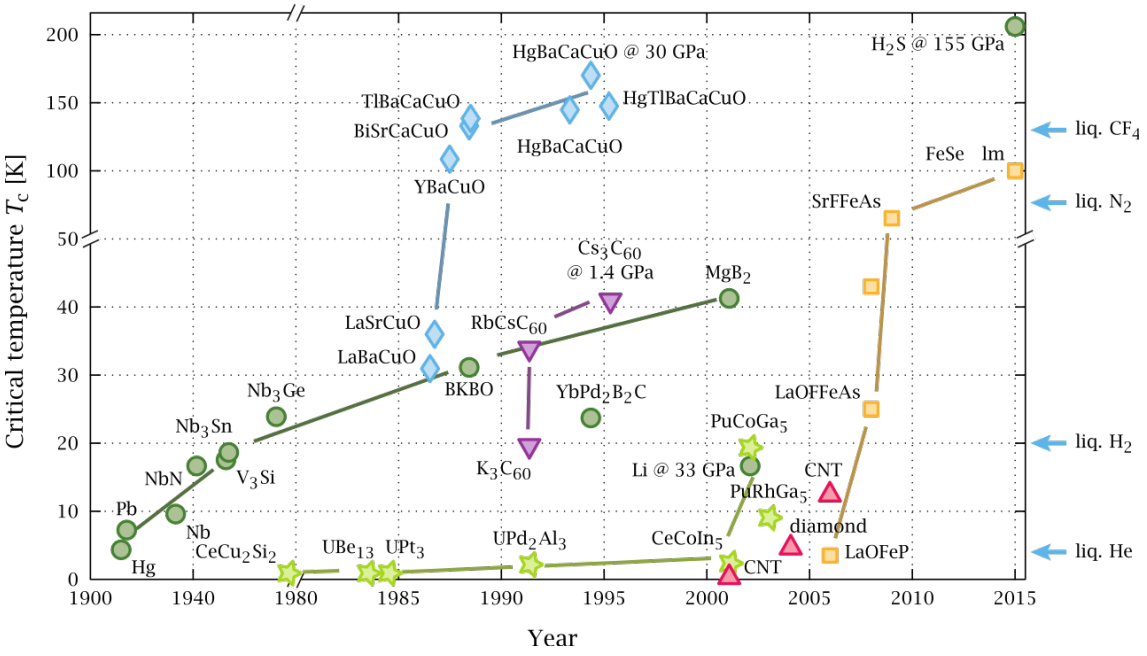

Figure 1.2: Timeline of superconductivity since 1911 (from Wikipedia).

tures of the transition metal atoms with O group and As group elements. With a lot of unknown properties and similar element composition, the transition metal chalcogenides and pnictides are worthy of being studied for searching new superconductors.

Several natural superconductors have been discovered in recent years. In 2006, Benedetto found the first natural superconductor covellite (CuS). An abrupt increase of the diamagnetic effect at 1.63 K (Figure 1.3) was observed in natural covellite samples from different countries while measuring the AC susceptibility with decreasing temperature, thus evidencing superconducting state [10]. The transition is field independent for low DC fields (smaller than 50 Oe), while cannot be observed for larger areas. These properties confirm natural covellite as a kind of type I superconductor. The structure of covellite at low temperature is composed of layered CuS_3

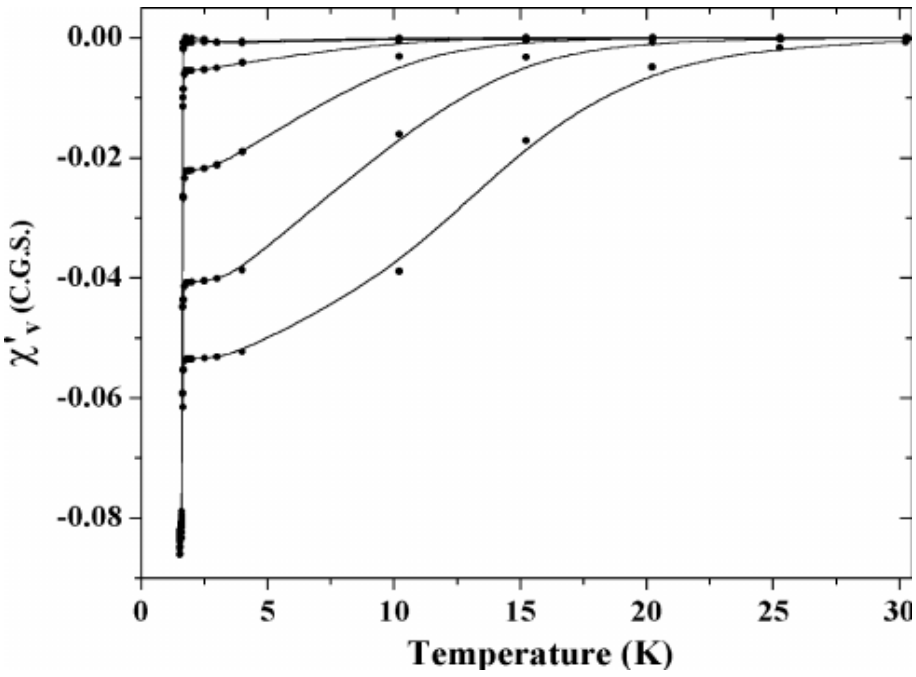

Figure 1.3: AC susceptibility measured in zero static field on covellite sample, in the range 1.5-30 K. The frequency ranges from 50 Hz (upper series) to 10 kHz (lower series); intermediate frequencies are 144, 416, 1201 and 3465 Hz.

planes connected by covalently bonded S_2 planes [10].

In 2009, miassite ($Rh_{17}S_{15}$) was reported as a strongly correlated superconductor with a superconducting transition temperature at 5.4 K [11]. Later the experiments were repeated in the lab made $Rh_{17}S_{15}$ with the same transition temperature, The heat capacity and resistivity experiment show that miassite is a strongly correlated superconductor. Based on the structure of miassite, researchers also tried to adjust the interaction by using Pd and Se atoms of the same element group to replace the Rh and S atoms. In these experiments, the researchers discovered a new multi-band superconductor $Pd_{17}Se_{15}$. The new material is the first superconductor born from the inspiration of natural superconductor.

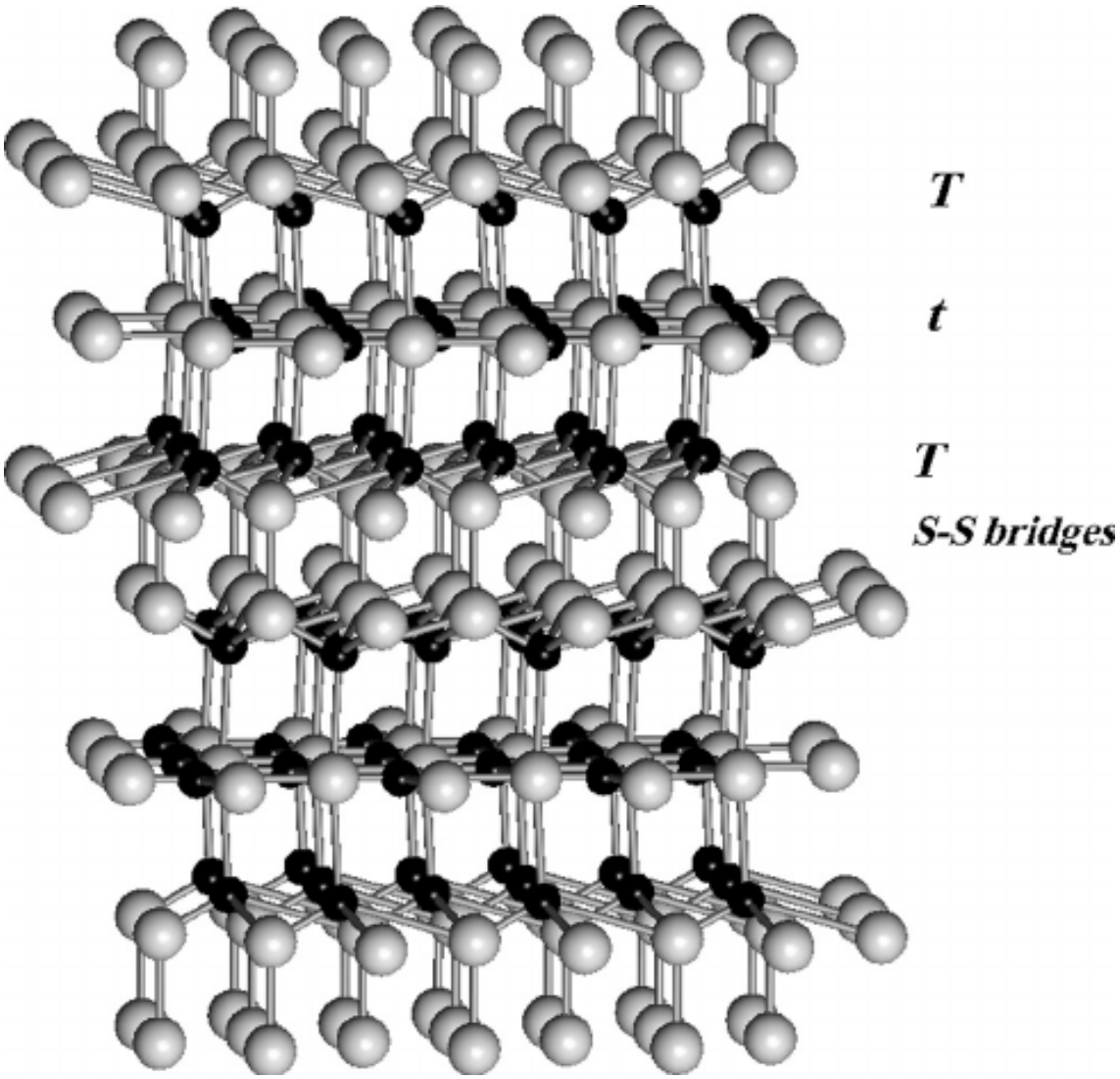

Figure 1.4: Low-temperature covellite structure (modified from Fjellvag's paper [4]). The T-t-T stacking sequences as well as the S-S bridges are evident. Grey and black spheres represent S and Cu ions respectively.

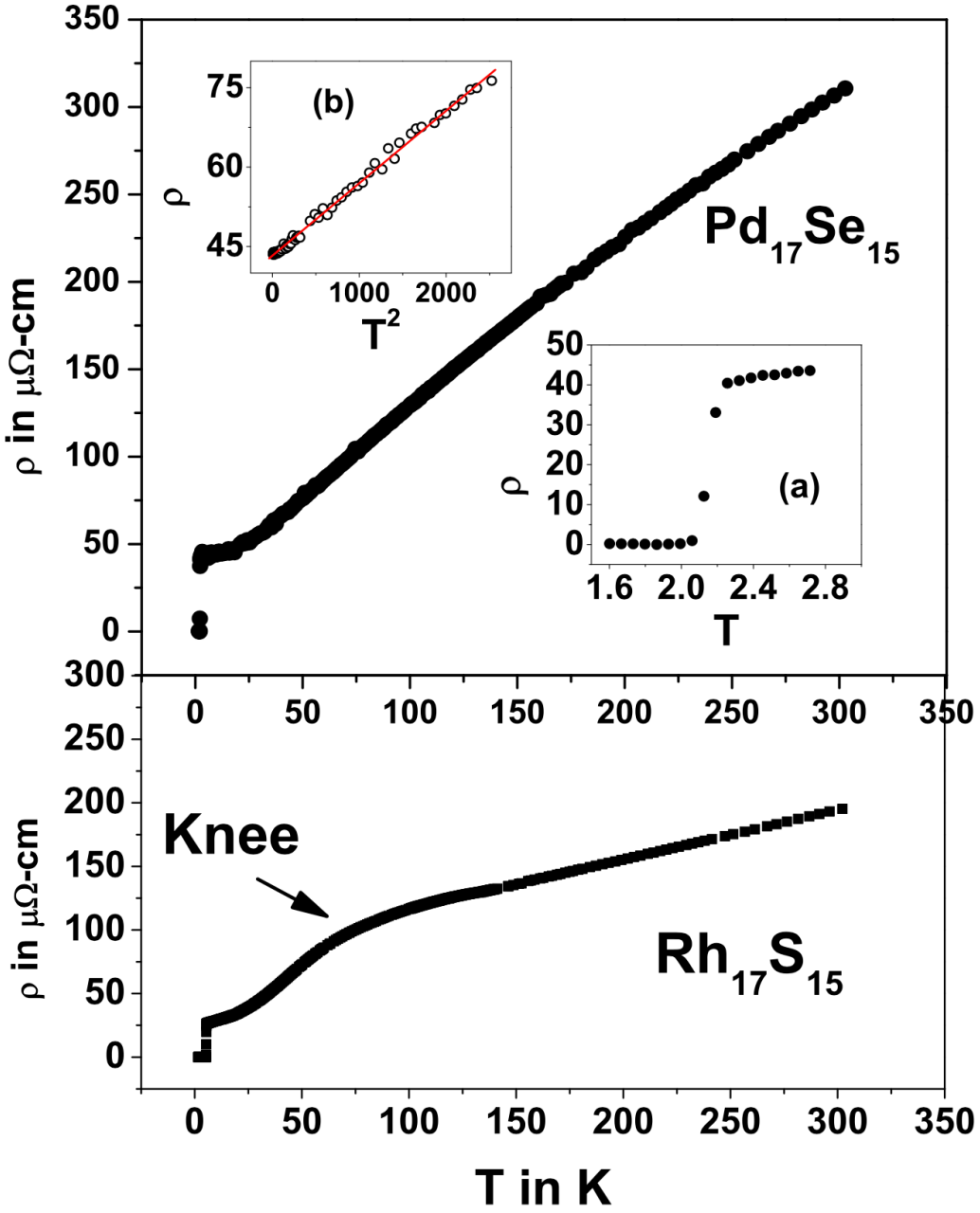

Figure 1.5: The temperature resistivity relation of miassite ($Rh_{17}S_{15}$) and $Rh_{17}Se_{15}$. Both of the two samples show superconductivity (Reference 8).

Both of the two natural superconducting minerals are transition metal sulfides, and most of the minerals in nature are sulfides. Also, most of the compounds studied in this thesis are transition metal sulfides. It reminds us of a significant family of materials in modern condensed matter physics, the transition metal oxides. In this thesis, we will have a brief introduction to the physical phenomena and properties of transition metal oxides. The physics of transition metal oxides will help us understand the magnetic transitions in our transition metal sulfides better. Besides sulfides, there is also some other type of natural superconductors.

In 2013, researchers discovered a superconducting transition in natural mineral calaverite ($AuTe_2$) by applying pressure up to 2.34 GPa [12]. The transition temperature is 2.3 K with a pressured induced structural transition. The transition temperature was increased to 4.0 K by doping Pt atoms into lab made $AuTe_2$. Calaverite has monoclinic lattice structure with Au layers and Te layers at ambient pressure, and below 5 K. With applied pressure increasing, the material has a low-temperature trigonal structure, and the charged ordered state disappeared and ended in a bulk superconducting state.

The discovery of several natural mineral superconductors gives us an inspiration of searching new superconductors in the natural mineral samples. With a collaboration with the Smithsonian National Museum of Natural History, Department of Mineral Science, I had the opportunity to get access to their collection of mineral specimens. There are several advantages of finding natural superconductors. First of all, a discovery of a new superconductor will be great news to the condensed matter physics research area. Also for a natural superconductor, we

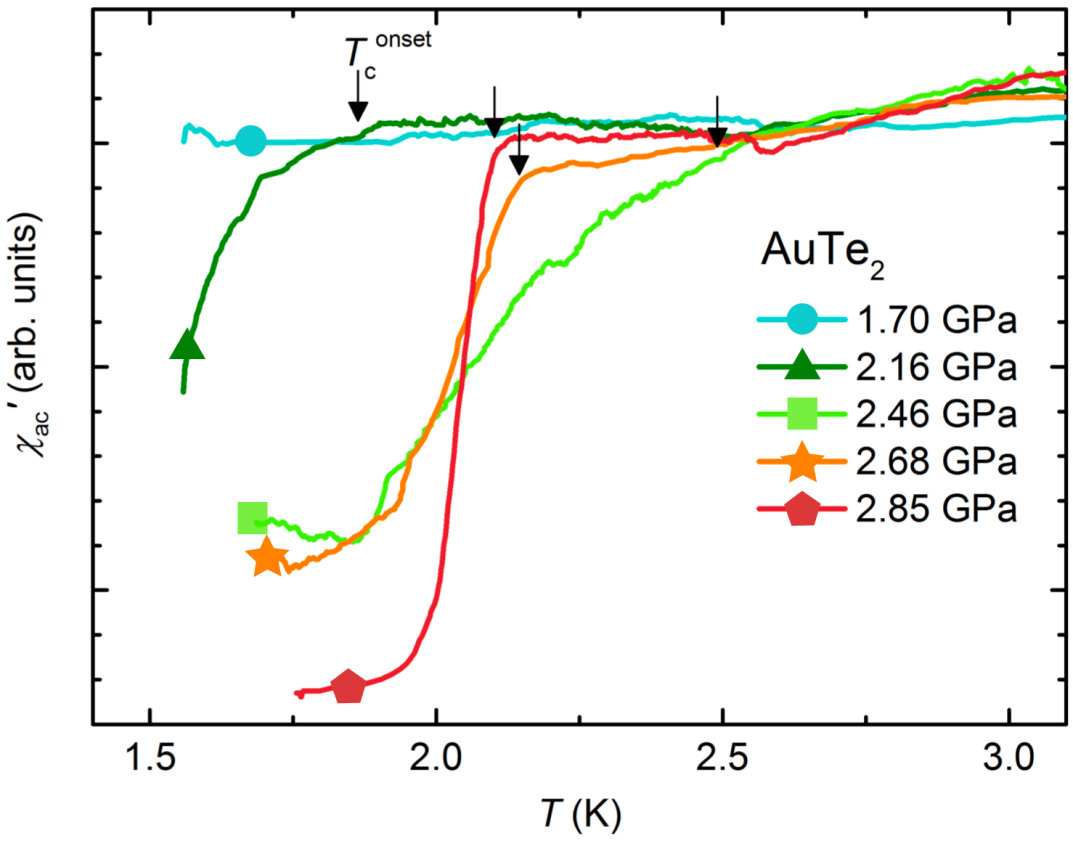

Figure 1.6: The diamagnetic signal of superconductivity in calaverite ($AuTe_2$) with applying pressure (Reference 9).

dont have to make it in the lab, it is possible to have wide applications with stable physical properties.

As I mentioned above, the magnetic ground state is a significant property for the unconventional superconductivity; also, the diamagnetic effect is a signal of conventional superconductivity. So to have a quick understanding of the mineral samples we have, I first do a quick magnetic scan for most of the mineral samples in Quantum Design MPMS system to measure the temperature dependence of the susceptibility. If there is a conventional superconducting state, we will observe a robust diamagnetic signal. On the other hand, considering the phase diagram of the cuprate, most of the unconventional superconducting states come along with a magnetic transition or magnetic ground state. So if we observe a magnetic transition in a particular sample, we will do more research on it including resistivity, heat capacity, and other physical properties. For some of the interesting mineral samples, I also attempt to grow them in the lab to get better crystals.

I have measured more than 40 samples from Smithsonian and discovered 17 unreported magnetic transitions, which will be introduced in details in the following section. Most of the samples were in good condition and were characterized with X-ray diffraction experiment and EDS experiment. In this thesis, I will introduce four different natural minerals I studied in detail. Before I introduce the interesting mineral samples, I will first give a brief introduction about transition metal compounds from the transition metal oxides and what we are expected from the mineral samples.

1.2 Physical Properties of Transition Metal Oxides

Even though I did not find any new superconductor from the mineral samples, I discovered several unreported magnetic transitions and also did further research about several reported magnetic transitions. Most of the minerals I measured are transition metal sulfides, and the magnetic properties of some samples remind me another important family of materials, the transition metal oxides.

Transition metal oxides are significant for many reasons. In last several decades, there were several notable discoveries in both theoretical and experimental condensed matter physics about transition metal oxides. The new physics phenomena, especially about the strongly correlated materials, are related to the complex properties of transition metal oxides. For instance, the Mott insulator, high-temperature superconductor cooperate, crystal field effect, colossal magnetoresistance, multiferroic materials, etc. Most of the discoveries are very important and even got Nobel Prize and have a lot of applications in engineering and industry areas such as batteries, photovoltaic materials, etc. In this section, I will have a brief review of the physics of transition metal oxides and its relation with the transition metal sulfides.

1.2.1 Interactions in Transition Metal Oxides

The unconventional physical properties of transition metal oxides mostly arise from the complex interactions in the systems. Besides the electron-electron interaction and electron-phonon interaction, the interactions between charges, spins and orbital degrees of freedom also play a significant role in the physical properties of

transition metal compounds. The complexity is because that most of the transition metal atoms have partially filled d electrons. In the following part, I will start from the magnetic interactions in transition metal systems and explain the novel theoretical and experimental results of transition metal oxides. Similar physical properties can also be found in transition metal sulfides.

Origin of magnetic moments

The total magnetic moment comes from two parts, the spin momentum S and the orbital momentum L. The overall angular momentum can be determined by Russell-Saunders coupling when the spin-orbital coupling effect is not substantial. In this physics picture, the spin (s) and orbital (l) angular momentum of unpaired elections are summed up to have the total spin momentum (S) and total angular momentum (L). S and L are coupled to give total angular momentum J as shown in Figure 1.7, results in a ground state with degenerate levels from $\mid L - S \mid$ to $\mid L + S \mid$ by Hunds rule.

The magnetic moment of an atom is determined by equation 1.1,

$$\mu_J = g_J \mu_B \sqrt{J(J+1)} \tag{1.1}$$

Where:

$$g_J = \frac{3J(J+1) + S(S+1) - L(L+1)}{2J(J+1)} \tag{1.2}$$

The following table shows the magnetic moments of several transition metal ions. The temperature dependence of magnetic moment can be calculated with mean field approach, as shown in the following equation:

$$u_J = \frac{g_J^2 \mu_B^2 J(J+1)B}{3KT} \tag{1.3}$$

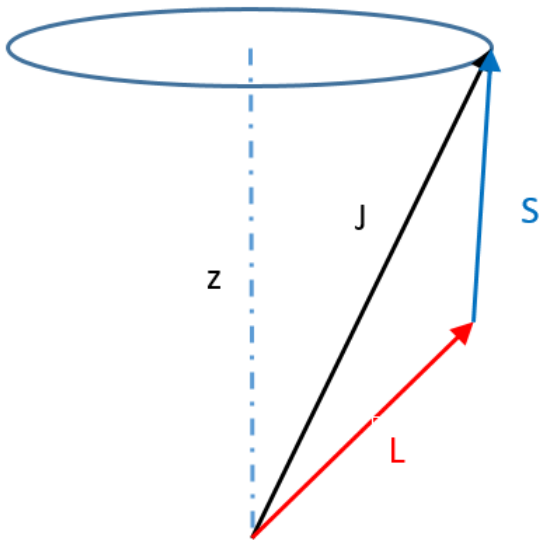

Figure 1.7: The schema of spin orbital coupling and total magnetic momentum.

Metal ion	Theoretical moment	Experimental moment
Fe^{2+}	4	4.1
Mn^{2+}	5	4.6
Co^{2+}	3	3.7
Ni^{2+}	2	2.3
Cu^{2+}	1	1.3

Table 1.1: Magnetic moment of some transition metal ions.

Which is just the famous Curie-Weiss law for paramagnetism: $\chi = C/T$, where the Curie constant C is defined as:

$$C = \frac{\mu_0 \mu_B^2}{3k_B} N g^2 J(J+1) \tag{1.4}$$

Magnetic interaction

The interaction between magnetic moments on each ion site will form a more complex magnetic structure in the materials. The Heisenberg model is often used to describe the interactions between individual moments in the system. As shown in equation 1.5, when the J_{ij} is negative, the spins tend to be anti-parallel alignment, so the material will prefer to have an antiferromagnetic ground state. Otherwise, parallel alignment is favored, and the material will be in a ferromagnetic ground state.

$$H = -J_{ij} S_i S_j \tag{1.5}$$

Heisenberg can be used for most of the direct magnetic interaction. It can also be regarded as a result of Pauli exclusion. Besides the direct interaction, indirect interaction or superexchange is also ubiquitous in transition metal oxides systems.

Superexchange interaction in transition metal oxides is the indirect interaction. The 3d orbitals of transition metal ion overlap with the p-orbitals of oxygen ions. If the transition metal ions and the bridging oxygen ion is around 180 degree, the overall system has antiferromagnetic interaction. If the bond is close to 90 degrees, the system has ferromagnetic coupling. This interaction rule is known as the Goodenough-Kanamori rule.

Paramagnetic	Antiferromagnetic	Ferromagnetic	Diamagnetic
Ti_2O_3	FeO	Mn_3O_4	Yb_2O_3
VO	NiO	γ-Fe_3O_4	TiO_2
VO_2	CoO		Cr_2O_3

Table 1.2: Some room temperature magnetic transition metal oxides.

The couplings and interactions between the spin degree of freedom bring a lot of exotic magnetic transitions in transition metal oxides. Table 1.2 shows several transition metal oxides with the different magnetic order at room temperature. All these materials have a broad application in engineering.

Crystal field Effect (CFE) and the structure of transition metal oxides

Besides the spin-spin interaction, the orbital degree of freedom and crystal structure is another very significant reason for the many exciting phenomena in transition metal oxides. Typically the several oxygen atoms and the transition metal atoms in the systems form TM-O_6 octahedra, TM-O_5 squared pyramid or TM-O_4 planes as shown in Figure 1.8(a). The polarization of the electronic field generated by the oxygen charge density will break the spherical orbital symmetry of the d-electrons of the transition metal atoms.

Because the five d orbitals have different charge density in a different orientation as shown in Figure 1.8(b), the d orbital electrons will lose their degeneracy and split into various energy states. This effect is known as crystal field effect. Figure 1.8(c) shows the electron configuration of a typical crystal field splitting in

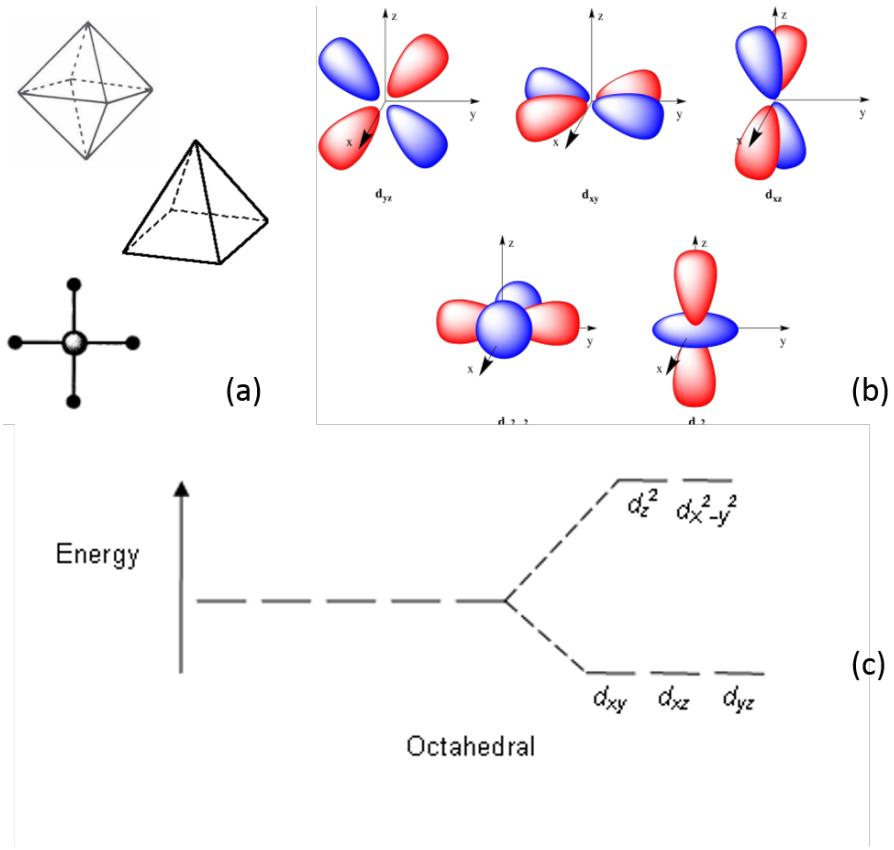

Figure 1.8: (a) The typical structure of TM-O in transition metal oxides. (b) 5 orbitals of d electrons. (c) Energy splitting of d electrons in octahedral crystal field.

an octahedral cell. The crystal field effect will affect the physical properties of the material.

1.2.2 Mott Insulator

One of the most significant concepts related to transition metal oxides is the Mott Insulator. In last century, several theoretical pictures were proposed to explain the electronic properties of metal and insulator. One of the most successful models is the Sommerfeld energy band theory. Consider a free Fermi gas without electron-electron interactions is placed into a periodic lattice potential, if the electrons obey the Fermi-Dirac distribution in momentum space, the available energy states form bands. We call them the energy bands in moment space. For insulators, the electrons in the valence band are separated by a large energy gap from the conduction band. While in conductors like metals, the valence band overlaps the conduction band. And in semiconductors, there is a small enough gap between the valence and conduction bands. Despite its great success in explanation of metal, insulator, and semiconductor, the ignorance of electron-electron interaction eventually brought some troubles. NiO was predicted to be metallic according to the band theory. Nevertheless, NiO had insulating behavior and was not metallic as predicted in later experiments. By introducing the effect of electron-electron interactions, we can explain the effect quantitatively and fix the defect of band theory with Hubbard model. Equation 1.6 shows the Hamiltonian of Hubbard model where t_{ij} represents the electron hopping between site i and site j, U is the Coulomb repulsion between

electrons.

$$H = -t_{ij} \sum (c^{\dagger}_{i,\sigma} c_{j,\sigma} + c^{\dagger}_{j,\sigma} c_{i,\sigma}) + U \sum n_{\uparrow,i} n_{\downarrow,j} \tag{1.6}$$

In a schematic physics picture language, when the t_{ij} is much larger than U, the Coulomb interaction can be neglected, and the system is metallic because the electrons can hop between sites with small repulsion. While if the Coulomb repulsion is much larger than the hopping effect, the electrons will be localized and the system is insulating. Such kind of insulator is called Mott insulator. As shown in Figure 1.9(a), if we consider the Coulomb interaction, the system will also have an energy gap. If the band gap in exists between anion and cation states, it is called charge transfer insulator. As we can conclude, Oxygen atoms play a significant role in strongly correlated transition metal oxides. Based on the localization of electrons, some mechanisms such as Mott-Hubbard model were formulated to understand the antiferromagnetic states in many of these correlated systems. We are expecting to have similar phenomena in some of the transition metal sulfide minerals.

The high-temperature superconductor cuprate is also regarded as doped Mott insulator in theory. In next section, we will discuss the physics of high-temperature superconductor.

1.2.3 High-Temperature Superconductors

Cuprate The first superconductor found with T_c ¿ 77 K (liquid nitrogen boiling point) is yttrium barium copper oxide. It started a new page of supercon-

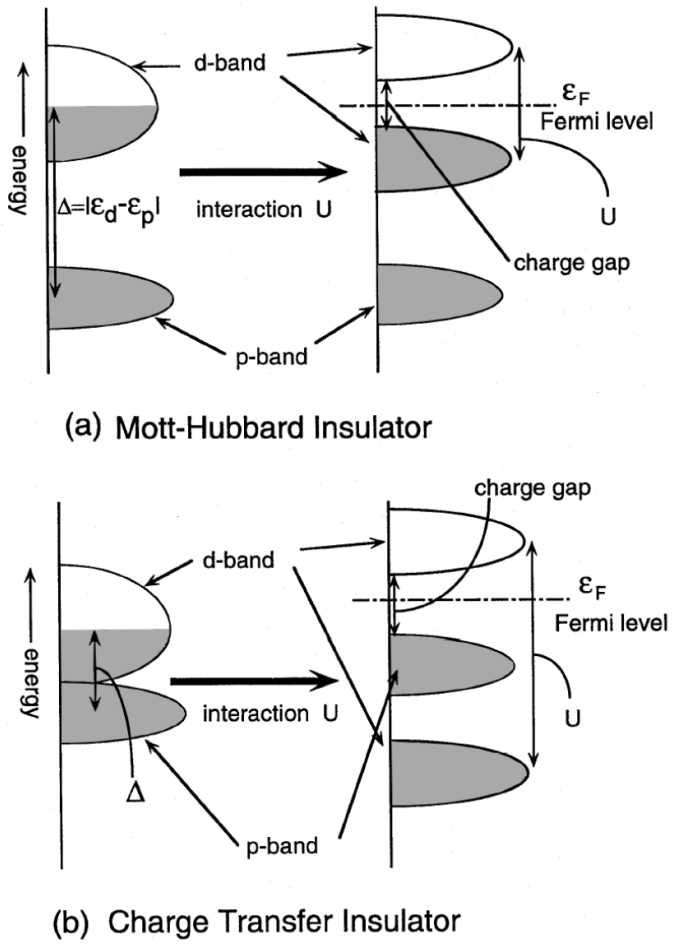

Figure 1.9: The schematic illustration of (a) Mott insulator and (b) charge transfer insulator.

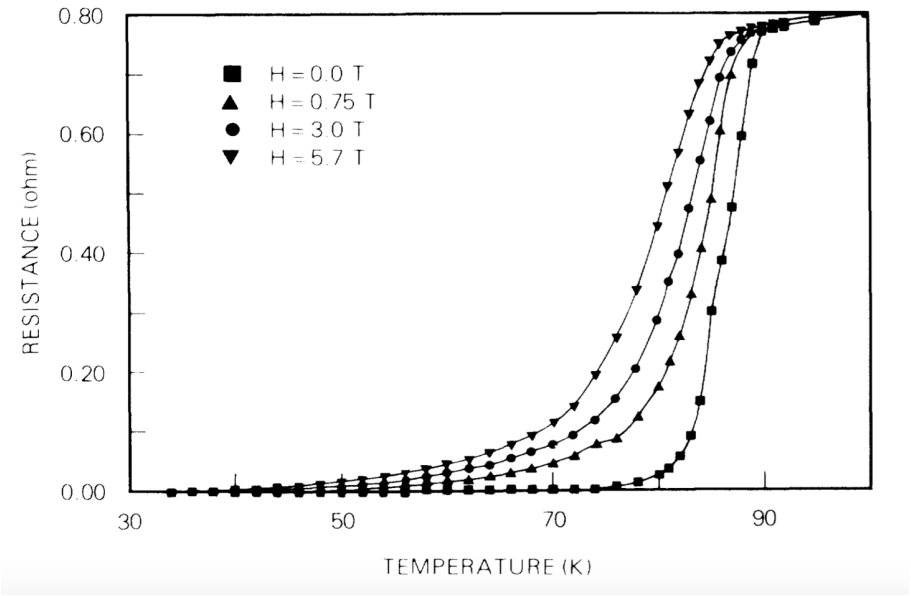

Figure 1.10: Superconductivity in YBCO compound.

ductivity research. This family of unconventional superconductors is called cuprate. All the cuprate superconductors share a similar structure with two common elements: the CuO_2 planes which form single-layer or multilayer conducting blocks per unit cell, and the charge reservoirs that are responsible for contributing either electrons or holes to the CuO_2 planes. It has been well studied how the CuO_2 plane contributes to the high-temperature superconductivity. We can control the carrier density in CuO_2 planes with electron or hole doping [13].

Election configuration

Cuprates are regarded as doped Mott Insulator. In the undoped compounds, the electronic states of the Cu ions on the CuO_2 plane are in the d configuration. The crystal field effect splits degenerate electrons into e_g and t_{2g} orbitals. The degenerate e_g orbitals split again due to the Jahn-Teller effect of the surrounding oxygen octahedron, leading to a partially filled $d_{x^2-y^2}$ orbital with the highest energy.

The Cu $d_{x^2-y^2}$ orbital forms a strong covalent bonding with the O atoms' p_x, p_y orbitals. The hybridization of the three orbitals results in the bonding, non-bonding and half-filled anti-bonding bands that predict a good metal considering the band theory, while the undoped samples turn out to be an insulator instead of a conductor.

Hubbard model picture As I mentioned in the previous section, cuprate is considered to be similar to doped Mott insulator. The contrast between the empirical prediction and the experiment results has been well investigated by theorists using Hubbard model and taking Coulomb repulsion into consideration. In a cuprate systems, the energy cost of having a second hole in the Cu d-orbital is much larger than the energy difference between the Cu $d_{x^2-y^2}$ and O p-orbitals. So the extra hole goes to the O atoms' p_x, p_y-orbitals more easily than to Cu orbitals. Thus the hoping energy is much smaller than the energy barrier, so the electrons form localized moments on the Cu sites, the spins interact via the superexchange interaction and results in an antiferromagnetic state. So the undoped parent compounds are also referred as antiferromagnetic Mott insulator. By electron or hole doping, we can break the Mott insulator state and have a superconducting state at a lower temperature.

Phase diagram

Compared with the undoped parent compounds, if we introduce carriers (electron or hole) into the systems, as shown in a simplified phase diagram (Figure 1.11), several novel phase transitions show up in both electron and hole doping. The phase diagram was made from many experiments including transport measurements, ARPES, STM, neutron scattering with different cuprate compounds. We

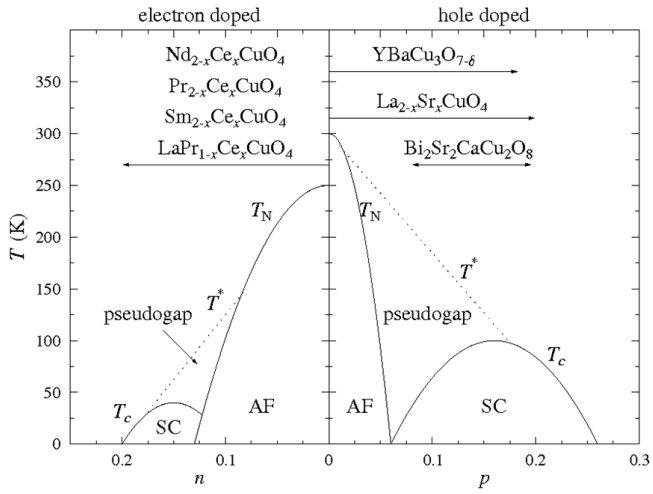

Figure 1.11: Phase diagram of cuprates. The AFM insulating state can be tuned by electron or hole doping and ends in a SC state (from Wikipedia).

will not go through the experiments in details. Instead, I will have a brief discussion about the transitions along the x-axis of the phase diagram phenomenally.

As we already know, the system stays in an antiferromagnetic Mott insulator state at zero doping. When holes are introduced to the system, the Neel temperature (T_N) decreases rapidly, and the antiferromagnetic ground state is killed at a critical doping level. If we continue introducing holes, various types of spin fluctuation states replace the antiferromagnetic ground state, and a new superconducting phase reveals with a particular optimal doping concentration and disappears if the system is over doped. Between the antiferromagnetic region and superconducting region, an opening spectral gap in spin and charge fluctuation with a suppress in the density of states around the Fermi energy has been observed in experiments. This region is referred as pseudogap. Beyond these states, the system stays in Fermi liquid state. On the electron doping side, the behavior is very similar to hole doping side

except that the antiferromagnetic region is broader and the superconducting region is narrower.

1.2.4 Colossal Magnetoresistance Effect

The Colossal Magnetoresistance Effect (CME) will help understand the relation between transport properties and magnetic properties better. Magnetoresistance is the property of the field dependent resistivity of materials. Most of the metals have magnetoresistance. The colossal magnetoresistance effect is a property of some transition metal perovskites. In early 1950s, a ferromagnetic transition accompanied by a metal-insulator transition was discovered and extensively studied after that. The magnetic transition is associated with large negative magnetoresistance in doped lanthanum manganite as shown in Figure 1.12. The large magnetoresistance and the metal-insulator transition is attributed to double exchange mechanism. As shown in Figure 1.12, in these systems, the hopping effect between site i and site j is proportional to $\cos(\theta_{ij})$, where θ_{ij} is the angle between the magnetic moments on site i and its nearest neighbor site j. When the temperature is above the transition temperature, the system is in paramagnetic state, the angle between magnetic moments is large, and the hopping effect is small. While when the system becomes ferromagnetic order with a temperature below the transition temperature, the spins tend to be aligned to the same direction and the hopping effect becomes large. In this case, the system will show insulating behavior above the transition temperature, while will have metallic property below the transition temperature. For the

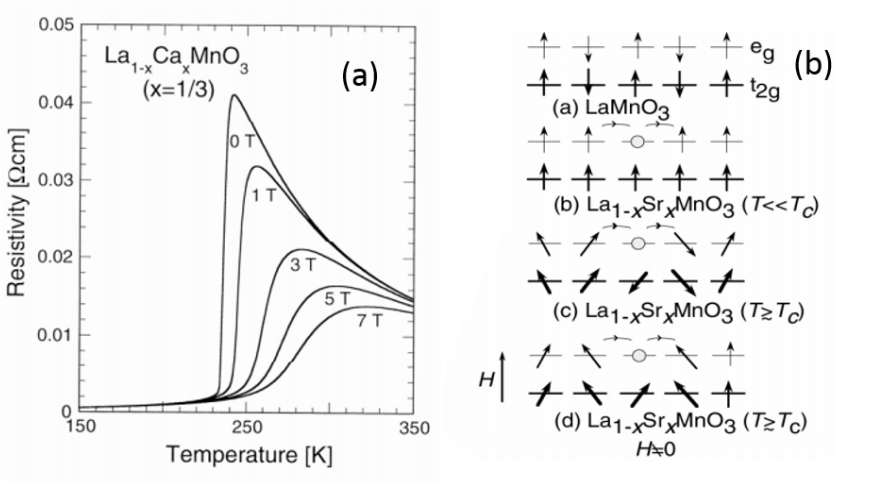

Figure 1.12: (a) The Colossal magnetoresisitance effect in $La_{1-x}Ca_xMnO_3$. (b) A schematic digraph of the theory of CME.

same reason, the spins tend to be polarized with field increasing, and the hopping effect becomes large which leads to a large negative magnetoresistance. Even though most of the materials with CME effect are oxides, some sulfides with charge ordering state also have the colossal magnetoresistance. For example, Mn^{2+} doped FeS and chromium sulfide Cr_2S_{3-x} all show some colossal magnetoresistance effect and both of the materials have some mineral form analogs with similar structure and chemical formula.

1.2.5 Anisotropic Properties

Anisotropic physical properties is another essential characteristic of many transition metal compounds. I also found some anisotropic structures in the minerals. Some of the transition metal oxides have an anisotropic unit cell structure, and the anisotropy in structure leads to anisotropic electronic and magnetic properties. An

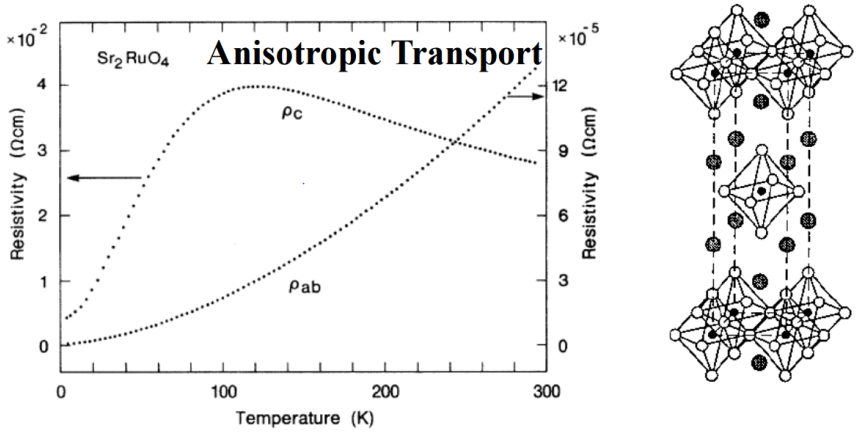

F. Lichtenberg / Progress in Solid State Chemistry 30 (2002) 103–131

Figure 1.13: The anisotropic transport property of Sr_2VO_4.

example is the Sr_2RuO_4, as shown in Figure 1.13, resistivity along c axis and perpendicular to the c axis are different. Some of systems are perfect low dimensional materials. For example quasi-1D transition metal oxide Sr_2VO_4.

In this part, I summarized the many interesting magnetic characteristics of transition metal oxides which are related to our research about the mineral samples. With these magnetic properties, transition metal oxides have a comprehensive application in industry. Similarly, the transition metal sulfide minerals may also have similar applications if we understand them better. Some transition metal oxide nanolayers are used as photovoltaic devices or solar cells. Even with a layered structure, some transition metal oxides are used as battery materials.

1.3 Comparison of Transition Metal Sulfides and Transition Metal Oxides

Transition metal sulfides can be regarded as a family of general transition metal oxide since the S atoms also from VIA group like the O atoms in oxides. For transition metal sulfides, they also have the same physical properties of transition metal ions in transition metal oxides. Even some of them have the similar TM-Sn structure like the transition metal oxides. With similar structure and physical characteristics, transition metal sulfides are also expected to have a lot of magnetic transitions and applications like transition metal oxides; however, most of the transition metal sulfides have not been well investigated. In the project of searching natural superconductor, I had an opportunity to get access to the large storage of minerals in Smithsonian Museum. I found most of the minerals are transition metal sulfides and had a chance not only to search natural superconductors but also to study the transition metal sulfides and other transition metal compounds.

In this thesis, I will show some similarities between the transition metal oxides and the natural transition metal sulfides based on my work. I will show an anisotropic low dimensional natural sulfide, berthierite ($FeSb_2S_4$). Also, I will show a natural transition metal sulfide bornite (Cu_5FeS_4) with a magnetic insulating state. Perhaps it will be a good starting point for natural superconductors. In the end, I will go through the interesting results from the many measurements during this project. A lot the sulfides have some transitions in transport associated with some

magnetic transition. Just like the picture of colossal magnetoresistance effect, the interactions between electrons and spin degree of freedom is not that simple.

Also, I will present some other interesting results of other transition metal minerals. A Ferromagnetic order was found in natural nagyagite ($Pb_5Au(Te,Sb)_4S_{5-8}$) samples. The magnetic order, the weak anti-localization property with strong spin-orbital coupling and the 2-dimensional structure of this compound make it a very interesting system for realizing topological properties in a natural compound. The magnetic order and transitions in both natural and synthetic maucherite ($Ni_{11}As_8$) samples show interesting finite-size scale effects. It gives us a different approach to understand the differences in some physical properties of natural and synthetic compounds.

Chapter 2: Experimental Methods

2.1 Chemical and Structural Characterization

The curators Cara Santelli, Jeff Post, and the collection manager Paul Powhat at Smithsonian helped us select the mineral specimens from the museum collections. Even though most of the natural mineral samples seem to have excellent quality, we still must determine their chemical compositions and structural properties. The chemical characterization is not only for investigating the structure of the materials but also for confirming the composition of the materials and proving that the physical properties we got from the measurements are intrinsic instead of induced by some impurities. Energy-dispersive (EDS) spectroscopy techniques give us the elements ratio in a given sample with very high accuracy. X-ray crystallography allows us to calculate the structure of a given material and the unit cell lattice constants. These techniques provide us an exact chemical composition analysis of the mineral materials.

2.1.1 Energy-dispersive Spectroscopy

Energy-dispersive Spectroscopy (EDS) obtains a local chemical composition analysis by using the X-ray spectrum emitted by a solid sample with a focused beam of electrons. The electron beam excites the electrons from the atoms in the sample, which release X-rays of different energy as they leave the atom. The full range of X-ray energy values is measured at one time. We can determine the elements in the material with the energy of the peaks and calculate a number of the elements from the density of the peaks.

The accuracy of EDS is affected by various of factors. Sometimes we are not able to figure out the elements correctly because of the overlap of peaks of some elements. Also, the surface of the sample will affect the penetration depth of the elections beam, so the samples should be well polished before experiments.

The EDS measurement was taken with the scanning electron microscopy (SEM) made by Bruker at Micro and Nano Fabrication Laboratory at University of Maryland. The device has a field emission SEM with EDS capability. The result was analyzed with AMICS software.

2.1.2 X-ray Crystallography

Powder X-ray diffraction (XRD) is a very versatile technique to characterize the structure and composition of samples. In our experiments, most of the mineral samples are polycrystalline compounds. Powder X-ray diffraction is used to study the materials. X-rays are partially scattered by atoms when they strike a crystal.

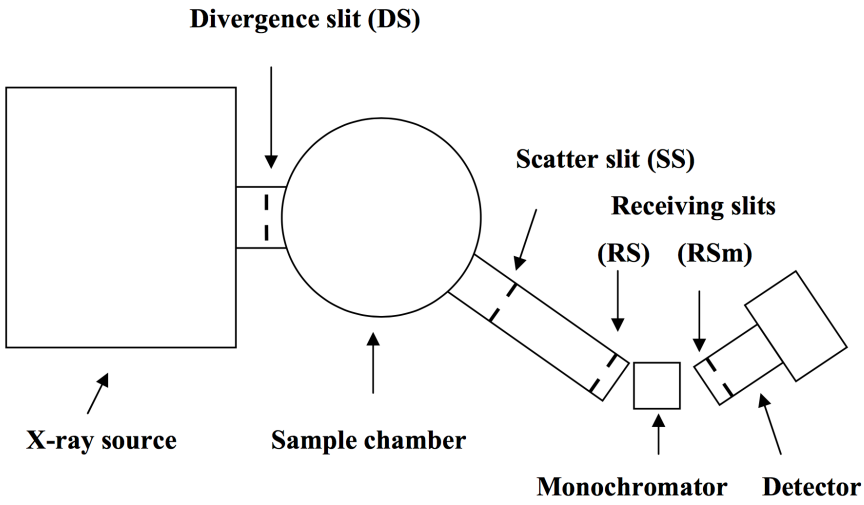

Figure 2.1: A schematic digraph of X-ray diffraction experiment setup.

The part of the X-ray that is not scattered passes through to the next layer of atoms, where again part of the X-ray is scattered, and part passes through to the next layer. The scattering on different planes formed by the atoms causes an overall diffraction pattern. The angle θ and the distance between layers d follow the Bragg's law,

$$n\lambda = 2d\sin\theta \tag{2.1}$$

A diffraction pattern can also be used to determine and refine the lattice parameters of a crystal structure. A theoretical structure can also be refined using a method known as Rietveld refinement. We can determine the value of lattice parameters of the materials as well as the composition of our target sample.

As shown in Figure 2.1, a powder X-ray diffractometer consists of an X-ray source, a detector, and a sample stage. The X-ray is focused on the sample at some angle θ, while reads the intensity of the X-ray it receives at 2θ.

Most of the powder XRD diffraction data were collected on Rigaku Miniflex X-ray diffractometer. It is a multipurpose analytical instrument that can determine: phase identification and quantification, percent crystallinity, crystallite size and strain, lattice parameter refinement, Rietveld refinement, and molecular structure. The X-ray source is from Cu $K\alpha$ radiation, $\lambda = 1.5418$ $\mathring{A}$

2.1.3 Neutron scattering

Neutron diffraction technique is a versatile technique to determine the magnetic structure. The mechanism of X-ray and neutron diffraction are very similar, but with some differences because of the nature of neutron, they are used as complementary techniques due to their different atomic scattering mechanisms. Neutron has spin-1/2 and will interact with the magnetic moments in the compound, which will lead to magnetic peaks in the diffraction pattern. So neutron diffraction can be used to study both magnetic and non-magnetic excitations in materials, as the energy of thermal neutrons is comparable to the energy of lattice vibrations and the neutron wavelength is comparable with typical interatomic distances in solids.

The BT-1 high-resolution neutron powder diffractometer at NIST Center for Neutron Research is used to obtain neutron powder diffraction data for crystallographic analysis by the Rietveld method or other characterization purposes in our experiments. It is a 32 detector instrument that can be used with three different monochromators and two separate incident Soller collimators, allowing the instrument response to be tailored to the needs of the experiment. The instrument can

be used with furnaces, refrigerators, and cryostats so that data may be collected at temperatures from 0.3 to 2000 K, and with magnet fields. For room-temperature data collection, a six-position sample changer is available.

2.2 Physical Properties Characterization

2.2.1 Magnetic Susceptibility

Magnetic susceptibility is the most important physical property we collected with the mineral sample. Because of the large amount of mineral samples from the Smithsonian Museum, we have to decide which mineral samples worth further investigation and so that we can focus on them. We measure the magnetic susceptibility temperature relation, and if there is a magnetic transition, we will collect more data from other experiments and even grow the material in our lab. Magnetic susceptibility is taken from Quantum Design Magnetic Property Measurement System (MPMS). The sample is loaded into a dewar with two magnetic coils. Measurement field up to 7 T is generated by one coil with a voltage corresponding to given magnetic field applied to the coil. The other coil takes the total magnetic response from the system and sample in terms of *emu*. The system temperature can be cooled down to 2 K with helium and well controlled. In some of the materials, the data show some difference between field-cooled (FC) and zero-field-cooled (ZFC) measured due to the spin interactions such as spin glass phase or superparamagnetism. So we need both measurements. To this end, we put the sample in straw and insert it into the MPMS system, first cooled down to the base temperature of 2 K then

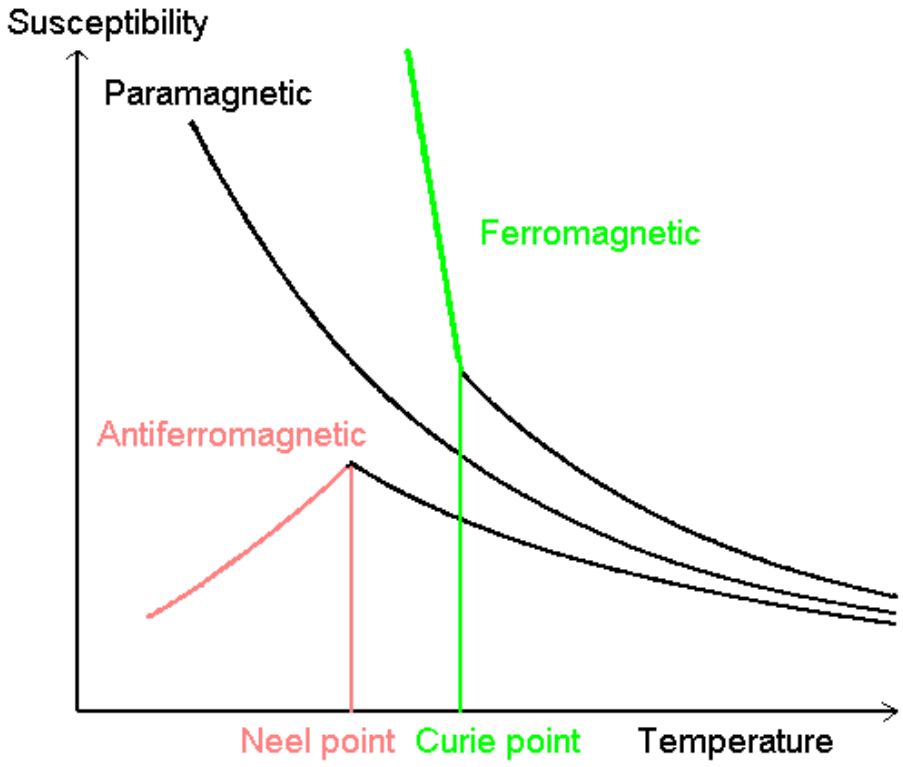

Figure 2.2: The susceptibility temperature relation of AFM, FM, and PM materials..

a field is applied. After centering the sample in the middle of the field, the sample is slowly warmed up while taking measurements. Once the temperature is back to room temperature, it is cooled down back to the base temperature with the same field applied. The susceptibility temperature tells us a lot of information; we can quickly figure out the type of magnetic transitions from the shape of susceptibility temperature relation. The typical characteristics of susceptibility and spins of several magnetic phase transitions are shown in Figure 2.2.

2.2.2 Electronic Transport Measurements

For the mineral samples, once we found there are some magnetic transitions in the magnetization temperature relation, more physical properties characterization will be prepared. Transitions in resistivity accompanied with the magnetic transitions are always worth more attention. Due to the magnetic order and exchange interactions between electron spins, some transition metal sulfides also have a similar transition like a metal-insulator transition in transition metal oxides. These transitions are the footprint of superconducting in strongly correlated systems. We typically use two different measurement configurations to measure the resistivity of samples base on the sample size. As shown in Figure 2.3 (a), when the samples are too small for attaching four wires, we use 2-wire probe method. This method is considered inferior because the measured resistance includes not only the sample resistance but also the contact resistance of the wires. The technique only works only when the contact resistance is much larger than the sample resistance. As shown in Figure 2.3 (b), four wires probe method are more common and precise. A current will be applied through the two current wires, and the voltage value between the two voltage wires will be collected. The contact resistance can be neglected with the four wires probe method. Also before the measurement, we also have to do several tests to determine the proper current with good enough signal and small enough thermal effect.

The resistivity can be obtained via the resistivity formula and Ohm's law in equation 2.2, V is the voltage, I is the applied current, s is the sample cross-sector

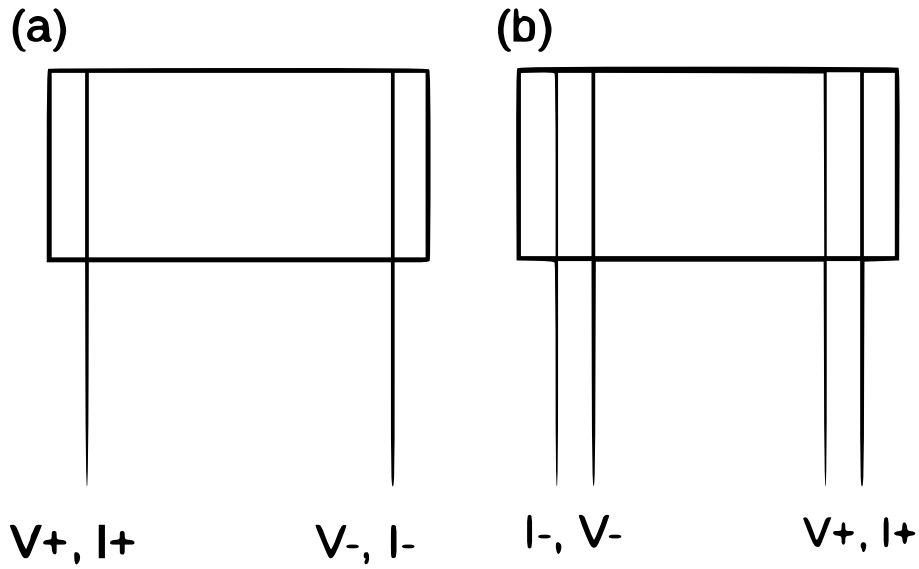

Figure 2.3: (a) Two wires probe method setup. (b) Four wires probe method setup.

area, and l is the distance between two voltage wires. We will cut and polish the samples with razer and sandpaper into good shape and smooth surface.

$$\rho = \frac{Vs}{Rl} \tag{2.2}$$

There various technique for making a good contact for transport measurement. Good contact has minimal contact resistance and also do not leave stray capacitances that may change the characteristics of the contact. In the mineral measurements, we mostly like to use silver paste, silver epoxy, solder or spot welding according to the sample condition.

Silver paste and silver epoxy method are very similar. For the silver paste method, we dissolve Dupont 4929 paint together with its solvent to make a liquid paste. For the silver epoxy method, we mix two different chemical reagents to get the silver epoxy paste. Wires will be covered by the paste and put onto the sample

with tweezers under a microscope. Silver paste dries at room temperate, while for the silver epoxy, we have to bake it at around 500 K for 10 minutes. Silver paint method is more straightforward and typically has smaller contact resistance, but the contact is not as high as epoxy which may fall off under some extreme conditions or with vibrations. The silver epoxy method has a firm connection while sometimes its contact resistance is large and the baking time is not suitable for some air-sensitive materials. The soldering method needs excellent craftsmanship, it gives firm enough contact and small contact resistance, but it is challenging and sophisticated. A small amount of PbSn solder is melted on the tip of a soldering iron, and a small amount of soldering flux is put on the end of the gold wire and the contact point on the sample. The operation is just the same as regular soldering work except for the samples are always extremely small. The spot welding method also gives firm contact and small contact resistance, even it is more comfortable for operation compared with solder method. The gold wire is loaded between a tip connected to a current source and the sample, and we will measure the resistance between the tip and the wire. Once they are attached to the sample, we will apply a pulse current to the tip. The heat generated from the current will melt the gold wire and connect it to the sample with a minimal contact resistance. The flaw is sometimes the current may break the samples into pieces.

There is no perfect method for all the samples. We sometimes have to play some trick with the measurements. For instance, for some of the transition metal sulfide mineral samples, the S atoms in the sample may react with the Ag atoms in the minerals forming some insulating AgS, ends in fragile and bad contacts. Solder

and spot welding also doesn't fit because of the sample size. In this case, we will use the physical vapor deposition(PVD) technique. We attach three strips of thin lithographer's tapes on the sample. The sample is loaded at the top of the vaporing chamber with the surface with tapes facing down. Some gold is put at the bottom of the chamber to generate gold vapor. A gold thin film will form on the surface of the sample, and the thickness can be easily controlled. After the fabrication, we remove the tape to get four independent contact points covered by the gold film so that we can avoid the reaction between contract paste and the samples.

2.2.3 Heat Capacity

Heat capacity temperature dependence is a prevalent method to identify the transition temperature and to study the quantum phase transition in a given material. Heat capacity is the amount of heat required to change the temperature of the material. The magnetic transitions in transition metal oxides are forming magnetic order, which is always accompanied by a structural transition or other phase change in electronic structure. So a noticeable change in the heat capacity data can always be found at the transition temperature.

We use the heat capacity setups and option on the 14 T PPMS. The sample is mounted on a heat capacity puck with Apiezon N grease, the heat capacity puck with the addenda has to be measured before putting the sample onto it. As shown in Figure 2.4, the puck has several thermometers to measure the temperature of different parts. Heat is applied to the sample, and the decay constant is recorded

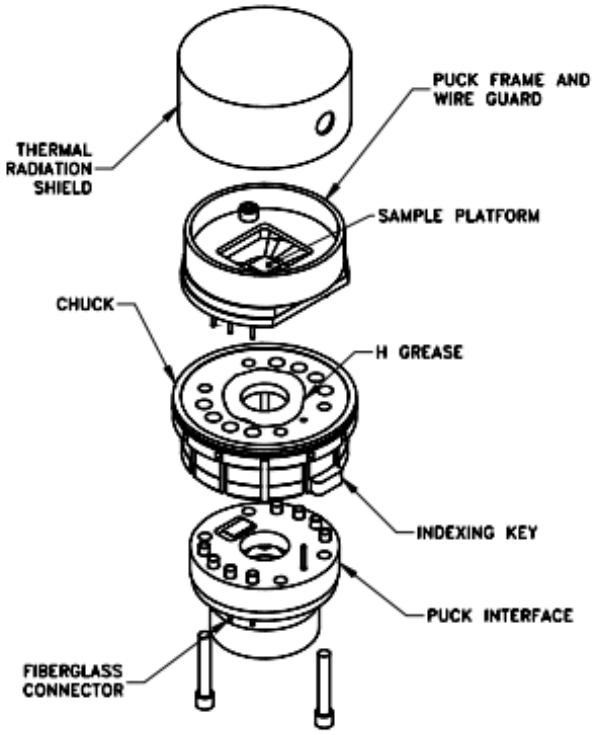

Figure 2.4: Exploded view of Quantum Design PPMS heat capacity puck, the picture is from the manual of Quantum Design PPMS.

during the measurement. By subtracting the addenda heat capacity from the total heat capacity, we can get the sample heat capacity with very high accuracy.

Besides the magnetic properties, heat capacity temperature dependence also gives us information about the electronic and structural properties of materials. The phonon contribution to the total heat capacity can be described with Debye model,

T_D is the Debye temperature. When the temperature is much smaller than T_D, the Debye model can be regarded as a T^3 model approximately. For metal or insulator, the electron contribution to the heat capacity is also added to the model with a linear T term.

2.2.4 Pressure experiments

As mentioned in chapter one, in some transition metal oxide systems, applying pressure will induce further transition like metal-insulator transition, superconducting transition. With very similar physical properties of transition metal oxides, we also measured some of the mineral samples under pressure. The measurement of pressure below 3.0 GPa is taken with the EasyLab piston cylinder high-pressure cell. The structure of pressure cell is shown in Figure 2.5. The photo of pressure setup is shown in Figure 2.6.

The contact is made with the 4-wire method with silver epoxy to avoid the contact detaching under pressure. We put the sample into the Teflon cap filled with pressure medium. By compressing the piston, we can apply pressure to the pressure medium so that the pressure will be applied to the sample evenly. The value of used pressure is confirmed with the superconducting transition temperature, which is very sensitive to the pressure. We can get to 3.0 GPa with the piston cylinder pressure cell in our lab. Diamond anvil cell (DAC) is used for higher pressure measurement. Figure 2.7 shows the principle of DAC. Pressure will be applied to the sample space if we press the top to DAC.

2.3 Crystal growth

For some of the mineral samples, the natural crystals sometimes have different physical properties from the lab made crystals due to some defects in structure or composition. Also, some experiments like neutron scattering require crystals with

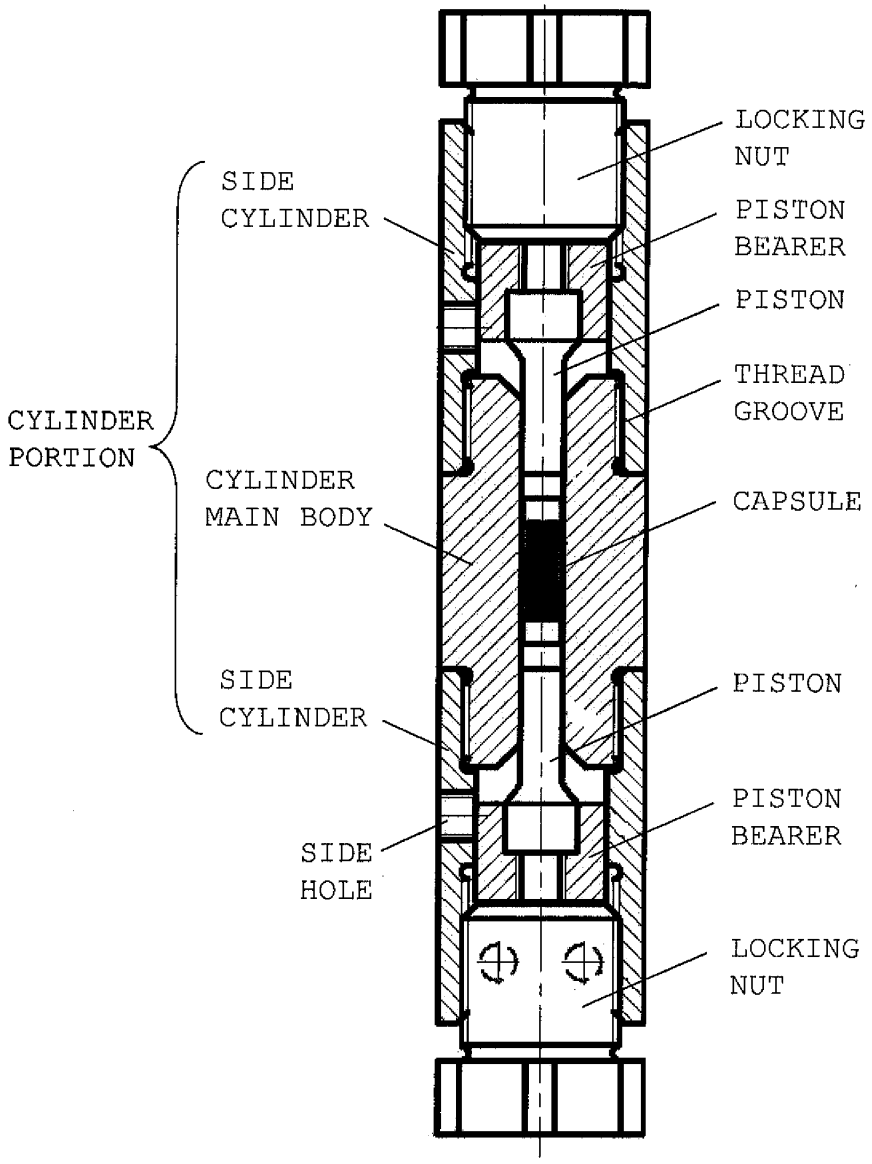

Figure 2.5: The setup of a typical piston cylinder pressure cell (from US Patent 20110094376 A1).

Figure 2.6: Photo of our pressure cell setup. The sample holder was made by me.

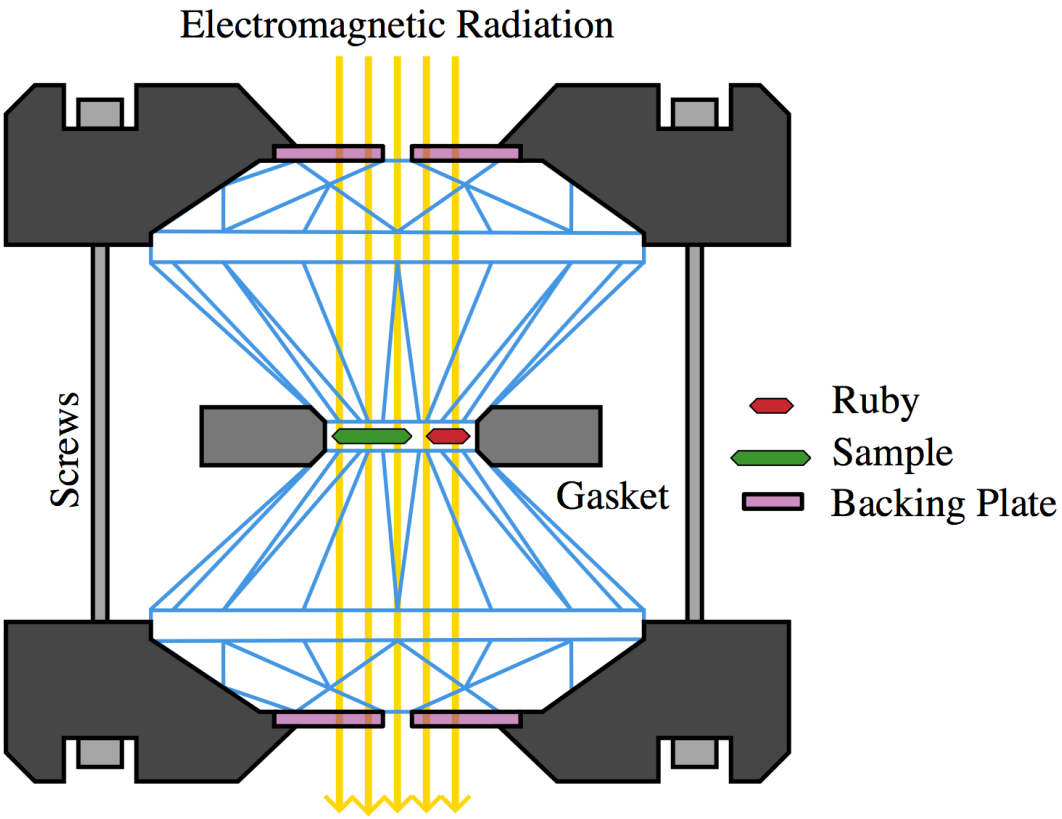

Figure 2.7: A typical setup of diamond-anvil cell (from Wikipedia).

larger size and higher quality. In these situations, it is necessary to grow larger polycrystals or single crystals. The most common method we use for transition metal sulfides growth is flux method. Similar to making sugar crystals from water, crystals also form in flux while cooling down. A flux growth starts from finding a good flux. A good flux typically has a low melting temperate and a good solubility for the elements. Also, it doesn't enter crystal as inclusions and doesn't create competing phase. The Antimony(Sb) flux is a good choice with a melting temperature of 630 °C and high stability. We used it for almost all growths. The crystal growth is accomplished by mixing a large molar amount of flux crystals and a smaller amount of required elements. The mixture is put in a crucible and sealed into a quartz ampoule under vacuum. We place the ampoule in a furnace and heat it to a high temperature to make the materials dissolve into the flux. The system is then cooled down slowly according to the phase diagram, the flux solubility decreases, and crystal forms.

I tried growing several compounds during this project. I made synthetic $Ni_{11}As_8$ polycrystals (will be mentioned in Chapter 6), Cu_3BiS_3 polycrystals, Fe_7S_8 polycrystals successfully. Also, I made some Cu_5FeS_4 polycrystals with $CuFeS_2$ impurities. I attempted to grow nagyagite, $FeSb_2S_4$ but didn't succeed.

2.4 Density functional calculation

Another powerful technique we used in this project is the density functional (DFT) calculation. DFT is a quantum computational modeling method to inves-

tigate many body systems. We can get the density of states and band structures from the DFT result. The main idea of DFT is to calculate a many-body interaction via the particle density instead of using the wavefunction. There are several commercial software with graphical user interface allow us to set up the atoms in materials with space group and certain unit cell structure, and to call the atom density functions directly. In this project, Mr. Xiuquan Zhou helped me do most of the DFT calculation using software VASP.

In this chapter, we introduced the experimental method we used for this project. In the next several sections, we will present the preliminary results of several absorbing natural materials.

Chapter 3: Berthierite ($FeSb_2S_4$): An natural quasi-one-dimension antiferromagnet with anisotropic magnetization.

In this section, we will discuss the unusual structural properties of transition metal sulfide compound with a natural transition metal sulfides berthierite ($FeSb_2S_4$). Berthierite ($FeSb_2S_4$) is a kind of iron and antimony sulfide mineral with gray metallic luster. Berthierite consists of one-dimensional chains of FeS_6 octahedra separated Sb atoms. Below 50 K, magnetic moments of Fe in each chain can align collinearly to form a long-range antiferromagnetic ordering via interactions with neighboring chains. The relationship between its low-dimensionality and magnetic order remains a puzzle. All the experiments were done by myself. Mr. Xiuquan Zhou helped me do the DFT calculation, and we analyzed the result together.

3.1 Introduction

Many materials with chemical formula AB_2C_4 have been investigated in recent years, where A is a transition metal element, B is a group V element and C is group VI chalcogenides (S, Se, and Te). In AB_2C_4, 3d transition metal A prefers octahedral coordination and forms AC_6 edge-sharing octahedra chains as the backbone of its structure. Several materials in this family show some interesting magnetic tran-

sitions at low temperature accompanying interesting physical properties [14]. For instance, $FeSb_2Se_4$ has been reported as a ferromagnetic material driven by structural distortion with a semiconductor-insulator transition [15]. $MnSb_2Se_4$ has been reported as a semiconductor with an antiferromagnetic transition at 20K [16]. With Cu-doping, $MnSb_2Se_4$ also show an enhancement in thermoelectrical property [17]. Their unique structure-property relationship, electronic and magnetic properties attract a lot of interests and demand through investigations on this family of materials.

Berthierite($FeSb_2S_4$) is a natural mineral of the AB_2C_4 family. An antiferromagnetic transition in natural occurring $FeSb_2S_4$ at 50K was reported by J.D. Donaldson in 1972 from Mössbauer and susceptibility measurement [18]. In 1983, Kerimov *et al.* found an abnormality between 50K and 70K and concluded it as a 2D material with linear M-H curve [19]. However, some of the results are not consistent with following measurements on natural mineral samples. The magnetic structure of this material was confirmed with neutron diffraction on natural samples by Wintenberger and Andr [20]. However, the magnetic interactions in the material are still not clear. In this section, We will discuss the anisotropic and low dimensional properties of berthierite with magnetic susceptibility, electrical resistivity, and heat capacity measurements of natural berthierite single crystals and density functional(DFT) calculations.

3.2 Experiments

Berthierite single crystal samples were provided by Department of Mineral Science, Smithsonian National Museum. Power x-ray diffraction data were collected with Rigaku MiniFlex x-ray diffractometer. Temperature dependence of susceptibility from 300 K to 2 K and the M-H curve up to 7 T were measured with Quantum Design Magnetic Property Measurement System (MPMS), the data were collected with field along a different direction. The temperature dependence of resistivity was measured on large bulk samples with four wires method with putting current along different directions in Quantum Design Physical Property Measurement System (PPMS). The heat capacity was investigated with the PPMS from 150 K to 2 K as well.

3.3 Results and Discusion

3.3.1 Crystals and X-ray diffraction

The natural Berthierite samples have needle like shape and dark grey metallic luster. Powder X-ray diffraction (XRD) data were collected with Cu $K\alpha$ radiation, λ = 1.5418 $\mathring{A}$, with 2θ ranging from 10° to 90°. Rietveld refinement for the XRD data collected from ground single crystals is presented in figure. 3.1, which is consistent with the previous reported structure of $FeSb_2S_4$ single crystals. Berthierite has an orthorhombic unit cell with *Pnam* space group. The lattice constants are a = 11.44 $\mathring{A}$, b = 14.12 $\mathring{A}$, c = 3.76 $\mathring{A}$ [21]. Similar to other compounds in the

AB_2C_4 family, berthierite consists of one-dimensional chains of edge-sharing FeS_6 octahedra separated Sb atoms. 0Each iron atom is surrounded by 6 sulfur atoms and forms a octahedral cell, the chains are connected via Sb-S-pyramids within the *ab* plain (figure. 3.1). The anisotropic interactions between transition metal atoms induced by strong anisotropic structure along and perpendicular to the *c*-axis always contribute to some low dimensional characters in the AB_2C_4 family materials and other compounds with similar structure.

The magnetic structure of $FeSb_2S_4$ has been deduced by M. Wintenburg with neutron diffraction refinement as shown in Figure 3.1 [20]. The magnetic moments at z and z+1 levels in the chain along c-axis make an angle of 142°, The moment at level z on chain 1 makes angles of 71°with its neighbors at z+1/2 on chain 3, of 109°with those at z+1/2 on chain 2, and of 180°with its neighbor at level z on the chain 4.

The distance and angles and lengths of chemical bonds between the Fe, Fe and S atoms are presented in TABLE 3.1. In the chain along *c*-axis, the FeS_6 octahedral are connected via sharing two S atoms. Each chain is connected via S-Sb pyramids. The distance between inter-chain nearest neighbors is about twice of the value of intra-chains. The magnetic interaction intra-chains should be larger than the interchain interaction, which may end in some low dimensional phenomena.

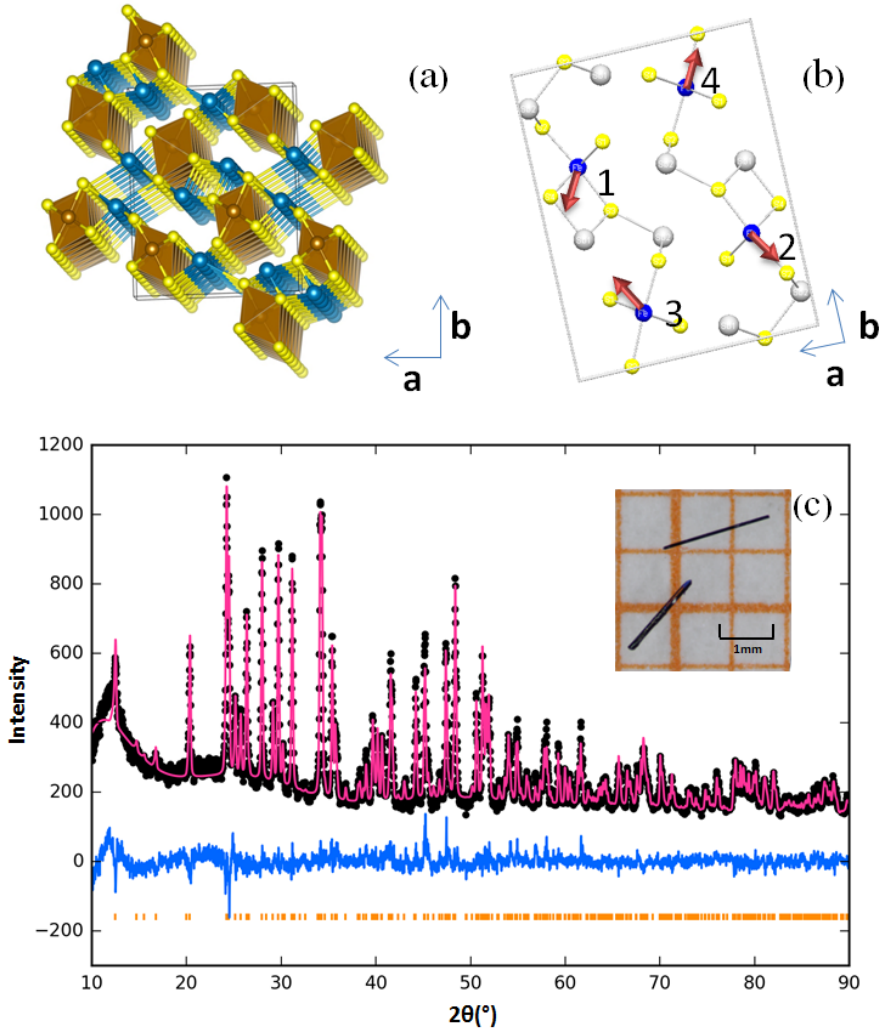

Figure 3.1: (a) The crystal structure of berthierite ($FeSb_2S_4$). Each Fe atom (brown) is surrounded by 6 S atoms (yellow) and forms a FeS_6 octahedral cell. The octahedral cells form a one-dimensional chain along the *c*-axis and the chains interact with each other via antimony atoms(blue) within the ab plane. (b) The magnetic structure of berthierite sample. Red arrows are magnetic moments on site 1-4. (c) The XRD pattern refinement of natural Berthierite ($FeSb_2S_4$) single crystals. Photo of natural berthierite single crystal samples is presented in the inset.

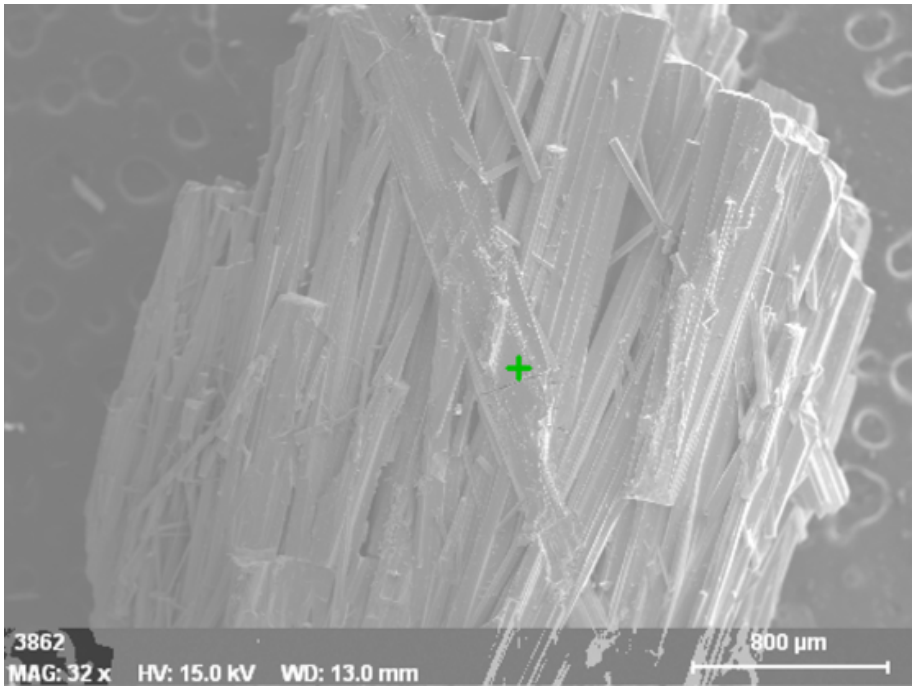

Figure 3.2: TEM image of natural berthierite. The corresponding EDS spectra are consistent with expected chemical composition.

Atoms	Distance(Å)	Bond	Length(Å)	Angle(°)
Fe1 - Fe1	3.763	Fe - S - Fe	2.509, 2.509	97.99
		Fe - S - Fe	2.616, 2.616	91.17
Fe1 - Fe2	8.810			
Fe1 - Fe3	7.483	S - Sb - S	2.708, 2.171	97.21
		Fe - S - Sb	2.492, 2.708	148.64
c		Fe - S - Sb	2.452, 2.171	114.61
		S - S	3.678	
Fe1 - Fe4	6.194	S - Sb - S	3.133, 2.171	86.49
		Fe - S - Sb	2.509, 3.133	106.27
		Fe - S - Sb	2.452, 2.171	119.81
		S - S	3.701	

Table 3.1: Structural parameters of Bertherite single crystals.

3.3.2 Resistivity

The resistivity data were measured from 300 K to 2 K with current (0.01 mA) applied both parallel and perpendicular to *c*-axis. Low-temperature data were not able to be collected because the resistance was too large and out of measurement range. Unlike the metal-insulator transition observed by Yu in synthetic single crystals [19], the resistance shows pure insulator behavior in both directions. The data was fitted with typical insulator resistivity formula $\rho = \rho_0 exp(-\frac{\Delta}{k_B T})$ with an energy gap of $\Delta = 0.3$ eV.

3.3.3 Magnetic susceptibility

Both ZFC and FC susceptibility temperature dependence of natural single crystal samples were taken in a constant field of 100 Oe from 300 K to 2 K. Data were collected with fields applied both parallel and perpendicular to the crystallographic *c*-axis. Unlike the transition temperature (50-70 K) reported by Yu *et al.* [19], the magnetic susceptibility data dropped by around 30% with a broad peak at around 50K with field applied along c-axis. The transition temperature is consistent with other measurement taken from natural samples. While it only dropped around 10% at the same temperature when the field is perpendicular to c-axis. Also, the upturn of the susceptibility below 25 K is more obvious when the field is perpendicular to c-axis. The result indicates an antiferromagnetic transition at 50 K with strong anisotropy. The high temperature region were fitted by Curie-Weiss law, with θ = 200 K, μ_{eff} = 4.7 μB when the field is along *c*-axis and θ = 290 K, μ_{eff} =

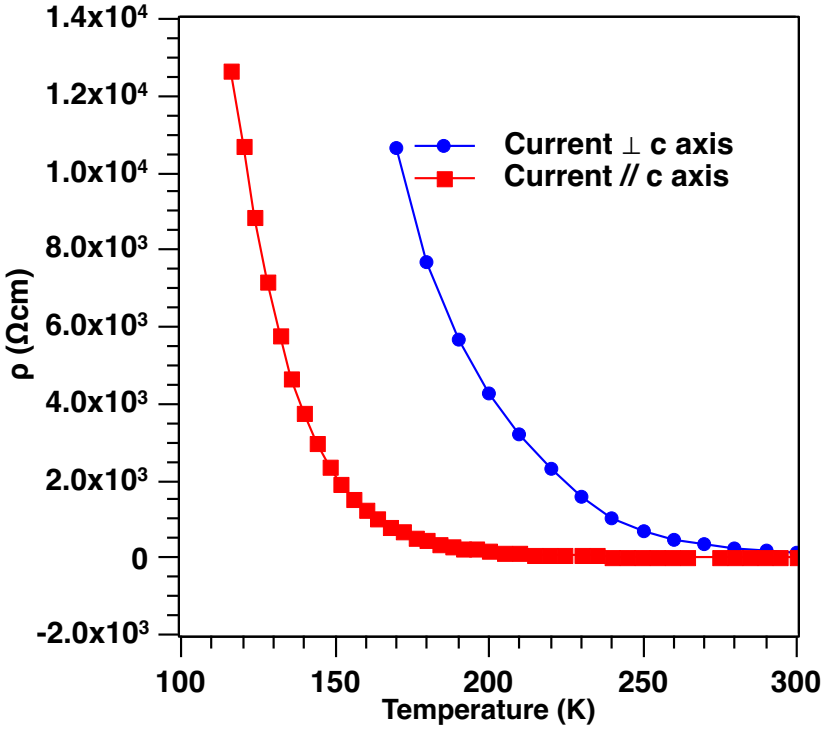

Figure 3.3: The resistivity of $FeSb_2S_4$ sample with current parallel and perpendicular to the c-axis. The sample has insulating properties for both conditions. The data were fit by typical insulator model $\rho = \rho_0 exp(-\Delta/k_B T)$, with an energy gap $\Delta =$ 0.3 eV.

4.7 μB when the field is perpendicular to c-axis. The transition temperature, Curie temperature and magnetic moment are well consistent with Winterberg's paper [20]. The magnetic moment reveals the Fe atoms are in Fe^{2+} states with $S = 2$.

The broad peaks in our susceptibility measurement always show in some quasi-one-dimensional antiferromagnet. The magnetic susceptibility data were fitted with Bonner-Fisher Model (Equation.3.1), which are often used to describe the quasi-one-dimensional antiferromagnetic systems with anisotropic coupling. N is the Avogadro constant, k_B is the Boltzmann constant, g is Landé factor, and J is the antiferromagnetic exchange constant coupling nearest neighbors along the chain, S equals 2 for Fe^{2+}. The expression of the function u(K) and K are shown in Equation.3.2.

$$\chi_{BF} = \frac{N_A S(S+1)}{3k_B T} g^2 \mu_B^2 \frac{1+u(K)}{1-u(K)} \tag{3.1}$$

$$u(K) = coth(K) - \frac{1}{K}; K = \frac{2JS(S+1)}{k_B T} \tag{3.2}$$

The interaction parameter J is approximate -12 K and g = 1.9 when the field is parallel to the c-axis. In one-dimensional antiferromagnetic systems, both intra-chain and inter-chain couplings, referred as J and J′ respectively, should be considered. Oguchi *et al.* has derived the following relationship from the Green function method as shown in Equation 3.3 and Equation 3.4 [22], where η = J′/J.

$$\frac{kT_N}{|J_1|} = \frac{4S(S+1)/3}{I(\eta)} \tag{3.3}$$

$$I(\eta) = \frac{1}{\pi^3} \int\int\int_0^\pi \frac{dq_a\, dq_b\, dq_c}{(1-\cos q_a)\eta + (1-\cos q_b)\eta + (1-\cos q_c)} \tag{3.4}$$

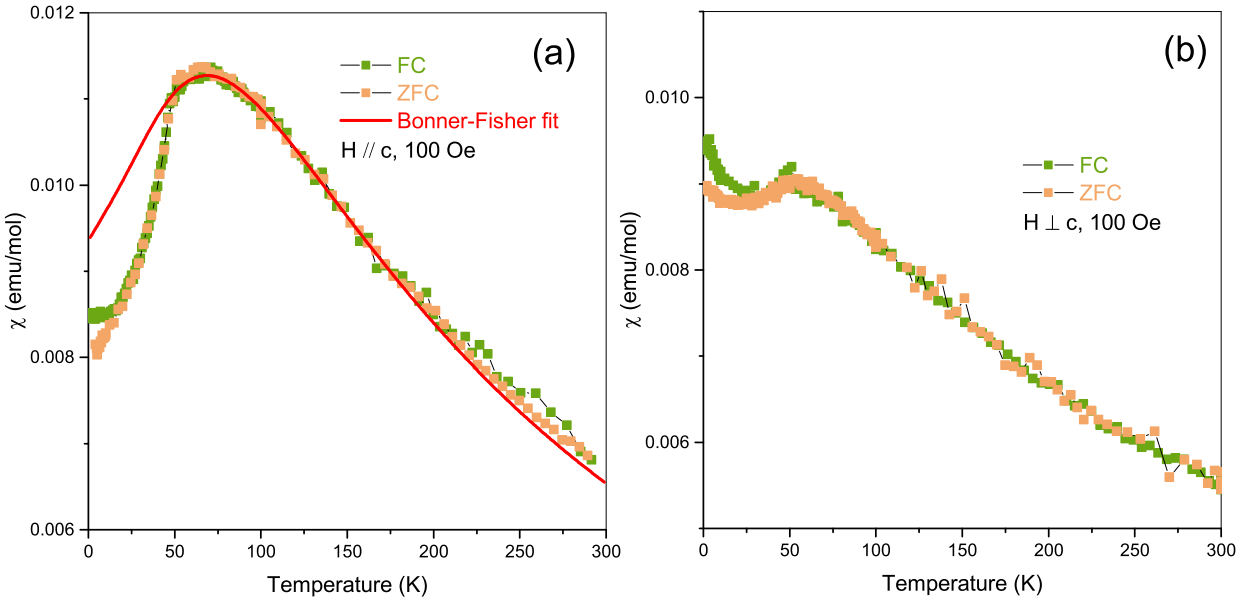

Figure 3.4: The magnetic susceptibility of berthierite. The red curve in (a) is Bonner-Fisher fit for Spin-2 one dimensional AFM chain.

An interpolation formula was proposed by Amy *et al.* [23], $I(\eta) \approx 0.64/\sqrt{\eta}$. Substitute our experiment data into the formula, we have an estimation of the inter-chain coupling of J′ = -0.89 K. The ratio of J′/J is approximately 0.074.

3.3.4 Heat capacity

Heat capacity data were taken from 150 K to 2 K. The results are displayed in Figure 3.4(a). The data show a more obvious λ-abnormally centered at around 40 K compared with Yu's paper, corresponding to the antiferromagnetic transition. The high-temperature part data were fitted by the Debye model with two Debye terms with Debye temperature Θ_1 = 220 K, Θ_2 = 355 K of weight 2.2 and 5.4 respectively. As shown in Figure 3.4(b), the magnetic heat capacity was calculated by subtracting the fitted data, the cumulative entropy was also calculated by integrat-

ing the magnetic heat capacity over temperature. The $S = 12.5$ J/mol is smaller than the theoretical value $R\ln(2S+1) = 13.38$ J/mol, where $S = 2$ and R is the gas constant. The smaller cumulative entropy is probably due to the long-range order in the magnetic structure.

The heat capacity of crystal comes from the contributions of phonons and magnetic excitations. At the low-temperature range, the phonon heat capacity follows the Debye-T^3 power law. The magnetic heat capacity depends on both the spin-wave dispersion relation and the dimensionality of the system. The magnetic heat capacity of an antiferromagnet is proportional to T^{δ}, where δ is the dimensionality of the lattice. The C/T versus T^2 ranging from 2 K to 10 K are presented in the inset of Figure 3.6. The low temperature region cannot be fitted with one T^3 term correctly. The lattice T^3 heat capacity at low temperature are estimated based on the fitting data. A magnetic heat capacity C_m proportional to $T^{1.42}$ at the low-temperature range are determined by subtracting the T^3 term from the experiment data.

3.3.5 Field-dependent magnetic susceptibility

The field scan data were taken from 0 to 6.5 T at 2 K (below the transition), 20 K (below the transition), 80 K (above the transition) with field applied both parallel and perpendicular to the c-axis, as shown in Figure 3.7. The M-H curve increased linearly when the field applied parallel to the c-axis, the linear dependence is consistent with Yu's result. The magnetization saturates at the higher field when the field

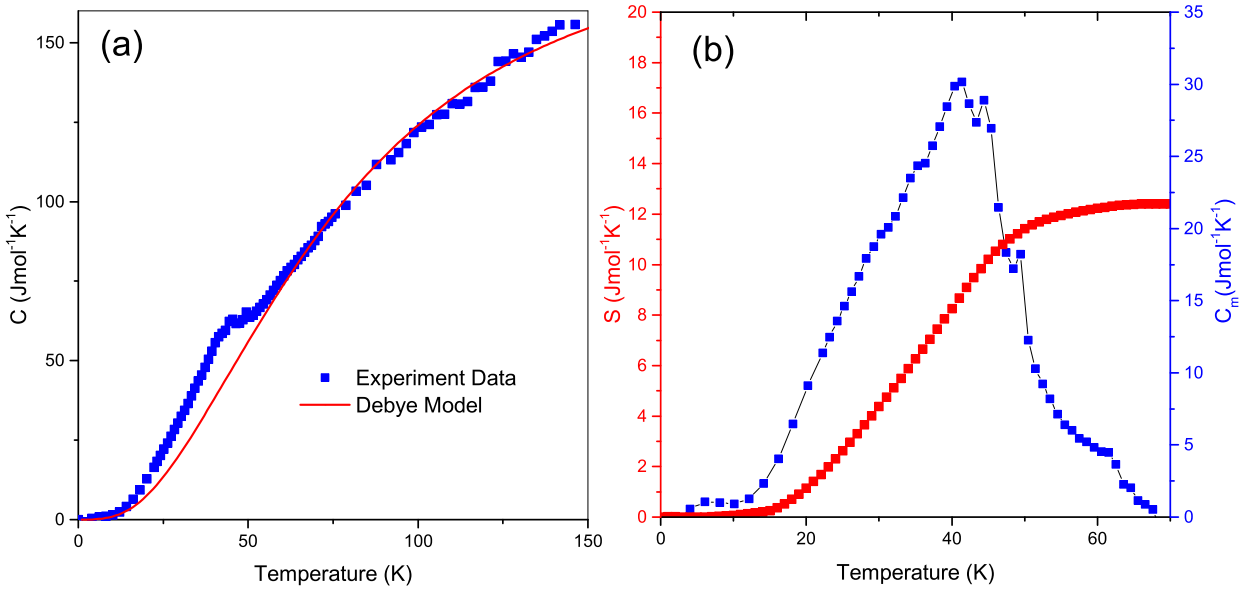

Figure 3.5: (a)Heat capacity data of berthierite, the red curve is the phonon term fitted by Debye model. (b) The magnetic heat capacity and the cumulative entropy.

is parallel to the c-axis. The magnetization shows strong anisotropic character with the field applied to the different direction. Similar properties are also discovered in linear chain ferromagnetic transition metal oxides such as $CuAs_2O_4$ [24], c-axis is the magnetic easy axis of the system with a larger intra-chain coupling compared with inter-chain coupling.The anisotropic magnetism is also consistent with the magnetic structure deduced from the neutron experiment. The long-range order perpendicular to the c-axis contributes some ferromagnetic order to the system, which is also shown in the susceptibility temperature dependence and previous research.

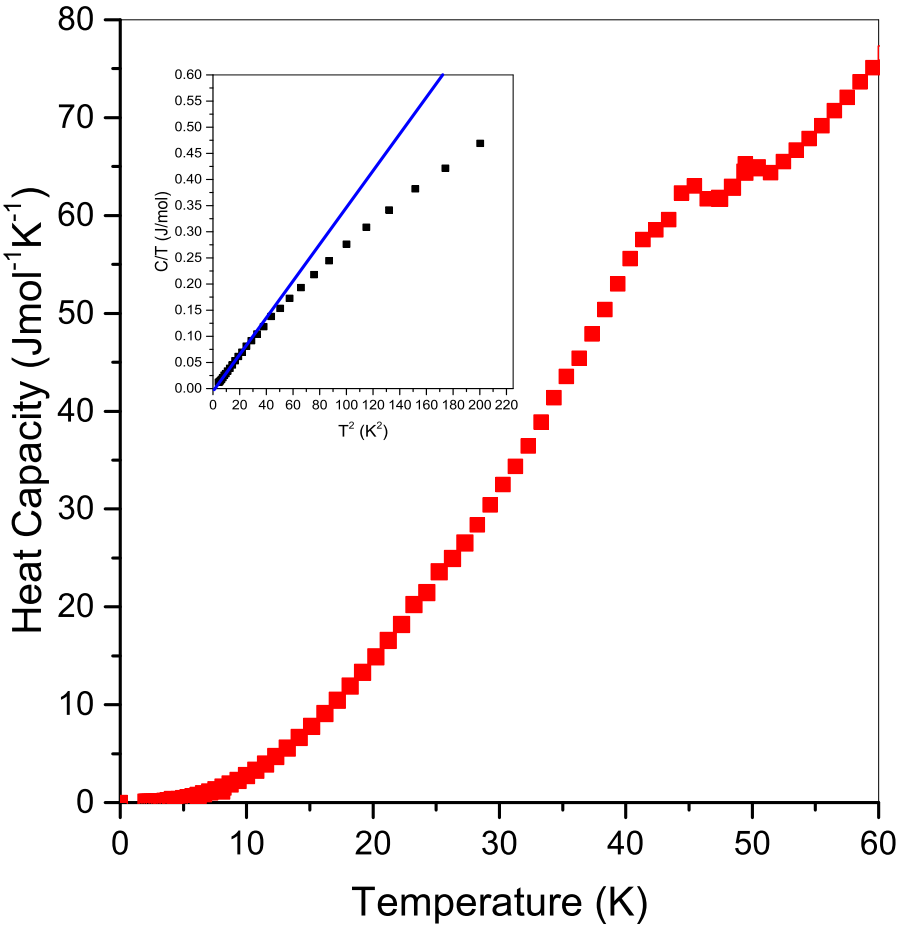

Figure 3.6: The heat capacity of berthierite from 2K to 60K. There are two small peaks across the transition, the reason for the two small peaks is not clear. C/T versus T^2 is presented from 2K to 10K in the inset.

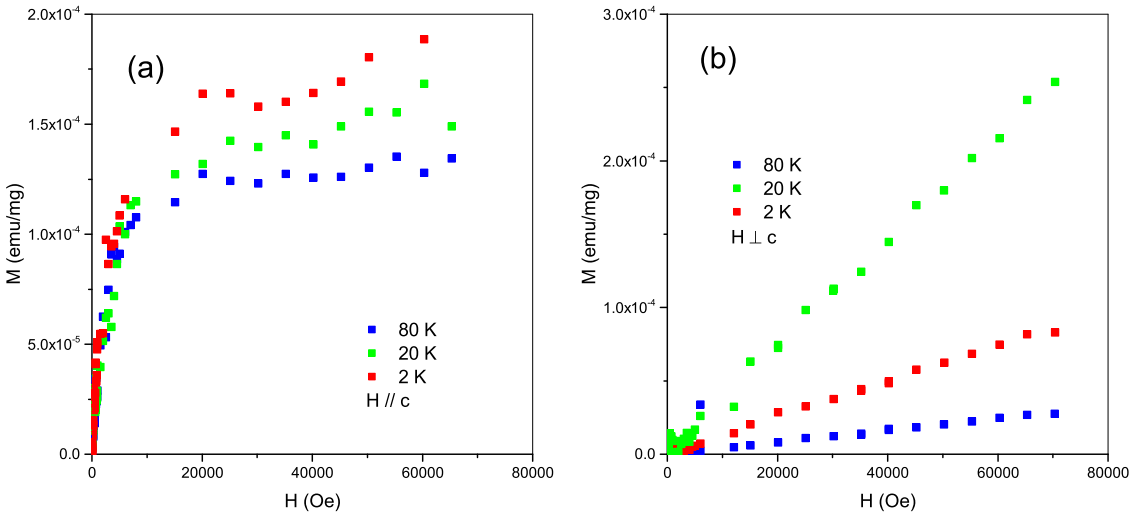

Figure 3.7: The M-H curve of $FeSb_2S_4$ at 2 K, 20 K and 80 K with field applied both parallel and perpendicular to c-axis.

3.4 DFT calculation

The density functional calculation was done with help from Xiuquan Zhou. I provided the crystallographic information file, and he helped me run the calculation on the server. We analyzed the results together. All density functional theory (DFT) [25, 26] calculations were performed by using the Vienna Ab-initio Simulation Package (VASP) [27–30] software package with potentials using the projector augmented wave (PAW) [31] method. The exchange and correlation functional were treated by generalized gradient approximation (PBE-GGA) [32]. The cut-off energy, 450 eV, was applied to the valance electronic wave functions expanded in a plane-wave basis set for all chalcogenides. A Monkhorst-Pack [33] generated 23×23×17 k-point grid was used for the Brillouin-zone integration to obtain accurate electronic structures. As shown in Figure 3.7, the band gap is consistent with the value of 0.3

eV we got from the resistivity measurement fitting. The density of state (DOS) was shown in Figure 3.7(b), the iron atoms on site 1 and site 3 (Fe1), site 4 and site 2 (Fe2) are the same, while the density is opposite between Fe1 and Fe2. Due to the crystal field effect, the d orbitals of the Fe atoms split into e_g and t_{2g} orbitals. A further splitting in eg and t2g orbitals make the d_{xz}, and d_{yz} have lower energy. The magnetic moments of orbital d_{xz} and d_{yz} with larger DOS dominate the total AFM interaction. Electrons of orbital d_{xz} and d_{yz} Fe atoms are polarized to c-axis. Two Fe atoms form strong coupling via superexchange interaction with the sharing S atoms within the c-axis, leading to a quasi-one-dimensional antiferromagnetism along the c-axis.

3.5 Conclusion

In summary, I did the transport measurement with temperature on natural berthierite single crystal samples and confirmed it as an Antiferromagnetic insulator. The magnetic susceptibility data were taken and analyzed. I gave an estimation of the inter- and intra-chain coupling. The T^{δ} dependence of the magnetic heat capacity strongly supports its low dimensional properties. I also observed the anisotropic magnetization perpendicular and parallelled to the magnetic easy axis which is well consistent with the magnetic structure and low dimensional character. In the end, we proposed the DFT calculation, the density of states shows the magnetic moment mainly comes from the d_{xz} and d_{yz} orbitals from the Fe atoms. The antiferromagnetism is probably due to the superexchange between Fe atoms via S atoms along the

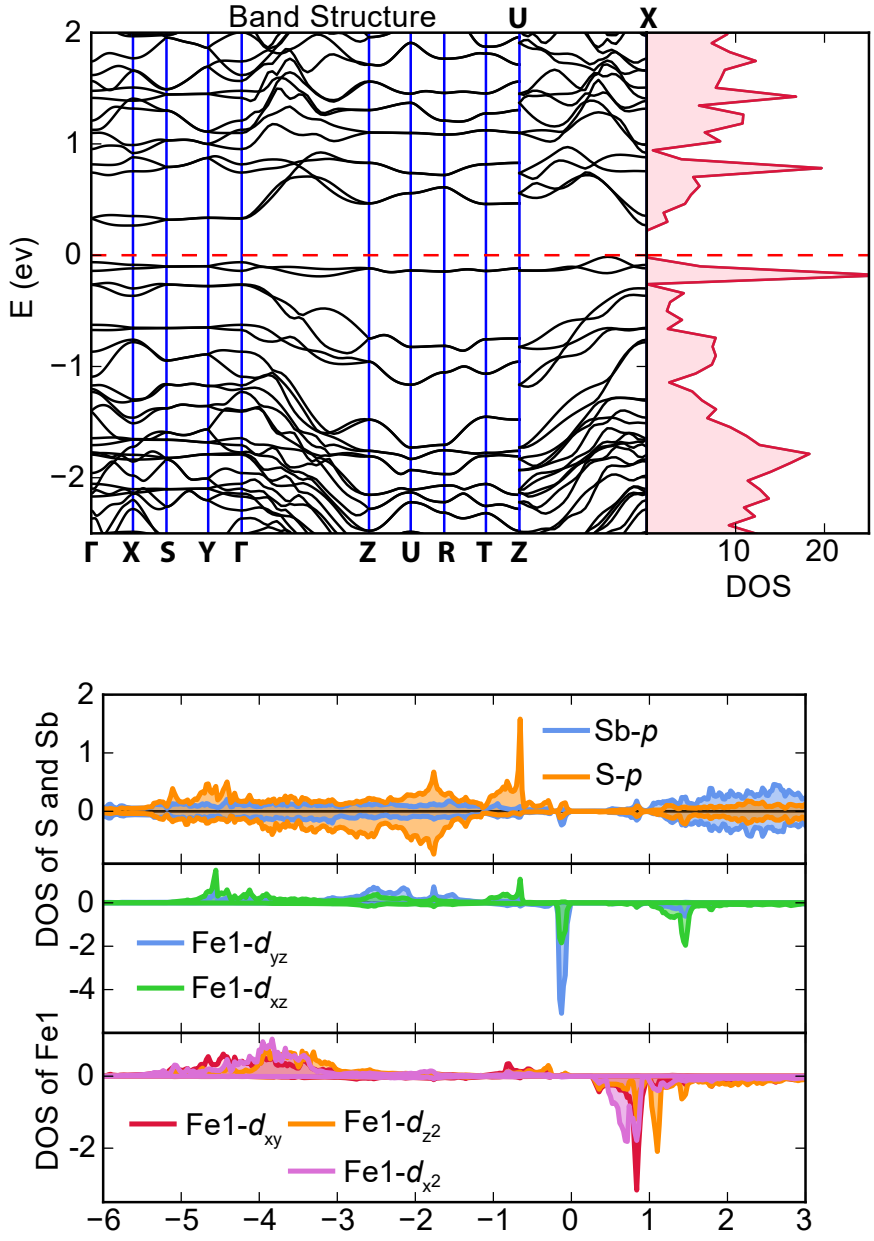

Figure 3.8: (The upper graph is the band structure and density of states(DOS) of berthierite. The lower one is the DOS of S atom, Sb atom, and Fe1 atom.

c-axis. The difference in some physical properties between natural mineral samples and the synthetic single crystals in Yu's paper is worthy of further research.

Chapter 4: Bornite (Cu_5FeS_4): Tuning the antiferromagnetic insulating state by applying pressure.

In this section, we will discuss a transition metal sulfide mineral bornite (Cu_5FeS_4) to show the possibility to find similar metal-insulator transition like transition metal oxides in transition metal sulfide. The results suggest transition metal sulfides with metal-insulator transition associated with magnetic transition may be a good candidate for searching natural superconductor as well as other strong correlated phenomena. I-Lin Liu helped me with the pressure measurement setup. And the X-ray data were collected by Dr. Ryan Stillwell from Lawrence Livermore National Laboratory. I measured the other transport data at CNAM and the neutron result at NIST.

4.1 Introduction

Materials with metal (semiconductor)-insulator transitions are of great interest with novel electronic and magnetic properties. In some strongly correlated systems, the magnetic or non-magnetic insulating states can be suppressed by chemical doping or applying pressure and associated by some unconventional phenomena like superconducting state. For instance, by applying pressure, superconducting state

shows up with suppression of the insulating states in the quasi-2D organic systems, $(TMTSF)_2X$ [34, 35]. In cuprate and iron-based superconductors, the antiferromagnetic states can also be suppressed by a hole or electron doping which lead to a superconducting dome [13, 36]. Many theories and models about metal-insulator transition and systems with metal-insulator transition were proposed, but searching new systems with the metal-insulator transition is still of great importance to physicists.

Transition metal oxide or sulfide compounds with mixed-valence state often exhibit a metal-insulator transition (MIT) with charge ordering. Some of the insulating ground states are non-magnetic. For example, Ti_4O_7 with Ti^{3+} and Ti^{4+} has a metal-insulator transition around 120 K associated with a structural phase transition [37,38]. CuIr2S4 experiences an MIT at 230 K associated with the charge ordering of the mixed-valent Ir ion and the formation of isomorphic octamers of Ir^{3+} and Ir^{4+} [39]. Meanwhile, some of the insulating ground states are ferromagnetic or antiferromagnetic. For instance, magnetite Fe_3O_4 with Fe^{2+} and Fe^{2+} exhibits magnetically ordered ground states [40, 41].

Bornite (Cu_5FeS_4) is a very famous mineral of considerable economic importance, also named as peacock ore with purple metallic luster. An antiferromagnetic transition at around 77 K was reported in the 1970s, and the magnetic properties of both natural and synthetic bornite have been studied with different experimental approach since 1977. Several explanations for the antiferromagnetic transition has been proposed. M.G. Townsend investigates the synthetic Cu_5FeS_4 and suggests that there is significant partial disordering of cations and vacancies in tetrahedral holes

of the face-centered cubic sulfur lattice, and thermoelectric power measurements indicate that bornite is a p-type semiconductor at room temperature. Mossbauer spectroscopy was taken with natural mineral from 12.8 K to 300 K by M. S. Jagadeesh. The data show the presence of high-spin Fe^{3+} and low-spin Fe^{2+}, whose concentrations change is a function of temperature (Fe^{2+} increases with increasing temperatures) [42]. Two possible magnetic structure was proposed by M. F. Collins *et al.* from the neutron diffraction data [43]. Compared with the magnetic properties, the low-temperature transport character of bornite has not been well studied. In this chapter, we analyzed the transport properties under pressure of natural bornite samples. A semiconductor-insulator transition associated with the magnetic transition is reported for the first time. The insulating state is actively suppressed by applying pressure up to 2.3 GPa with pressure cell. The high-pressure X-ray diffraction data reveals a structural transition at around 6.1 GPa. I also present our results of magnetic susceptibility, heat capacity, and neutron scattering experiments and compared our results with previous reports.

4.2 Experiments and Results

4.2.1 Crystals and X-ray diffraction

The natural bornite poly-crystal samples were provided by Department of Mineral Science, Smithsonian Institute. Natural bornite specimen has dark purple metallic luster. Powder x-ray diffraction data were collected with Rigaku MiniFlex X-ray diffractometer. The crystal structure of bornite has been well studied for a

wide temperature range. There exist three polymorphic forms of Cu_5FeS_4 [44–46]. Above 525K, bornite has a high-temperature cubic structure as shown in Figure 4.1 (a), each Cu(Fe) sites have an equal probability of vacancy. When the temperature is below 525K, the bornite sample goes into a metastable state. As temperature decreasing, the Cu and Fe atoms become ordered, *c*-axis loses its symmetry and results in a doubled unit cell and gradually change to an orthorhombic structure with space group *Pbca* and lattice constant $a = 10.95$ Å, $b = 21.862$ Å, c = 10.95 Å. The samples are in the low-temperature orthorhombic structure in our measurements. The refined X-ray diffraction pattern is shown in Figure 4.2, the structure of the natural samples are well consistent with the orthorhombic structure and of excellent quality.

4.2.2 Magnetic susceptibility

The magnetic susceptibility was measured with Quantum design Magnetic Property Measurement System(MPMS) under 100 Oe from 2 K to 300 K with both zero field cooling and field cooling. The magnetic structure has been well investigated before. An antiferromagnetic transition at 750 K was first discovered by from the susceptibility temperature dependence. As shown in Figure 4.3, our susceptibility data is well consistent with the previous data. The magnetization decreased when the temperature is below 70 K. Curie-Weiss analysis gives a magnetic moment of 4.7 μB, which is consistent with the report by Koto *et al.* as well as the results by Collins *et al.* from neutron experiment [43, 45]. There is a small increase

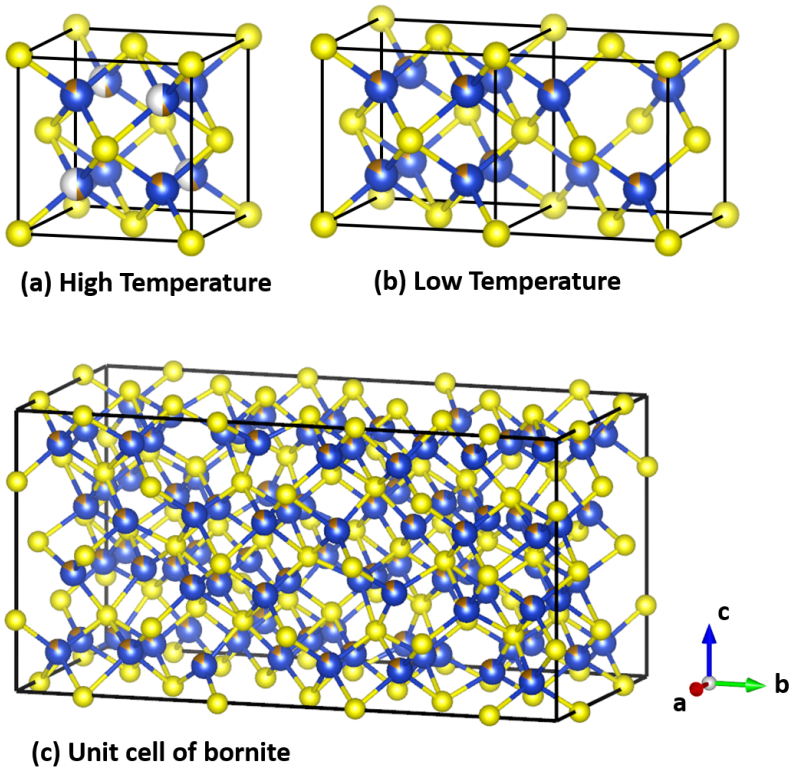

Figure 4.1: The unit cell of bornite samples. (a) One sublattice of the high temperature (above 525 K) cubic structure, four of which with different direction forms a unit cell. (b) One sublattice of the low-temperature orthorhombic structure. (c) The unit cell of the low-temperature structure of bornite.

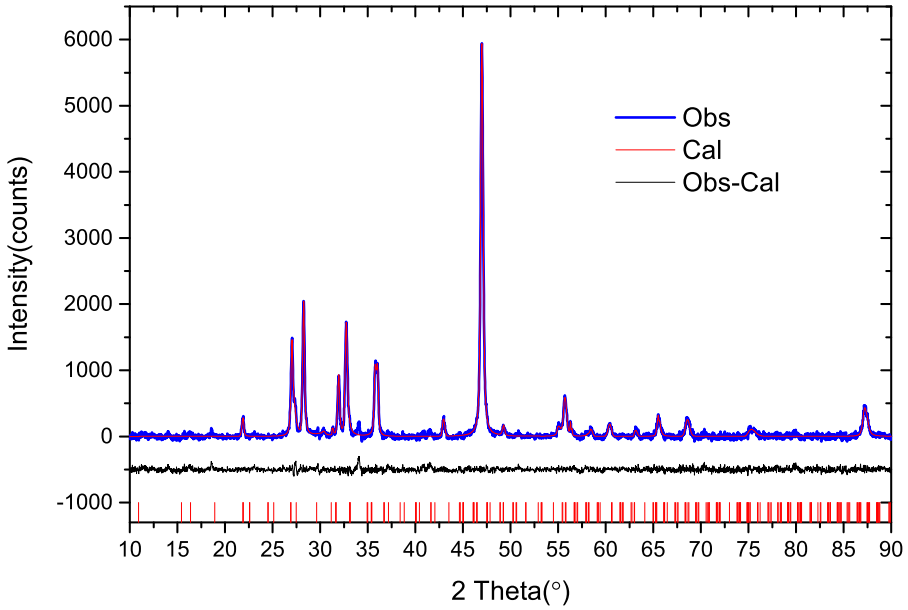

Figure 4.2: The X-ray diffraction pattern of natural bornite samples.

of magnetization at around 8 K, also reported by Collins *et al.*, which is probably due to the spin rotation.

4.2.3 Heat capacity

The heat capacity and entropy of natural bornite samples were measured by Robie from 5 K to 351 K measured by quasi-adiabatic calorimeter and from 338 K and 761 K by differential-scanning calorimetry [47]. The heat capacity of natural bornite shows a λ-type anomaly at 65 K associated with the antiferromagnetic transition of the spins of the Fe^{3+} ions. The heat capacity also exhibits a broad hump between l40 K and 255 K which may be caused by charge transfer involving Fe^{2+} - Fe^{3+} and Cu^{+} - Cu^{2+}. I also measured heat capacity in a larger temperature range from 2K to 300K with PPMS. As shown in Figure 4.4, the low-temperature data around 50K is similar to the Collins' measurement.

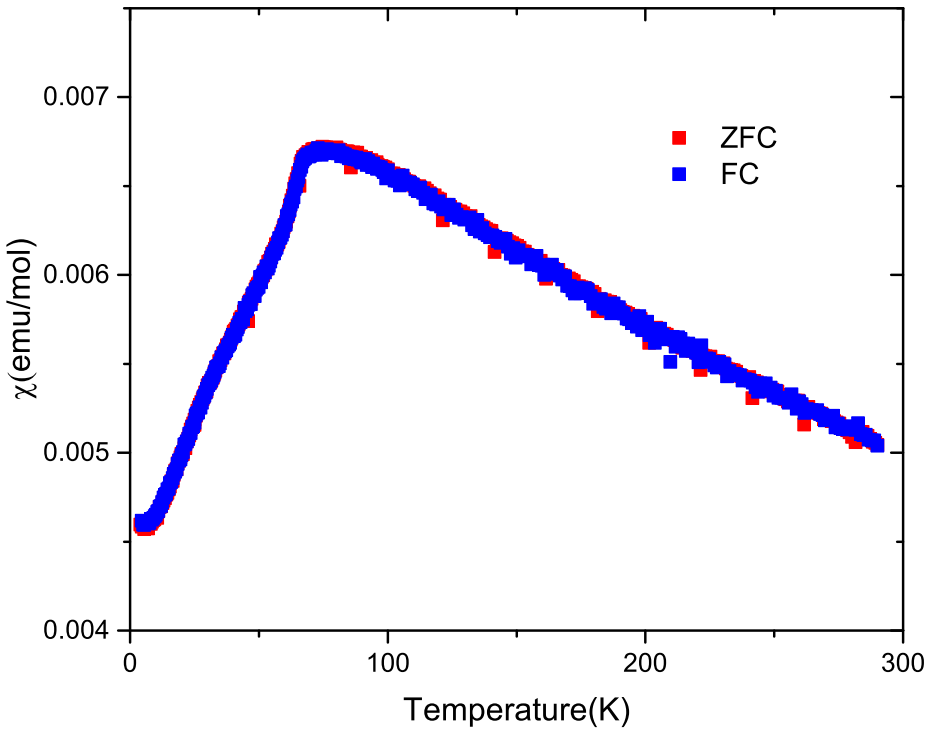

Figure 4.3: Susceptibility temperature dependence of natural bornite samples. The decrease at 70 K corresponds to the AFM transition. There is another small upturn at 8 K which is also mentioned in previous papers.

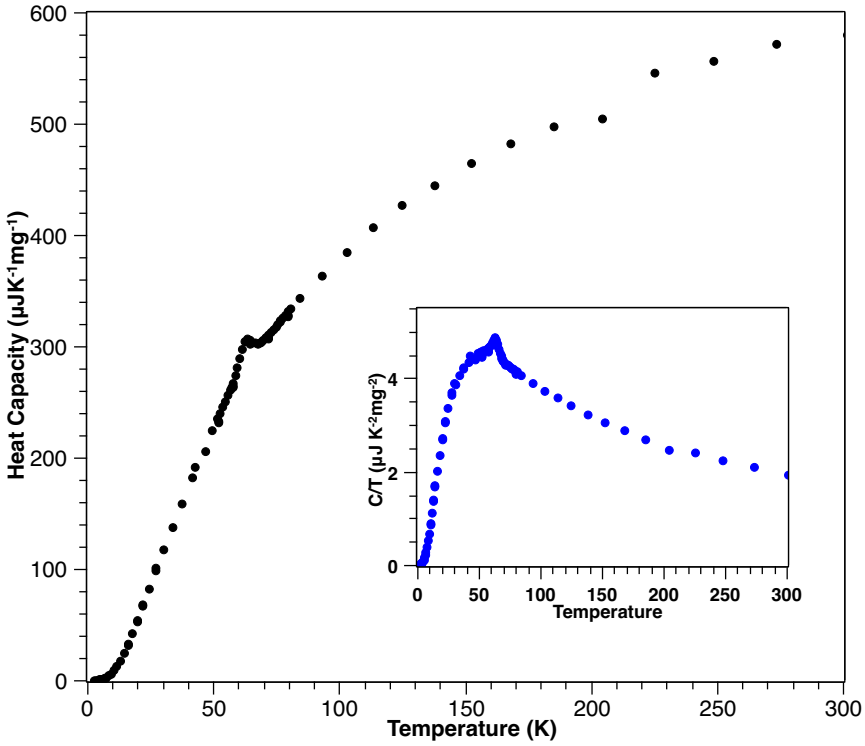

Figure 4.4: Heat Capacity of natural bornite from 2 K to 100 K, the inset is temperature dependence of C/T from 2 K to 300 K.

4.2.4 Neutron diffraction

The neutron diffraction data were taken with BT-1 High-Resolution Powder Diffractometer at NIST Center for Neutron Research (NCNR). Diffraction patterns of 2.5 K, 50 K and 300 K were collected with Ge(311) monochromator, wavelength λ = 2.079 Å. Compared with the neutron diffraction data of natural bornite samples at 4.2 K, 18 K and 300 K using 1.40 Åneutron source measured by M.F.Collins *et al.* [43], we detected more magnetic peaks and had better data below the 8 K transition. As shown in Figure 4.5, the neutron diffraction patterns are plotted. The peaks at 10.9, 12.2, 15.4, 22.7, 27.6 and 33.2°of 2.5 K and 50 K data are not apparent in the 90 K measurement. The magnetic diffraction pattern is calculated by subtracting the 90 K data from the 50 K data. Most of the magnetic peaks are the same as the peaks from planes in the unit cell. I couldn't get exquisite refinement with the several magnetic structures proposed by M.F.Collins *et al.* [43], only several magnetic peaks can be fitted. The magnetic structure of bornite should be more complex. The 10.9 and 15.4°peaks correspond to (0, 2, 0) and (0, 2, 1) plane; the 12.2°peak may come from a new sub-lattice due to the antiferromagnetic ordering. The intensity of these three peaks increases with temperature decreasing, which is probably due to the formation of the magnetic ordering. However, I couldn't get good enough magnetic structure refinement because of the complexity of the unit cell.

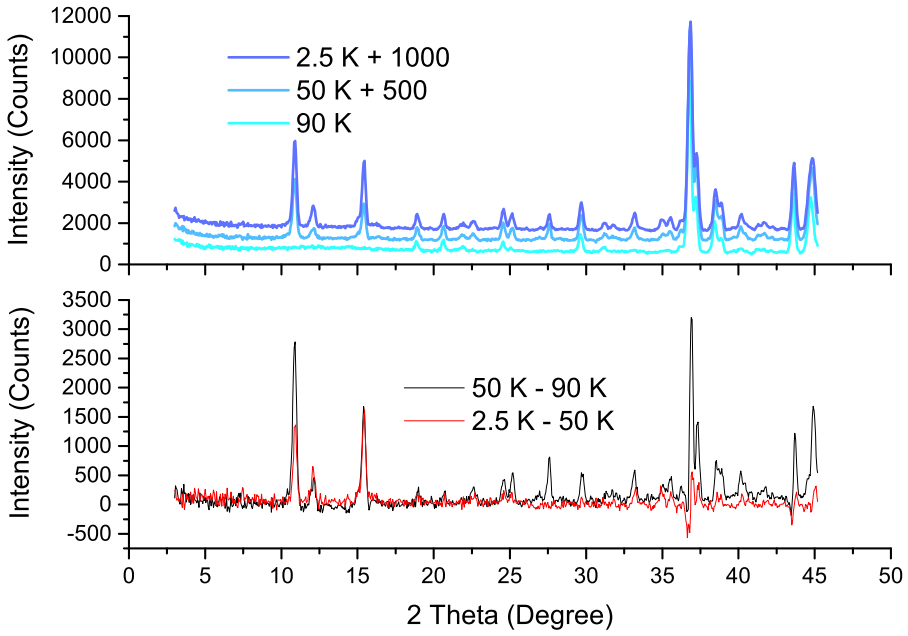

Figure 4.5: Neutron patterns of natural bornite samples at 2.5 K, 50 K, and 90 K. The second plot shows the difference between patterns.

4.2.5 Resistivity and Pressure

The resistivity data under pressure were taken in a piston-cylinder pressure cell (C&T Factory CTF-HHPC50) using 1:1 ratio mixture of 1-methyl-3-butanol and n-pentane as a hydrostatic medium, with Quantum Design Physical Property Measurement System (PPMS), from 2K to 300K with zero fields. The measurement method is a traditional 4-wire method.

As shown in Figure 4.6, the sample is put in a piston-cylinder pressure cell immersed in pressure medium. By applying pressure on the top of the pressure cell, the pressure medium will be compressed so that the pressure will be applied evenly to the sample. The exact pressure is confirmed with a superconducting

Figure 4.6: The 4-wire resistivity measurement setup for natural bornite sample. The shiny yellow parts are gold thin film fabricated by PVD method; the wires are connected to the gold parts with silver epoxy. The sample is located in the cell which will be filled with pressure medium during the experiment.

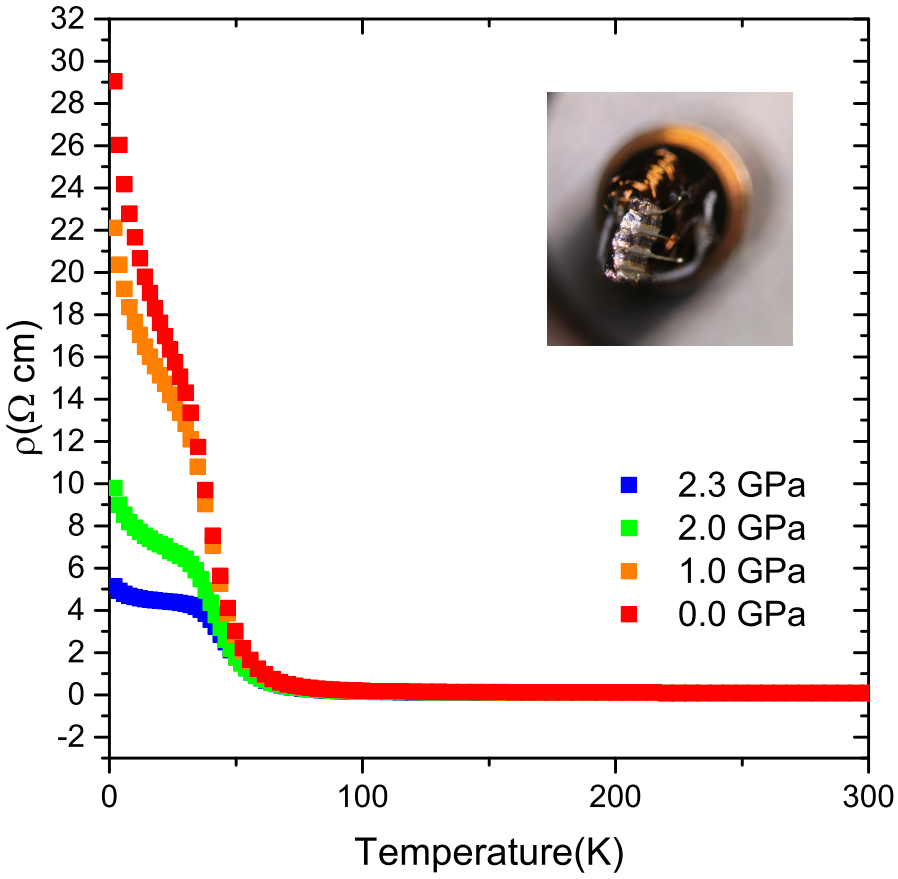

Figure 4.7: Resistivity of natural bornite sample under 0, 1.0, 2.0 and 2.3 GPa. The inset is the photo of the contact.

transition temperature of a lead sample in the pressure medium. We can apply up to a maximum pressure of 2.3 GPa with the setup. Unlike the measurement of ambient pressure without pressure cell, the contact has to be very strong to avoid detaching from the sample while applying pressure. So silver epoxy is used for making contact instead of silver paint, while the contact resistance is extremely large, up to 1000 Ohm. The Ag ions in the silver epoxy may react with the S atoms in the mineral. I fabricate four gold contact points with a thickness of 100nm by using the physical vapor deposition (PVD) to avoid the reaction and then connect gold wires to the gold contact points with silver epoxy. With this preparation, I was able to decrease the contact resistance down to less than 1 Ohm. The photo of the sample is shown in the inset of Figure 4.7.

As shown in Figure 4.7, the resistance of the natural bornite sample decreases dramatically with increasing pressure. A linear regression of the band gap size with pressure was made and gave an estimation of 3.0 GPa to suppress the insulating state to metallic state. However, we cannot get to 3.0 GPa with our pressure cell.

Density function (DFT) calculation was conducted to study the density of states (DOS) of the spin-up and down Fe ions with Vienna Ab initio simulation package (VASP). The cubic (high temperature) structure was used in the calculation instead of the orthorhombic (low temperature) structure for simplicity. The two structures are very close as I mentioned above. The DOS shows a metallic ground state instead of the insulating state in our experiment. The insulating state may come from charge order state associated with the antiferromagnetic order. The system is probably a Mott insulator.

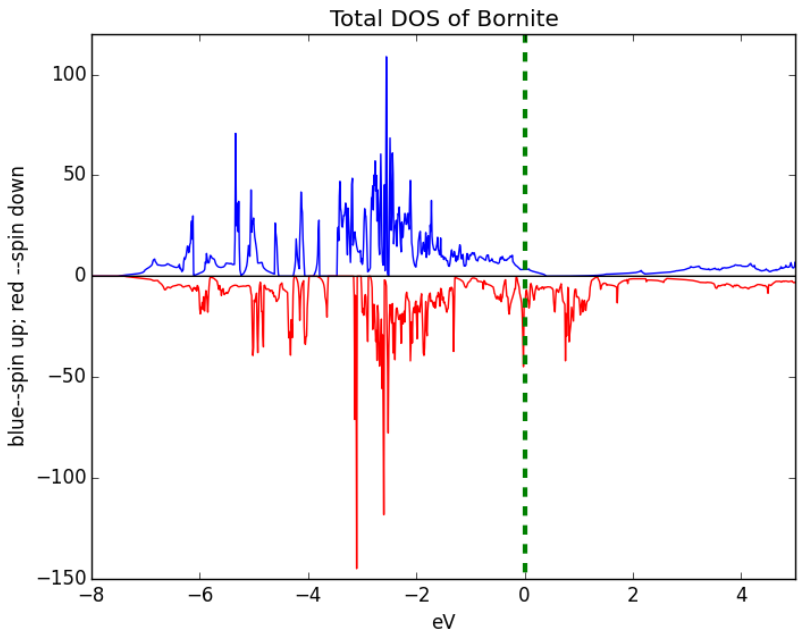

Figure 4.8: The density of states of cubic(high-temperature structure) bornite. The blue data are the spin up Fe atoms and red data are spin down Fe atoms. The Fermi energy is in the band.

4.3 High Pressure X-ray powder diffraction

High-pressure X-ray powder diffraction data of natural bornite sample from 4.7 GPa to 40.5 GPa were recorded on a MAR3000 imaging plate detector. The sample was contained in a diamond anvil cell (DAC). The wavelength of the radiation was 0.4133 Å(30keV).

The diffraction patterns are presented with corresponding pressure in Figure 4.9. The change at around 6.5 GPa indicates a structural phase transition in bornite sample. It is necessary to do further research about the structure and physical properties of the high-pressure phase.

The lattice parameters were calculated with the XRD patterns. As shown in Figure 4.10, the volume of the unit cell doesn't change much below 5.2 GPa. The unit cell shrinks along a and b axis and expands along the c axis. When the pressure is above 5.2 GPa, the lattice parameters changes significantly which results in a structural phase transition above 6.1 GPa.

4.4 Conclusion

I studied the transport properties under pressure of natural bornite samples. A semiconductor-insulator transition associated with an antiferromagnetic transition at 70 K is reported for the first time. Since the DOS of the cubic bornite gives a metallic ground state, the antiferromagnetic insulating state may be a Mott insulator with mix-valenced transition metal atoms. The semiconductor-insulator transition

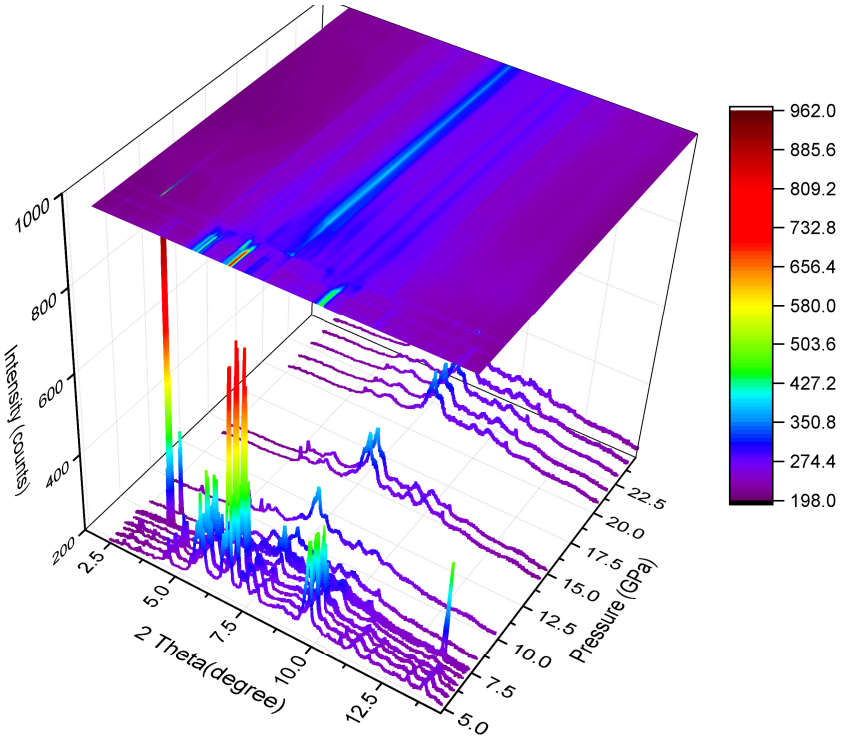

Figure 4.9: The X-ray diffraction patterns of different pressures.

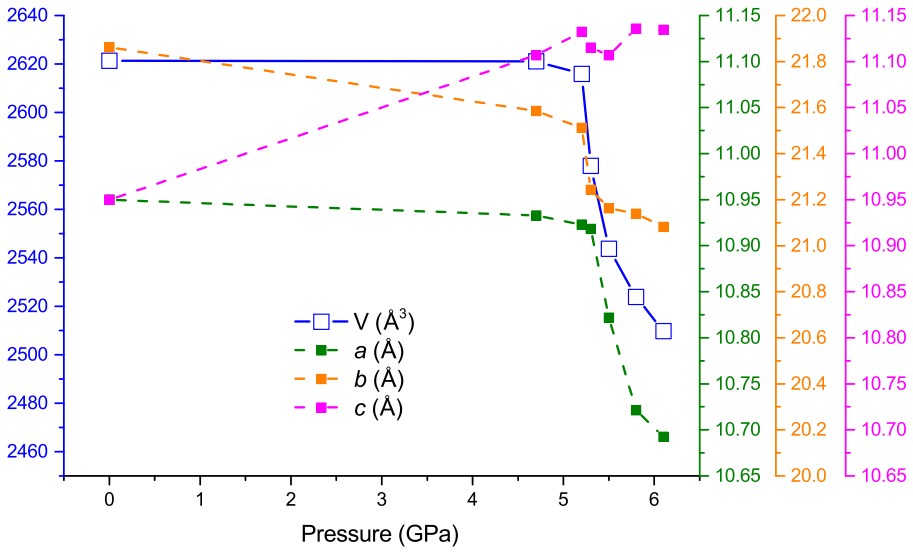

Figure 4.10: The lattice parameters and volumne of unit cell under different pressures.

is because of the charge ordering introduced by the AFM order. The insulating state can be strongly suppressed by applying pressure up to 2.3 GPa. The insulating state is estimated to become metallic at around 3.0 GPa. High-pressure X-ray diffraction data reveals a structural transition at around 6.1 GPa. The magnetic susceptibility and heat capacity data are well consistent with previous studies. Neutron scattering result shows several magnetic peaks, but the magnetic structure is still not clear.

Our research provides a candidate for pressure study of MIT transition. Transport properties above 2.3 GPa will be measured in the future. Also, more experiments will be conducted to study the magnetic structure of bornite as well as the new structural phase transition at 6.1 GPa.

Chapter 5: Nagyagite ($Pb_5Au(Te,Sb)_4S_{5-8}$): A natural 2D material with topological properties.

In this section, I will present our results about another transition metal sulfides nagyagite ($Pb_5Au(Te,\ Sb)_4S_{5-8}$). My conclusion will show that in some mineral systems, there may exist some quantum phenomena related to topological concepts. All the measurement and analyze were done by myself.

5.1 Introduction

During recent years, there are a large number of observations of ferromagnetism associated with doping of nonmagnetic material into non-magnetic oxides [48, 49], especially in some low dimensional materials [50]. The ferromagnetism has been named as d^0 ferromagnetism because the magnetism is probably not from partially filled d-orbitals, but from moments induced in the p-orbitals of the oxygen band [51]. Even in cases where there are partially filled d-orbitals, discrepancies between bulk measurements indicating ferromagnetism, and microscopic analyses by X-ray magnetic circular dichroism (XMCD) finding paramagnetic transition metal ions, have suggested that the ferromagnetism comes from vacancies in the oxygen lattices. The d^0 ferromagnetism is used to explain some of the ferromagnetic ma-

terials without magnetic atoms. But the theory is still under debating. Besides the exotic magnetic properties, low dimensional systems are of great interest due to many other reasons.

In recent years, extensive studies have been conducted in investigating the 2D election gas related to topological physics such as GaAs and HgTe quantum wells [52, 53]. A lot of 2D systems like thin films have been developed with different techniques. More interesting physical properties can be expected in similar systems with a sufficiently strong spin-orbital coupling (SOC) such as the naturally formed crystalline 2D structure that adopts a structure similar to those of lab-made thin films. A strong advantage of naturally formed 2D structure is that a large number of organic and inorganic materials adopt this type of structure. These natural occurring materials provide a parallel platform to uncover novel quantum phenomena derived from strong SOC, inversion symmetry breaking as well as novel magnetism. For example, Lei Fang have studied the transport properties of natural and synthetic $[Pb_2BiS_3][AuTe_2]$ samples [54, 55]. The naturally occurring material is called buckhornite, in which Au and Te atoms form a planar pseudo-square net sandwiched between the Pb_2BiS_3 layers. Large SOC strength and weak antilocalization were reported in the 2D heterostructure [Pb2BiS3][AuTe2], the ab-initial calculation suggested helical-like spin textures and spin-flips at the Fermi surfaces. In this subsection, I will present the transport properties of a naturally occurring material nagyagite ($[Pb(Pb, Sb)S_2][(Au, Te)]$) with a similar 2D structure of the buckhornite. Also, I studied the magnetic properties of the natural compound. A ferromagnetic-like transition at around the 30 K will also be discussed. Due to the low transition

temperature, most of the magnetic impurities can be excluded. I didn't see any magnetic atoms from the energy dispersive x-ray spectrometer (EDS) data. One possible reason for the transition may occur with a tiny amount of magnetic atoms doped in the system. Another possible reason is that is no magnetic atoms; the transition comes from d^0 ferromagnetism induced by the low dimensional structure and vacancies in the material. It worth further investigating by controlling the Au-Te composition or magnetic doping with synthetic nagyagite samples as well as first principle calculation.

5.2 Experiments

Nagyagite single crystal samples were taken from Department of Mineral Sciences, Smithsonian Institution. The origin of the specimen is from Nagyag, Romania; the place nagyagite was first discovered. Powder x-ray diffraction data were collected with Rigaku MiniFlex X-ray diffractometer. Energy dispersive X-ray spectroscopy (EDS) and transmission electron microscopy (TEM) photo was taken at Nanocenter at University of Maryland, College Park. Temperature susceptibility relation data from 300 K to 4 K and the magnetic isotherm measurement at a various temperature up to 7 T were measured with Quantum Design Magnetic Property Measurement System (MPMS). The temperature dependence of resistivity was measured on large bulk samples with four wires method in Quantum Design Physical Property Measurement System (PPMS).

5.3 Results and Disscusion

5.3.1 X-ray diffraction and EDS

Nagyagite was first discovered in 1789 by Werner from Nagyag Transylvania (now Nagyag, Romania) and named after the city (cited in Hintze (1904)). The structure of the material was unknown for a long time because of its complicated chemical composition. X-ray diffraction experiments on both natural and synthetic single crystal were conducted in 1999 [1], and the average structure was determined: space group $P2_1/m$, $a = 4.220(1)$ Å, $b = 4.176(1)$ Å, $c = 15.119(3)$ Å, $\beta = 95.42(3)°$, and Z = 2. As shown in Figure 5.1, Nagyagite has a clear 2D layer structure: slices of two slabs thick SnS-archetype with formula Pb(Pb, Sb)S2 parallel to (001) have a thickness of 9.15 Å. Te and Au forms a planar pseudo-square net that is sandwiched between the SnS-archetype layers; it is assumed that planar AuTe configurations are edge connected to chains and that Te atoms are in a zigzag arrangement.

EDS data was analyzed and presented with several other specimens from previous reports in Table 1. The chemical composition of the Au-Te layers and the Pb-Sb-S layers have strong sample dependence. While on average the gold tellurium ratio is from 0.25 to 0.5, so we may be able to make synthetic materials with $AuTe_2$ layers like the $[Pb_2BiS_3][AuTe_2]$, which has a robust spin-orbital coupling (SOC). We may also be able to study the SOC effect of Au-Te layers of different composition by controlling the gold tellurium ratio. As shown in the TEM photo in Figure 5.3, the natural occurring nagyagite crystal is always with some quartz (SiO_2), which is the

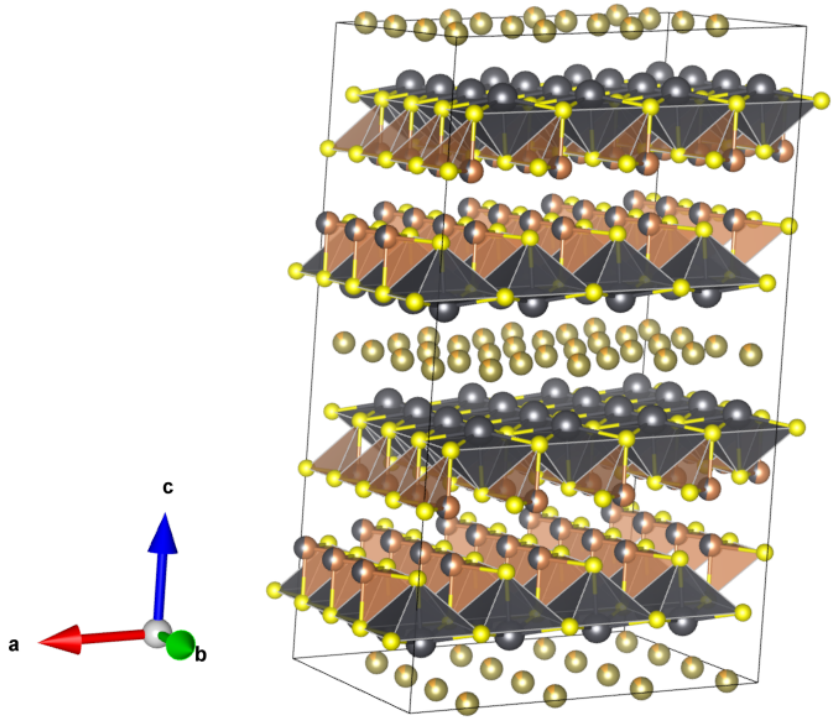

Figure 5.1: Structure of Nagyagite.The orange and gray balls are Au and Te atoms. The Au and Te atoms share the sites in the layers. The yellow balls are the S atoms, the brown ones are Sb atoms, and black ones are Pb atoms.

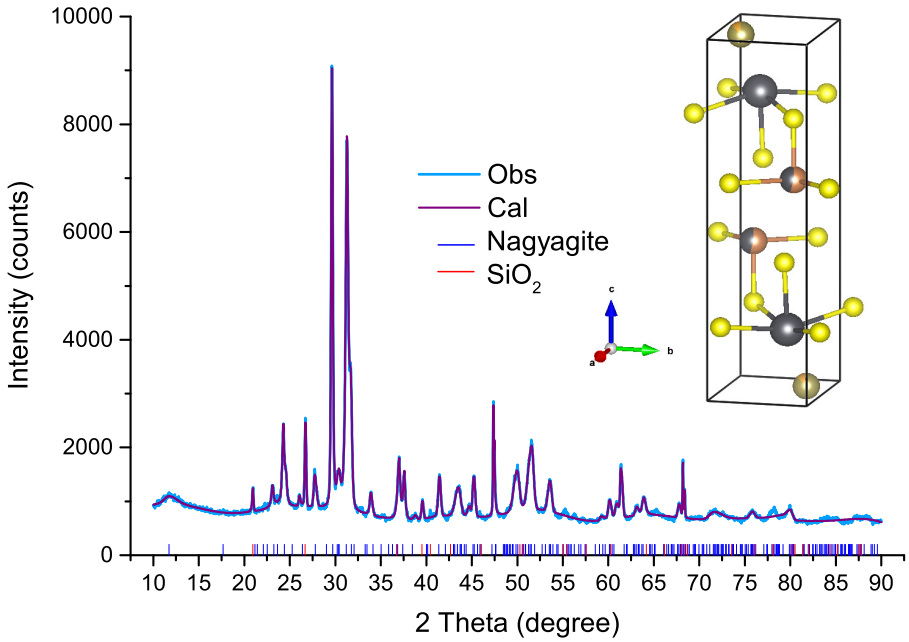

Figure 5.2: The X-ray diffraction pattern of natural nayagite. Red peaks are quartz(SiO_2) from the mineral samples.

white part of the picture. For the magnetic properties and transport measurements, I removed the quartz from the sample as much as possible. To study the structure, as well as the chemical composition of the natural samples, X-ray diffraction data of several pieces of nagyagite crystals with the quartz as well were collected. The refinement was done with the average structure proposed by Herta Effenberger. As shown in Figure 5.2, we are not able to distinguish any impurity peaks except for quartz. Even though we cannot exclude the possibility of having other impurity phases, the main phases of our nagyagite samples are of 95% nagyagite and 5% quartz determined by reference intensity ratio (RIR) method.

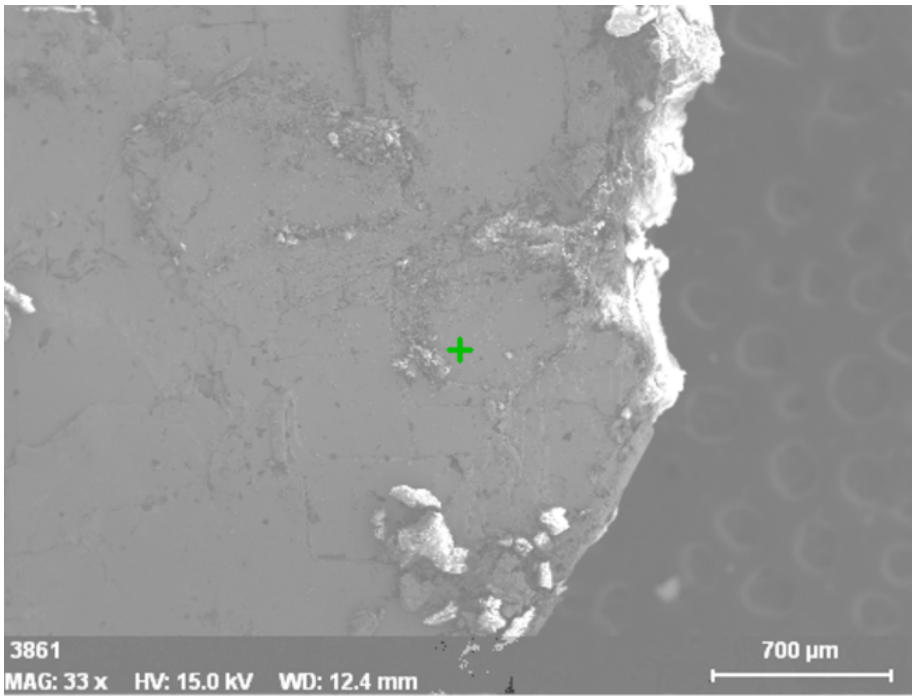

Figure 5.3: TEM image of a piece of natural nagyagite sample, the white parts are quartz; corresponding EDS results are shown in TABLE 1. I didn't see any impurities from the surface, and the composition of elements is consistent with the chemical formula.

	Au	Te	Pb	Sb	S	Au:Te
Sample a	6.61%	13.41%	31.84%	7.33%	40.28%	1:2.03
Sample b	6.71%	13.89%	32.75%	7.52%	39.13%	1:2.07
Sample c	6.60%	14.18%	32.26%	7.12%	39.84%	1:2.15
Sample d	4.68%	15.97%	32.88%	7.54%	41.03%	1:3.41
Our sample	5.83%	16.65%	40.17%	9.02%	28.33%	1:2.83

Table 5.1: The atom composition of nagyagite samples in different papers. Sample a: Herta Effenberger (1999) [1], samples from Nagyag, Romania, collection of the Institute of Mineralogy and Crystallography, University of Vienna. Sample b: Paar and Chen (1982) [2], samples from Schellgaden, Austria. Sample c: Stanley et al. (1994) [3], samples from Nagyag, Romania. Sample d: Herta Effenberger (1999) [1], synthetic nagyagite, standard deviation in parentheses from 18 analysis. Our sample: samples from Nagyag, Romania, collections of Department of Mineral Sciences, Smithsonian Institution.

5.3.2 Resistivity

Resistivity temperature relation data were collected from 4 different pieces of samples. Even though the normalized values are a little bit different, the shapes of the plots are very similar. As shown in Figure 5.4, the resistivity of two different samples, the resistivity of both samples first increase with temperature decreasing and has a broad peak at around 220 K. Then the resistivity value decrease with temperature decreasing. At the lower temperature at around 50 K, both samples

have a metal-insulator transition. The resistivity data have great similarity with the data of $[Pb_2BiS_3][AuTe_2]$ samples reported by Fang [54, 55]. Resistance magnetic field dependence was also taken under different temperatures. For the low field part, we also see weak anti-localization phenomenon in sample 2 down to 2 K, while the signal is not large enough to be figured out in sample 1. Also, the WAL disappears at around 5 K in sample 2. The discrepancy of the low-temperature resistivity values may come from the anisotropic property of nagyagite since all the experiments are general measurements without structure characterization, there may exist some angular dependence in the *ab* plane.

For higher field, the magnetoresistance data were collected at 2 K, 30 K, 50 K and 300 K. The temperatures were selected according to the resistivity curve. Figure 5.6 shows the raw magnetoresistance, both samples have very obvious negative magneto resistance at low temperature. To make a comparison with $[Pb_2BiS_3][AuTe_2]$, a HLN model with strong SOC were used to fit the low field data at 2 K as shown in Eq 5.1, where α equals 0.5 for weak anti-localization, $B_\Phi = \frac{\hbar}{4el_\phi^2}$ and l_ϕ is the electron coherence length. The data doesn't look so symmetric due to the Hall components. The coherence length is about 1.37 nm.

$$\Delta\sigma(B) = \alpha\frac{e^2}{2\pi^2\hbar}(\ln(\frac{B_\Phi}{B}) - \Psi(\frac{1}{2} + \frac{B_\Phi}{B})) \tag{5.1}$$

5.3.3 Magnetic susceptibility

Both ZFC and FC susceptibility temperature dependence of natural nagyagite samples were taken in a constant field of 1000 Oe from 300 K to 2 K. As shown

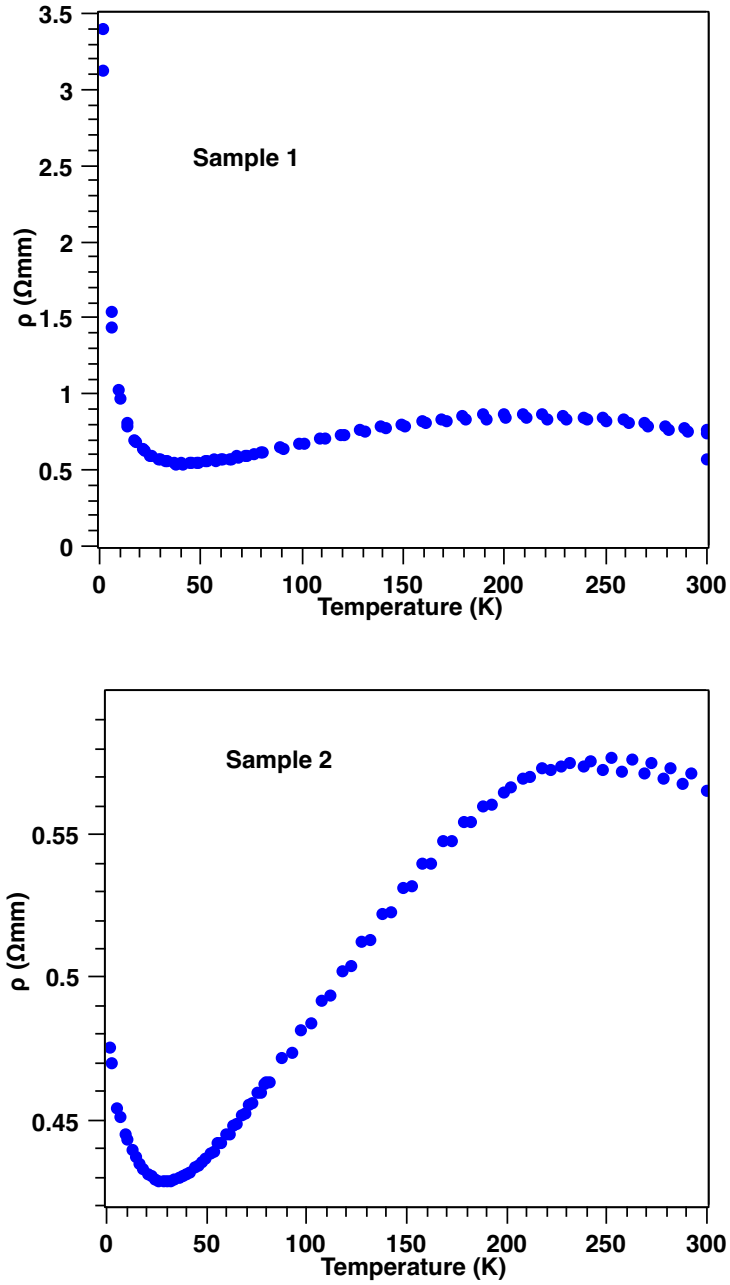

Figure 5.4: Resistivity of natural nagyagite.

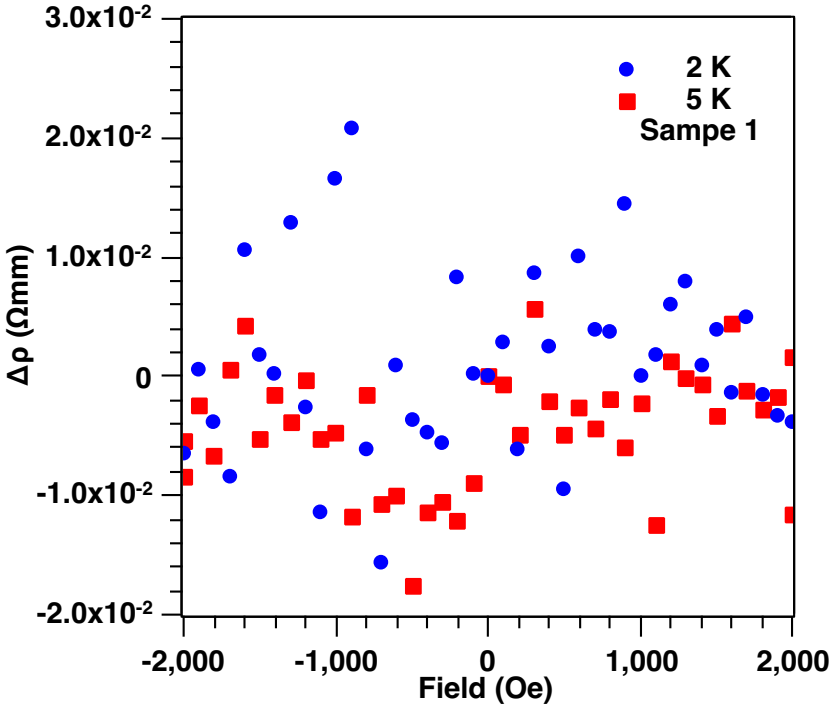

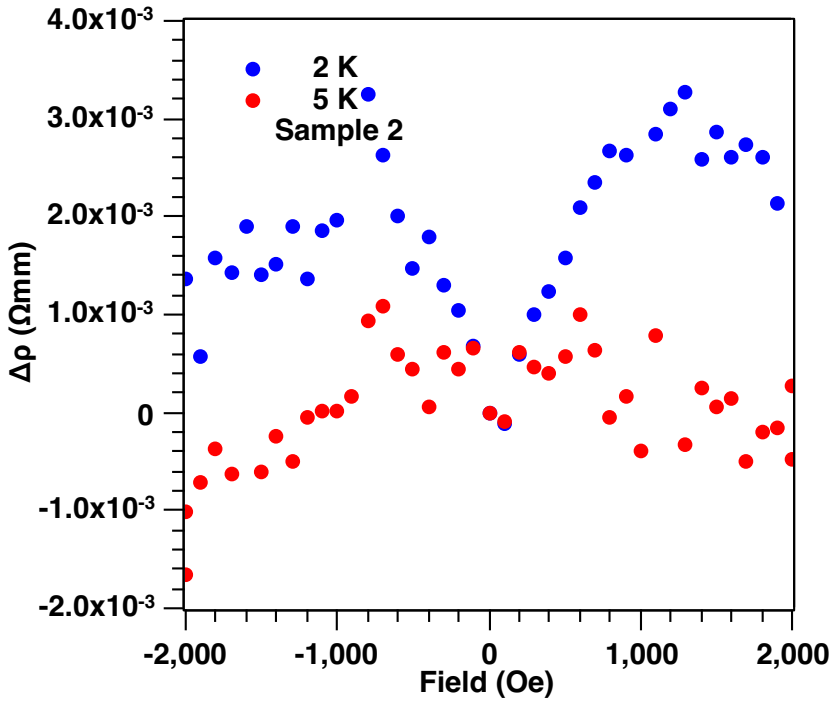

Figure 5.5: ρ(H) - ρ(0) at 2 K and 5 K of 2 of sample 1 and sample 2.

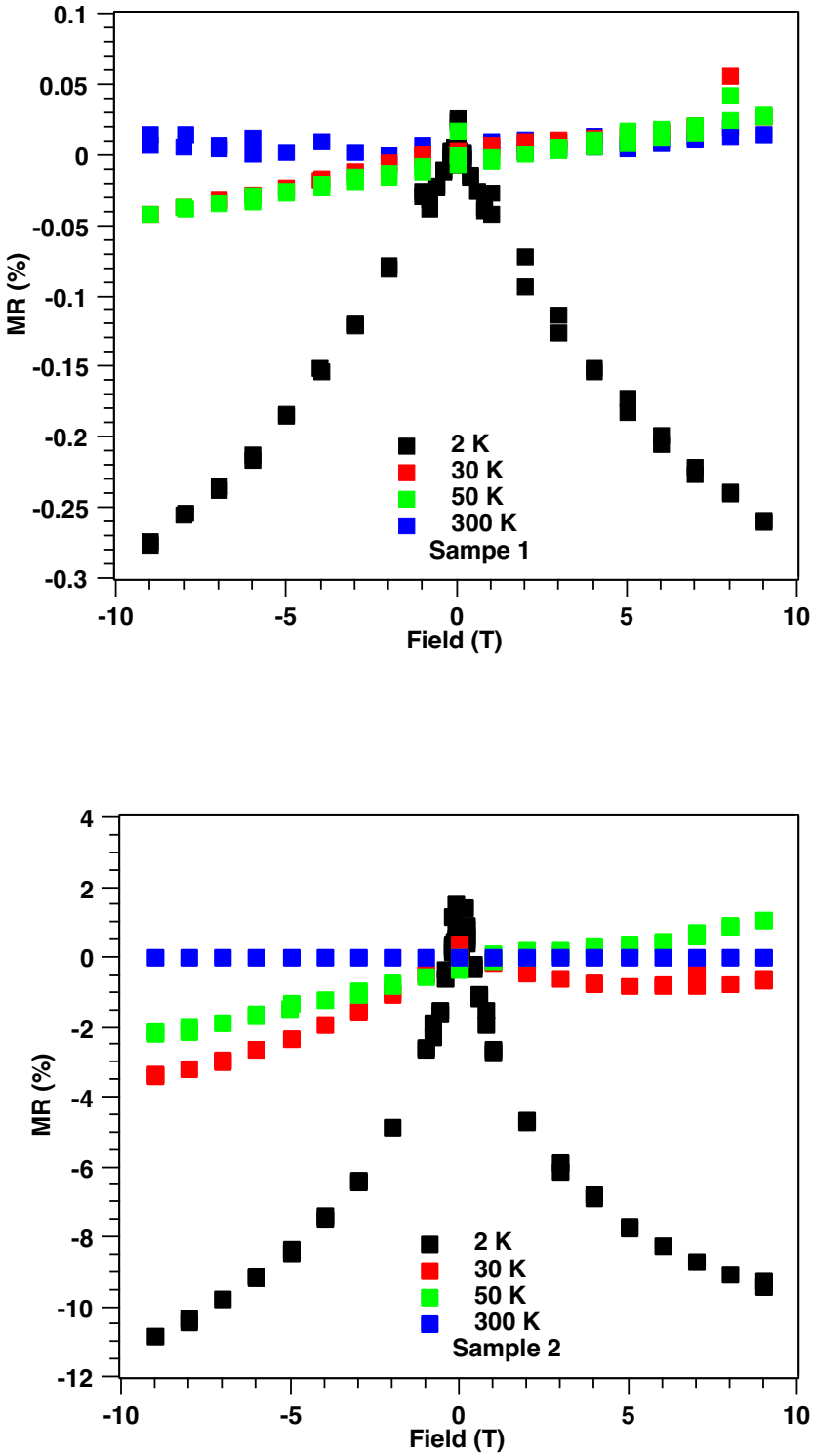

Figure 5.6: Magnetoresistance of nagyagite at 2 K, 30 K, 50 K, 300 K.

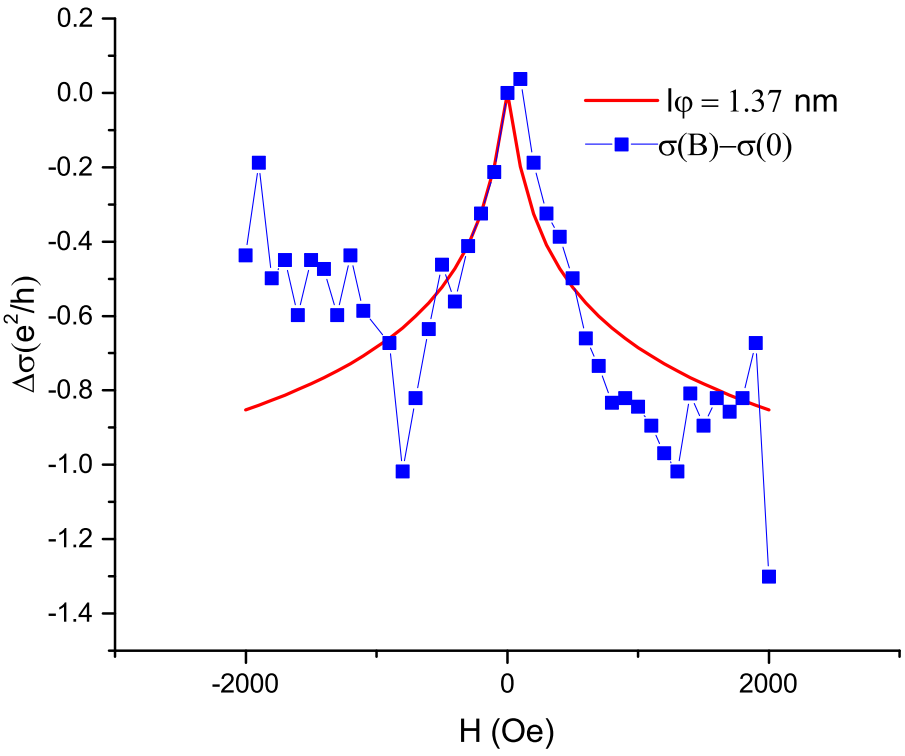

Figure 5.7: The change of normalized conductance fitted with HLN model.

in Figure 5.7, a sudden increase at around 30 K in FC and ZFC data indicates a ferromagnetic order. The irreversibility between FC and ZFC suggests spin-glass (SG) state. The susceptibility above the transition temperature can be perfectly fitted with Curie Weiss law, $\chi = \frac{C}{T-\Theta}$. As shown in the inset of Figure 5.7, we have a negative Curie temperature of Θ = -54.4 K and an effective magnetic moment of 0.76 μ_B. The Curie temperature of a ferromagnetic material is expected to be positive. The negative Curie temperature suggests antiferromagnetic interactions in the material, which may due to some ferrimagnetic order. The magnetic susceptibility measurements were repeated with three different samples, and all the samples had the ferromagnetic order at the same transition temperature. The magnetic hysteresis data at 4 K is shown in Figure 5.9. Since there are no magnetic atoms in the

system, one possible reason is that there exist some magnetic atoms or impurities in the mineral and cannot be detected with EDS and XRD experiments. In this case, these phenomena can still be regarded as the intrinsic properties of natural nagyagite sample. We may be able to construct the magnetic system by doping some magnetic elements in synthetic nagyagite. Another possible reason for the magnetic transition is probably due to the so-called d^0 ferromagnetism. The d^0 ferromagnetism is used to explain some of the ferromagnetic materials without magnetic atoms; the magnetism may come from some electron polarization. For example, pure gold is nonmagnetic, while gold nanoparticles display a magnetic moment [56]. But the theory itself is still under debating. Synthesizing some lab-made nagyagite single crystals is necessary. Also, first principle calculation may reveal the reason for the magnetism.

5.3.4 M-H curve

To understand the ferromagnetic interaction, I also did the magnetic isotherm measurement. The M-H curve from 4 K to 52 K is presented in Figure 5.10. To understand the nature of the magnetic phase transitions, I have transformed the M-H data into Arrott plots as shown in Figure 5.11. Banerjee has given an experimental criterion, which allows us to determine whether a magnetic transition is a first or second order. It consists in observing the slope of the isotherms plots M^2 versus H/M. Applying a conventional approach, the straight line was constructed simply by extrapolating the high magnetization parts of the curves for each studied

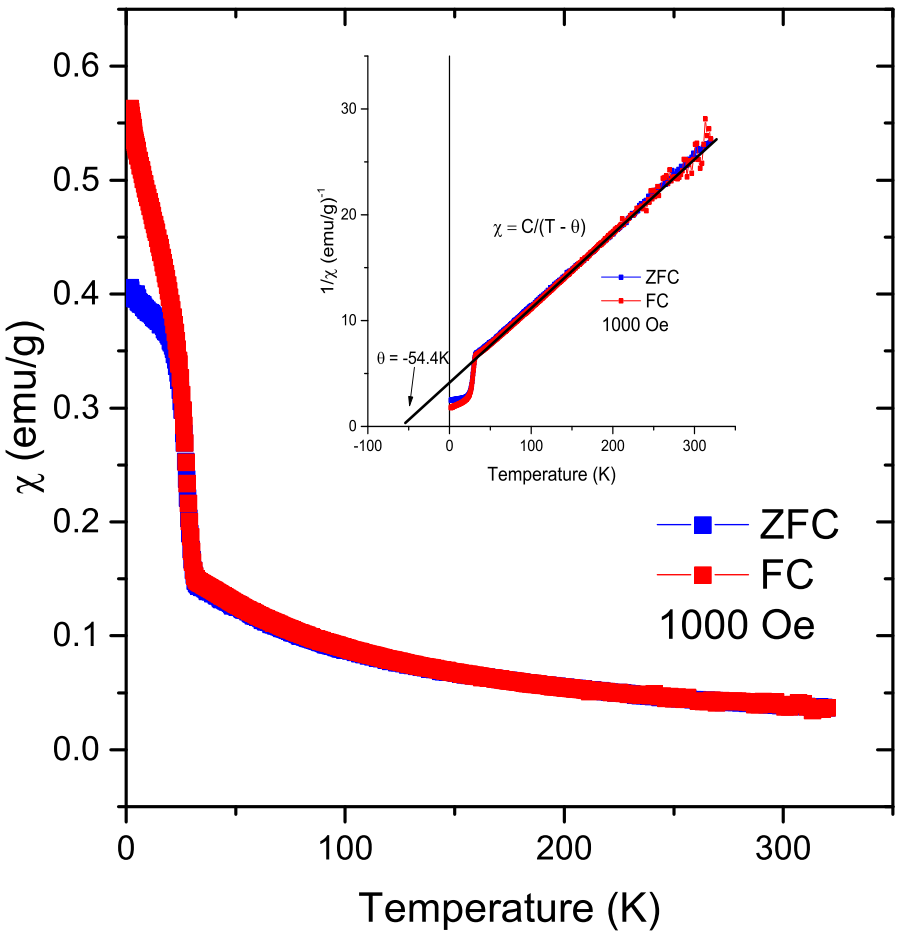

Figure 5.8: Magnetic susceptibility of natural nagyagire. The inset shows the Curie-Weiss fitting. Although the samples have a very clear ferromagnetic transition, the Curie Weiss fit give a negative Curie temperature which correspond a AFM interaction.

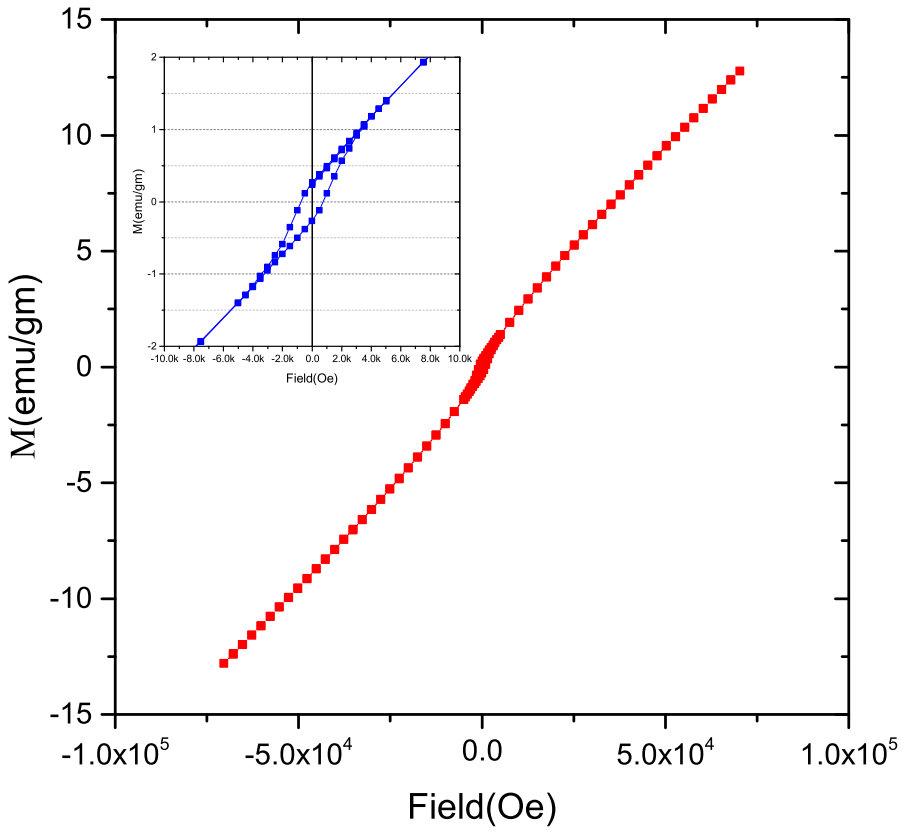

Figure 5.9: Magnetic hysterisis of natural nagyagite at 4 K. This prove the ferromagnetic order in natural nagyagite samples.

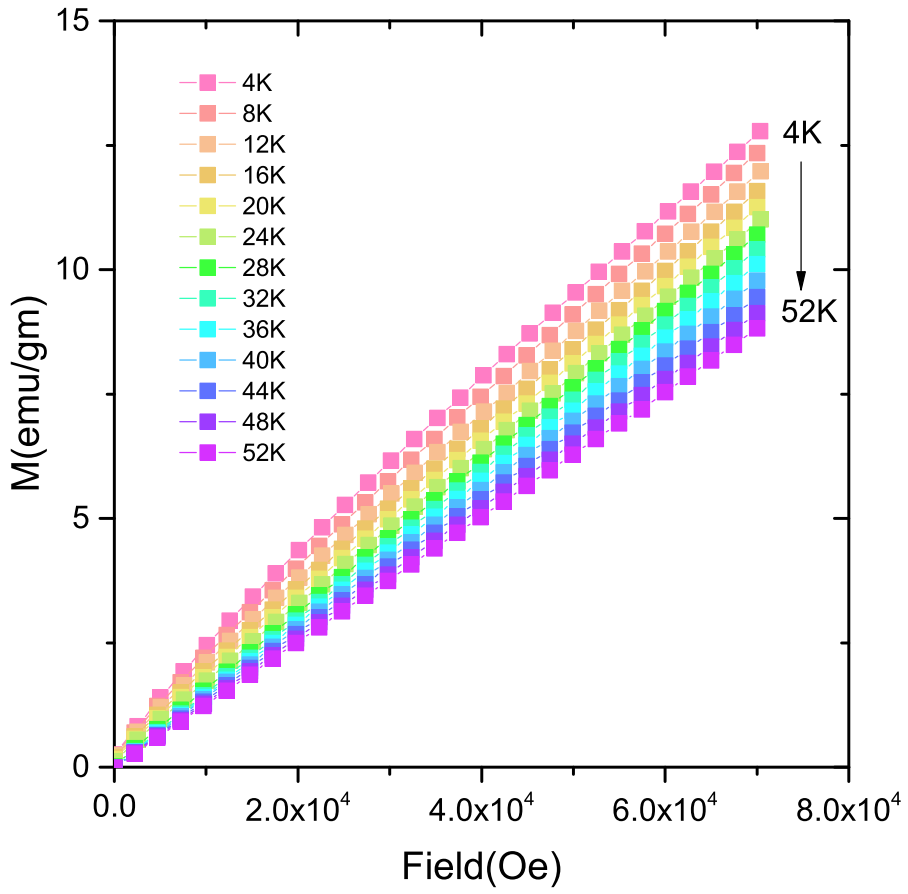

Figure 5.10: M(H) curves of natural nagyagite samples from 4 K to 52 K.

temperature. The negative slope of the Arrott plot indicates a first-order transition, while the positive slope implies a second order transition [57]. From Figure 5.11, the Arrott plots have positive slopes for both below and above T_c, indicating that the transition is second order.

The magnetic entropy change can be evaluated using the Maxwell equation,

$$\Delta S_M = \int_0^H \left(\frac{\partial S}{\partial M}\right)_T dH = \int_0^H \left(\frac{\partial M}{\partial T}\right)_H dH \tag{5.2}$$

In our magnetization measurement, I calculated the magnetic entropy change

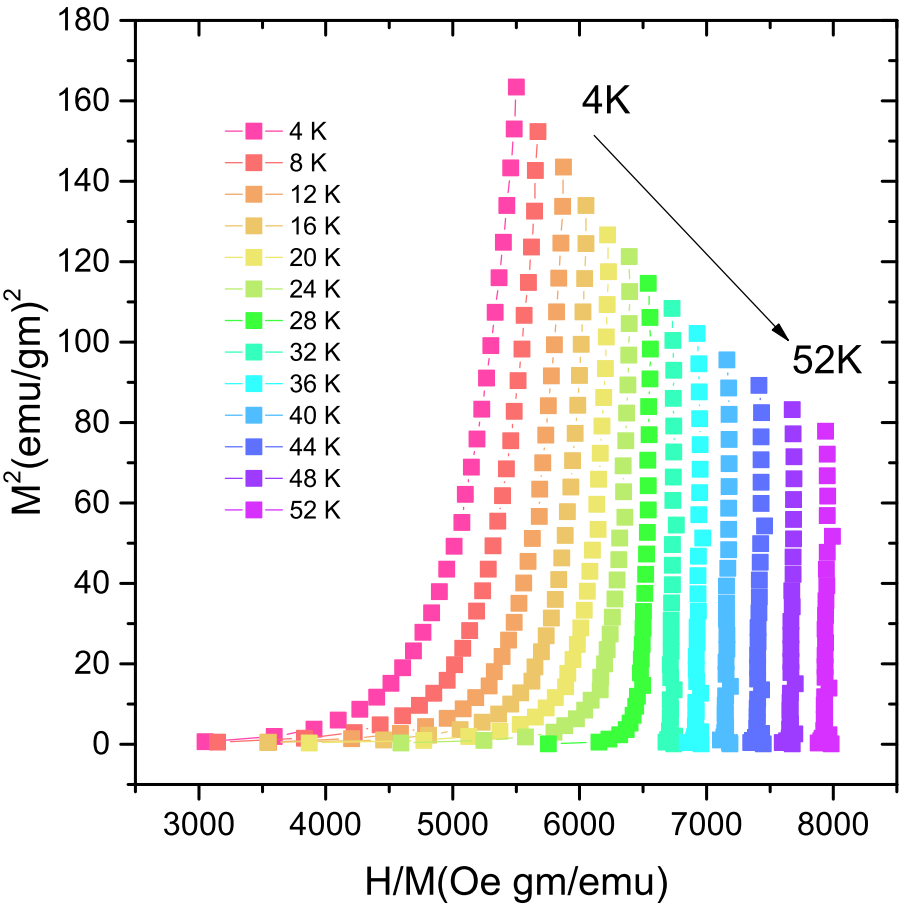

Figure 5.11: Arrott plots of natural nagyagite.

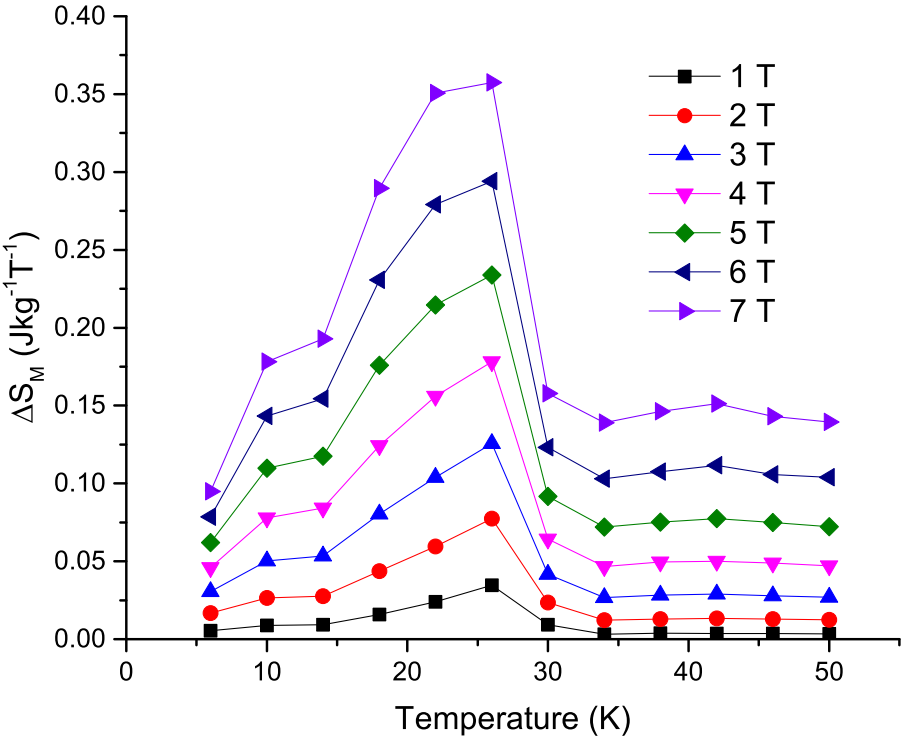

Figure 5.12: Magnetic entropy change of natural nagyagite. It shows a maximum at the transition temperature.

with approximation,

$$\Delta S_M \left(\frac{T_i + T_{i+1}}{2} \right) = \sum \frac{M_{i+1} - M_i}{T_{i+1} - T_i} \Delta H_i \tag{5.3}$$

As shown in Figure 5.12, the magnetic entropy change are presented with temperature from 1T to 7T. The magnetic entropy change has the maximum right around the transition temperature around 25K.

5.4 Conclusion

I report the magnetic and transport properties of naturally occurring mineral nagyagite. The slope of resistivity temperature relation changes several times

from 2 K to 300 K. Natural nagyagite samples have negative magnetoresistance at low temperature, and some of the samples show weak anti-localization phenomena with a relatively large coherence length. The 2D layered structure associated with these phenomena makes nagyagite a candidate for 2D heterostructures with a strong spin-orbit coupling which may be related to topological quantum materials. Surprisingly, a ferromagnetic transition was discovered in natural nagyagite samples. It may come from impurities that have not been detected, or it might be derived from the d^0 ferromagnetism. Either reason makes nagyagite an interesting system. Synthetic nagyagite samples and first principle calculation should be conducted in the future for further investigation. Also, another similar material museumite (Pb_2(Pb, Sb)$_2S_8$[Te, Au]$_2$) which also has the AuTe layers can be regarded as another material in this family.

Chapter 6: Maucherite ($Ni_{11}As_8$): crystalline size-dependent magnetic transition in natural minerals.

In this section, we will discuss the magnetic transition in natural mineral maucherite ($Ni_{11}As_8$) as well as the physical properties of synthetic maucherite. The comparison gives a possible explanation for the discrepancies between the natural and synthetic samples. This may provide us with some inspiration about the difference between natural compound, and the lab made ones, even if a material has already been well studied, the same naturally occurring compound is still worthy of investigation. Xiuquan and I did the grinding research together, and he helped me do the TEM measurement for the powder samples.

6.1 Introduction

Since the discovery of superconductivity in iron-based superconductor $LaFeAsO_{1-x}F_x$ [58, 59], a lot of experiments have been devoted for searching new iron-based superconductors. This family of new superconductors show competition between superconductivity and magnetization with chemical doping or applying pressure. The quasi-2D Fe-As layers in the *ab*-plane also brought a lot of attention in investigating transition metal arsenide binaries, which also have the similar tetragonal structure

to those Fe-based superconductors [13]. Also, transition metal arsenide binaries are a very significant family of magnetic materials with different special magnetic properties arising from the 3d, 4d, 5d electrons [60]. There is a small number of investigation about transition metal arsenide materials, most of the transition metal arsenide binaries show very interesting physical and magnetic properties. An anomalous spin density wave state was reported in FeAs [61]. A transition related to the double-spiral h_c-type antiferromagnetism and superconductivity was reported in Cass [62, 63]. MnAs has a ferromagnetic transition accompanied by a structural transition [64]. A metal-insulator transition was reported in RuAs samples [65]. NbAs were predicted as a potential Weyl semi-metal [66]. However, there were few low-temperature experiments about transition metal arsenide binaries due to the difficulty of growth, and many of the reported transitions were not well studied. Natural nickel arsenide binary minerals have a wide distribution in nature ore. For instance, nickeline (NiAs), rammelsbergite ($NiAs_2$), and pararammelsbergite ($NiAs_2$) were reported as paramagnetic materials [67]. Another natural Nickel arsenide binary maucherite ($Ni_{11}As_8$) was first discovered in 1913. Nanosheets of $Ni_{11}As_8$ were synthesized via hydrothermal redox route [68]. The nanosheet samples show weak ferromagnetism at room temperature. The physical properties of bulk maucherite have still not been well investigated. I studied the magnetic properties of natural maucherite samples. The transport data of natural maucherite samples including resistivity and heat capacity data will also be presented in this chapter. Synthetic poly-crystals of $Ni_{11}As_8$ were also synthesized. I compared the susceptibility of both synthetic, naturally occurring and nanosheet samples. Surprisingly,

the natural samples show different susceptibility temperature dependence from the synthetic samples. Also, the magnetic moment of nanosheet samples is ten times larger than the bulk samples. These unusual magnetic properties are probably due to the sample size dependence of the ferromagnetism. $Ni_{11}As_8$ can be regarded as a good system to study the finite-size scaling properties of ferromagnetism.

6.2 Experiments

Natural maucherite poly-crystal samples were taken from Department of Mineral Science, Smithsonian Institute. Synthetic polycrystalline powder samples were made by melting of high purity Ni and As powder. Powder x-ray diffraction data were collected with Rigaku MiniFlex X-ray diffractometer at room temperature. Temperature dependence of susceptibility from 300K to 2K and magnetic isotherm measurements at various temperatures were taken with Quantum Design Magnetic Property Measurement System (MPMS). The resistivity temperature dependence was measured with the 4-wires method in Quantum Design Physical Property Measurement System (PPMS). The heat capacity was measured from 150K to 2K with PPMS as well. Neutron diffraction experiments were conducted with High-Resolution Powder Diffractometer - BT1 at NIST Center for Neutron Research.

6.3 Results and Disccusion

6.3.1 Crystals and X-ray diffraction

Both natural and synthetic maucherite samples have gray metallic luster. Our synthetic samples are very fragile compared with the natural samples. We can break the synthetic samples into powder even by touching them with a tweezer, while we have to grind the natural samples in mortar to make them into powder. Powder X-ray diffraction (XRD) data for both samples were collected with Cu $K\alpha$ radiation, $\lambda = 1.5418$ Å, with 2θ ranging from 20°to 80°. Rietveld refinement of both samples is presented in Figure 6.2. Both samples have some nickeline (NiAs) impurities, but the maucherite phases are well consistent with the previously reported structure of natural $Ni_{11}As_8$ samples. Maucherite has a complex tetragonal unit cell with $P\bar{4}_12_12$ space group. The lattice constants are $a = 6.872$ Å, $b = 6.872$ Å, $c = 21.821$ Å [69], as shown in Figure 6.1. The unit cell is composed of ordered-disordered (OD) layers of one kind; the unit layers display stack orientation along the c axis [70]. Table 1 presents the weight ratio of the main phase and impurity phase calculated with reference intensity ratio (RIR) method and the lattice constants of best refinement. Since NiAs is paramagnetic material, it didnt affect our magnetic measurements very much.

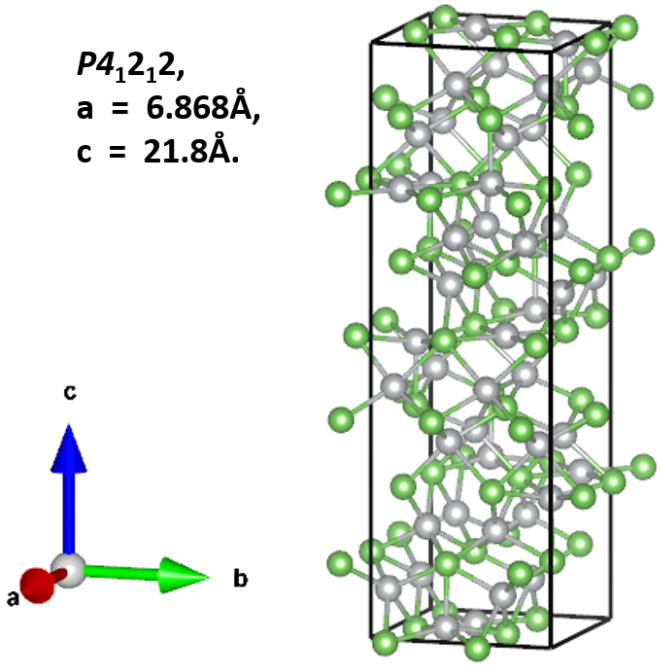

Figure 6.1: The unit cell of maucherite ($Ni_{11}As_8$). The green atoms are Ni atoms, and white ones are As atoms. The structure can be regarded as four layers, and each layer is of the same structure and rotates 90 degrees compared with the lower layer.

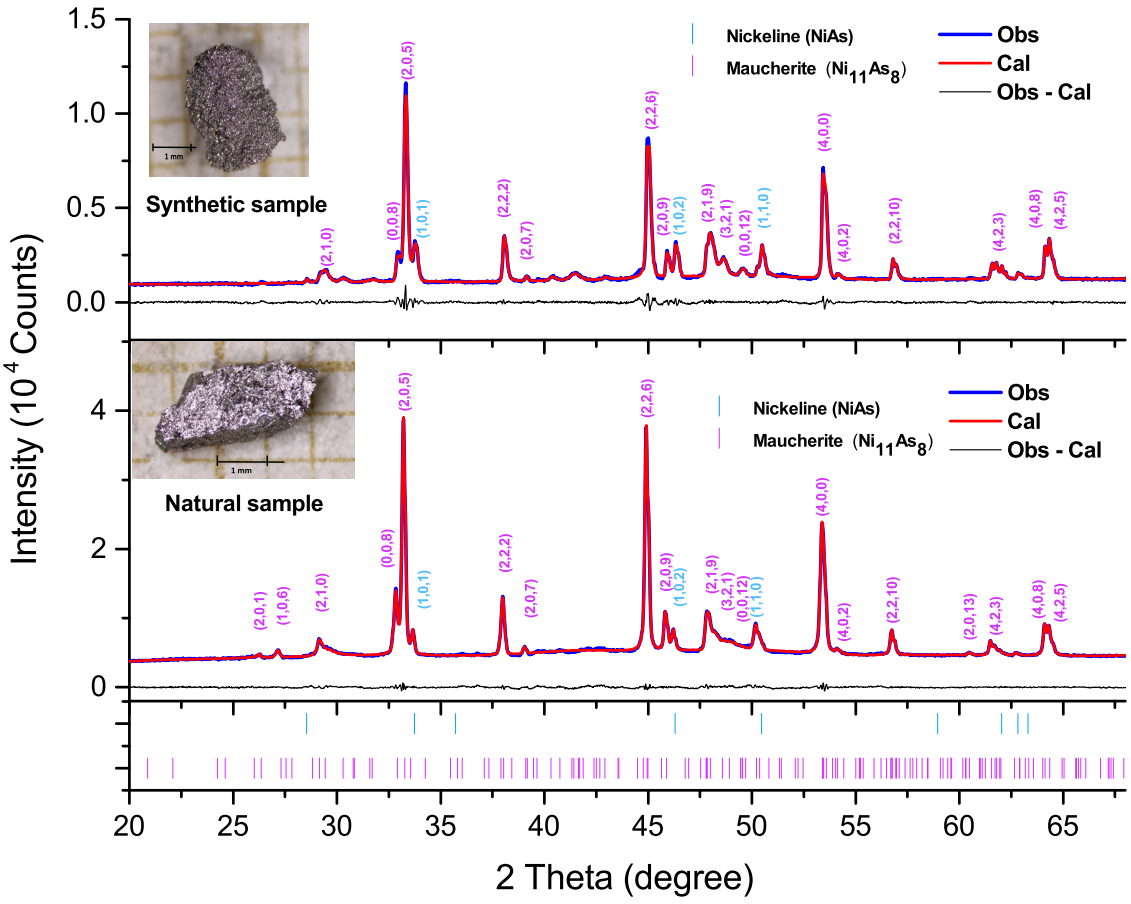

Figure 6.2: The X-ray diffraction patterns of natural and synthetic maucherite samples. The blue lines are observed data, and the red lines are calculated data. The photos of both samples are displayed in the figure. The synthetic sample is very fragile compared with the natural sample.

	Natural Sample	Synthetic Sample
$Ni_{11}As_8$ (%)	96(5)	90(2)
NiAs (%)	4.1(2)	9.5(2)
a (Å)	6.86(2)	6.86(4)
b (Å)	6.86(2)	6.86(4)
c (Å)	21.81(5)	21.77(3)

Table 6.1: A comparision of the natural occurring samples and synthetic samples. Both samples have some Nickeline (NiAs) impurities. The first two rows of the table show the percentage of $Ni_{11}As_8$ and NiAs in weight. The last three rows are the lattice parameters with the smallest residues after refinement.

6.3.2 Magnetic susceptibility

Both zero-field-cooled (ZFC) and field-cooled (FC) susceptibility temperature dependence of natural samples were taken in constant fields of 100 Oe and 1000 Oe from 300 K to 2 K. I also measured the ZFC and FC susceptibility temperature relation of synthetic sample powder from 300 K to 10 K in 1000 Oe field. As shown in Figure 6.3, in natural mineral samples, a sudden enhancement at around 20 K in FC and ZFC data suggests a formation of ferromagnetic order. The irreversibility between FC and ZFC indicates spin-glass (SG) state. With field increasing, the irreversibility becomes smaller, indicating the frozen SG state is gradually destroyed under larger magnetic fields. These coincide well with other SG systems. The susceptibility above the transition temperature can be fitted with modified Curie Weiss

law, $\chi = \chi_0 + \frac{C}{T-\Theta}$. As shown in the inset, we have a negative Curie temperature of Θ = -40.9 K and a very small effective magnetic moment of 0.019 μ_B. The Curie temperature of a ferromagnetic material is expected to be positive. The negative Curie temperature suggests antiferromagnetic interactions in the material, which perhaps indicates some ferrimagnetic order. While for the synthetic samples, the susceptibility increases with temperature decreasing without any obvious transition. The susceptibility data of both samples are very close at low temperature.

6.3.3 Resistivity

The resistivity data were collected from 300 K to 2 K at 0 T and 7 T. As shown in Figure 6.4, the natural maucherite sample show typical metallic behavior. The resistivity decreases as temperature decreasing with a $\rho = \rho_0 + AT^2$ relation, suggesting a Fermi liquid behavior at low temperature. ρ_0 is approximately 4.22×10^{-6} Ω m and A equals 1.15×10^{-10} Ω mK^{-1}. The residual resistivity ratio (RRR), defined as ρ(300K)/ρ(2K), equals 6.7. I didn't see any obvious abnormal around the transition temperature. The magnetic field doesn't affect the resistivity very much.

6.3.4 Heat capacity

Heat capacity data were taken from 150K to 2K. The results are displayed in Figure 6.5. The heat capacity data is consistent with the Debye's model. There is no obvious abnormal at the transition temperature, but a very small cusp can be found at around 30 K.

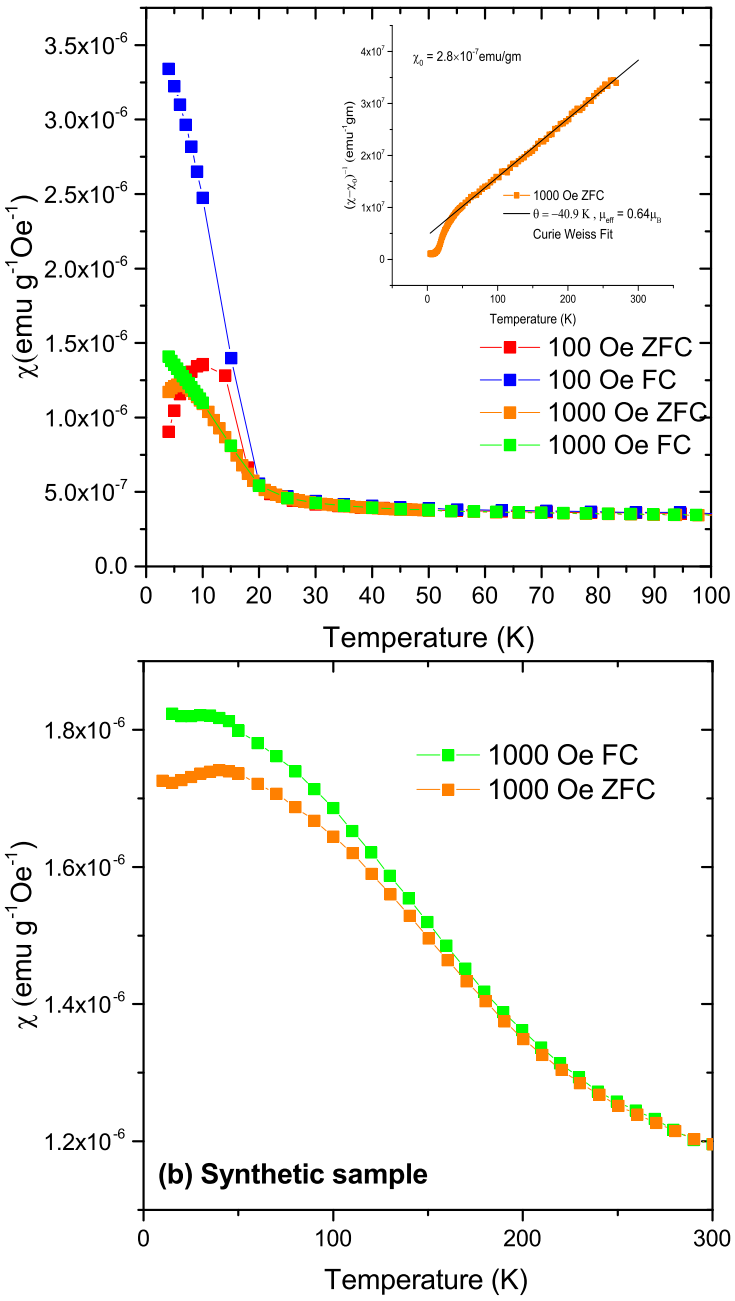

Figure 6.3: (a) The ZFC and FC susceptibility temperature relation of natural maucherite samples at 100 Oe and 1000 Oe from 2 K to 100 K. (b)The ZFC and FC data of synthetic samples at 1000 Oe from 300K to 10 K.

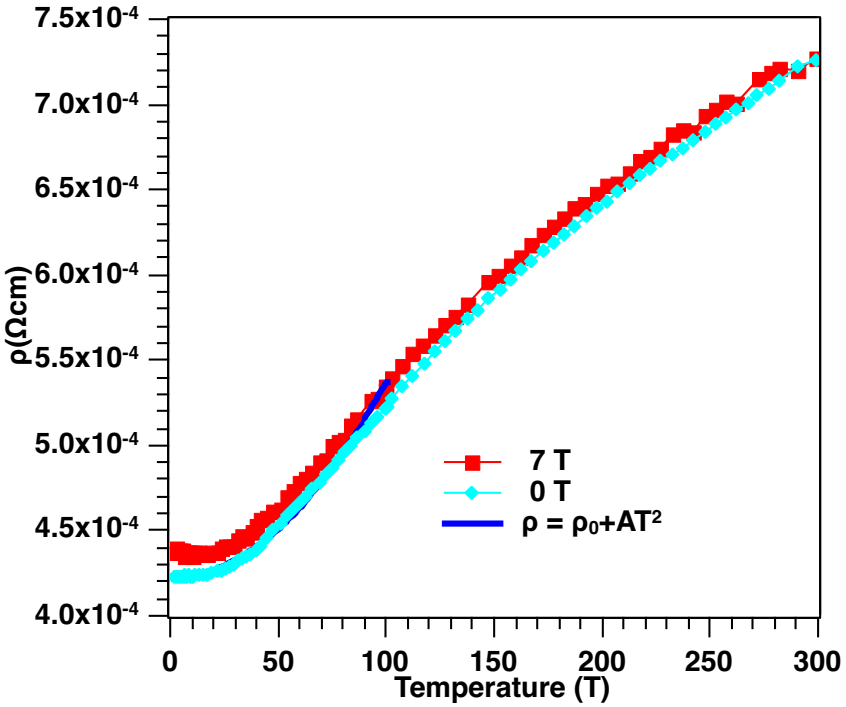

Figure 6.4: Reisitivity of natural maucherite samples from 2 K to 300 K at 0 T and 7 T. The resistivity follows the Fermi liquid theory and doesn't change much with field.

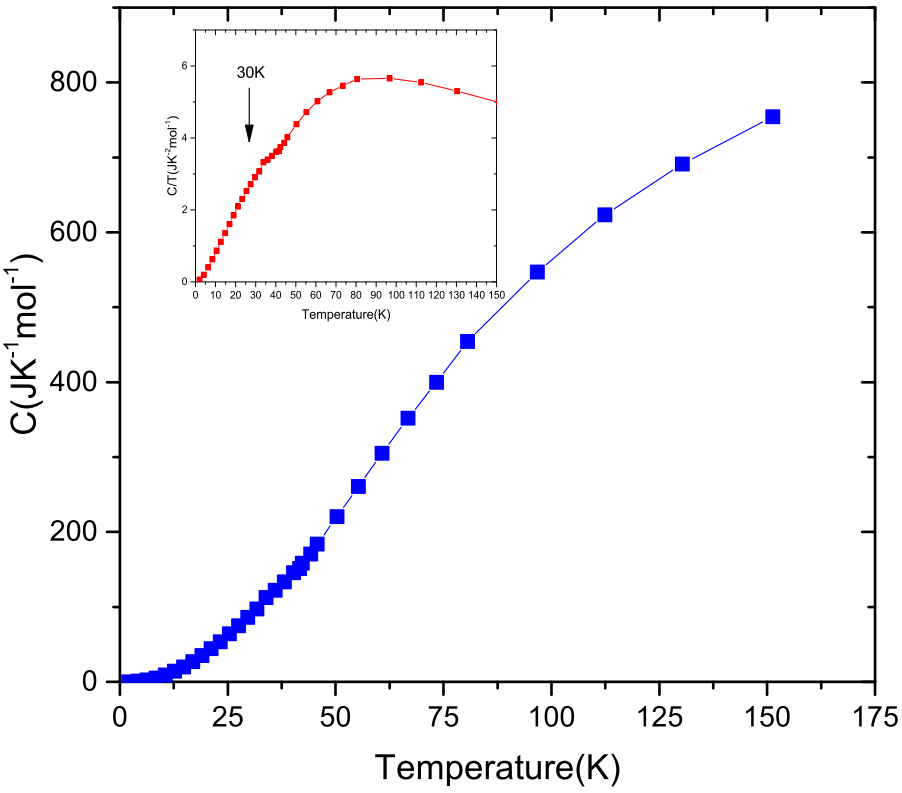

Figure 6.5: Heat capacity of natural maucherite from 2K to 150K, the inset shows the plot of C/T v.s. T. A subtle abnormal can be found at around 30K

6.3.5 Magnetic isotherm

For better understanding the magnetic transition, I also did the magnetic isotherm measurement. The susceptibility temperature dependence of bulk and powder natural samples, as well as the M-H curves of natural bulk maucherite at 4K, natural powder at 300 K, synthetic powder sample at 10 K and 300 K, nanosheets at 283 K [68] are plotted in Figure. 6.6. As we can see, the magnetic moment was enhanced after grinding for natural samples. The M-H curves of both single crystalline nanosheets and synthetic and natural maucherite powder have room temperature ferromagnetic behavior, while the natural bulk samples only show ferromagnetic M-H curve below 20 K. The magnetic moments of both natural and synthetic bulk compounds are ten times smaller than the ferromagnetic moment of the $Ni_{11}As_8$ nanosheet reported by Wei *et al.* [68]. The difference in magnetic order and transition temperatures between nanosheets, synthetic powder samples, and natural bulk samples is probably due to the typical size dependence of the magnetization of some ferromagnetic, ferromagnetic and multiferroic materials. A field dependence shift in Curie temperature up to 93 K was discovered in nanoscale $MnFe_2O_4$ particles [71–73]. The Curie temperature increased as the size of the particles decreases. Such phenomena associated with a size-depended susceptibility value were also reported in some other transition metal compound [74–76]. The size-dependence of the transition temperature and magnetization are often modeled by finite-size scaling model [77]. In a second order transition case, the shift of Curie temperature is described as,

$$T_c(L_\infty) - T_c(L) = aL^{-\frac{1}{v}} \tag{6.1}$$

We are not able to give a quantitative analysis of our results based on the finite-size scaling model, but considering the fragile property of the synthetic samples, the transition temperature difference between natural and synthetic samples is probably due to their microstructures. Size dependence of the magnetic order is worthy of study.

To understand the nature of the magnetic phase transitions, I have transformed the M(H) data in Figure 6.8 into Arrott plots shown in Figure 6.8. Banerjee has given an experimental criterion [57], which allows the determination of the nature of the magnetic transition (first or second order). It consists in observing the slope of the isotherms plots M^2 versus H/M. Applying a regular approach, the straight line was constructed merely by extrapolating the high magnetization parts of the curves for each studied temperature. The negative slope of the Arrott plot indicates a first-order nature of the transition, while the positive slope implies a second-order transition. It is seen from Figure 6.9 that the Arrott plots have some positive slopes both above and below the transition temperature T_c, indicating that the exhibits some second-order property phase transition. In particular, the S-shaped nature of the Arrott plot near T_c denotes a negative order of the sign of the coefficient c2(T) in the Landau expansion of the magnetic free energy.

Tight binding calculation of bulk $Ni_{11}As_8$ was given in Wei's paper [68]. The density of state (DOS) implies the bulk $Ni_{11}As_8$ to be metallic and has a Fermi level

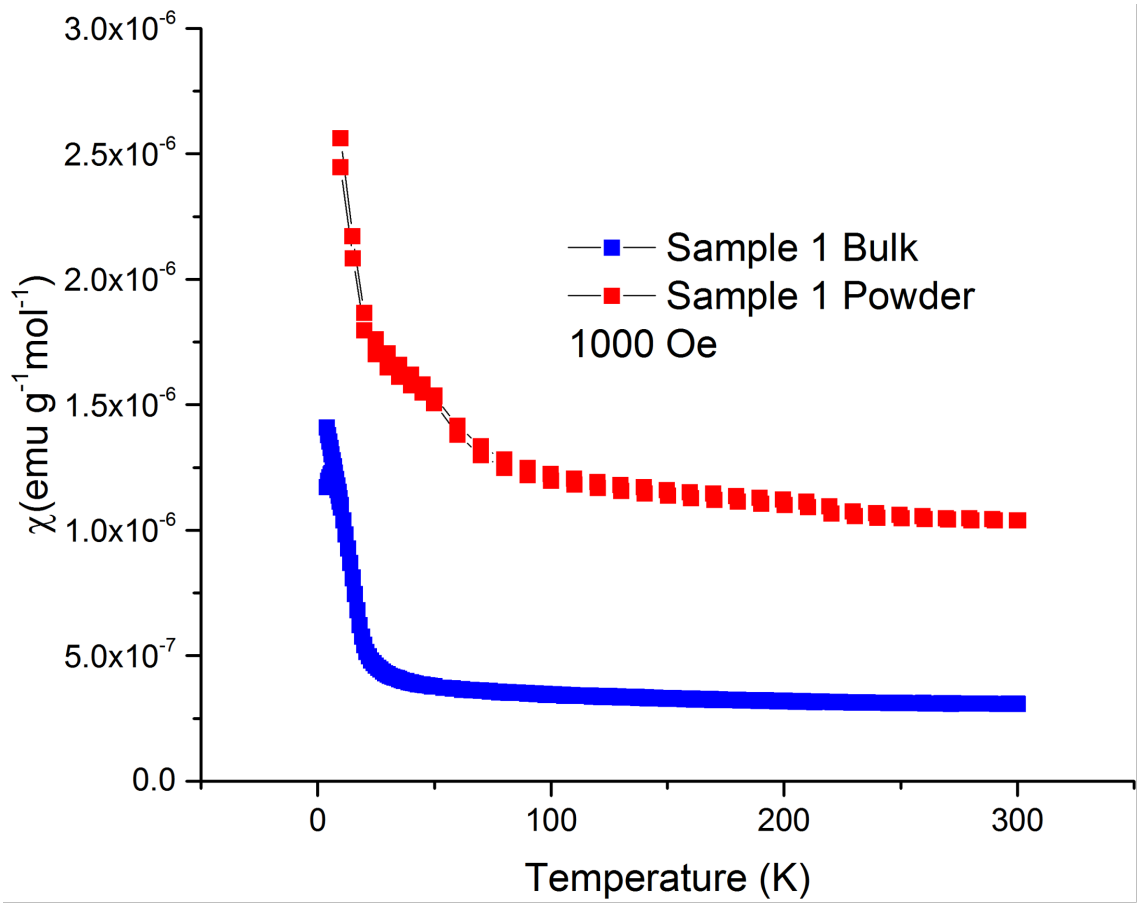

Figure 6.6: The susceptibility of natural maucherite bulk sample and powder sample. The experiment was repeated 3 times on different pieces of samples. The powder always has a larger magnetic signal than bulk samples.

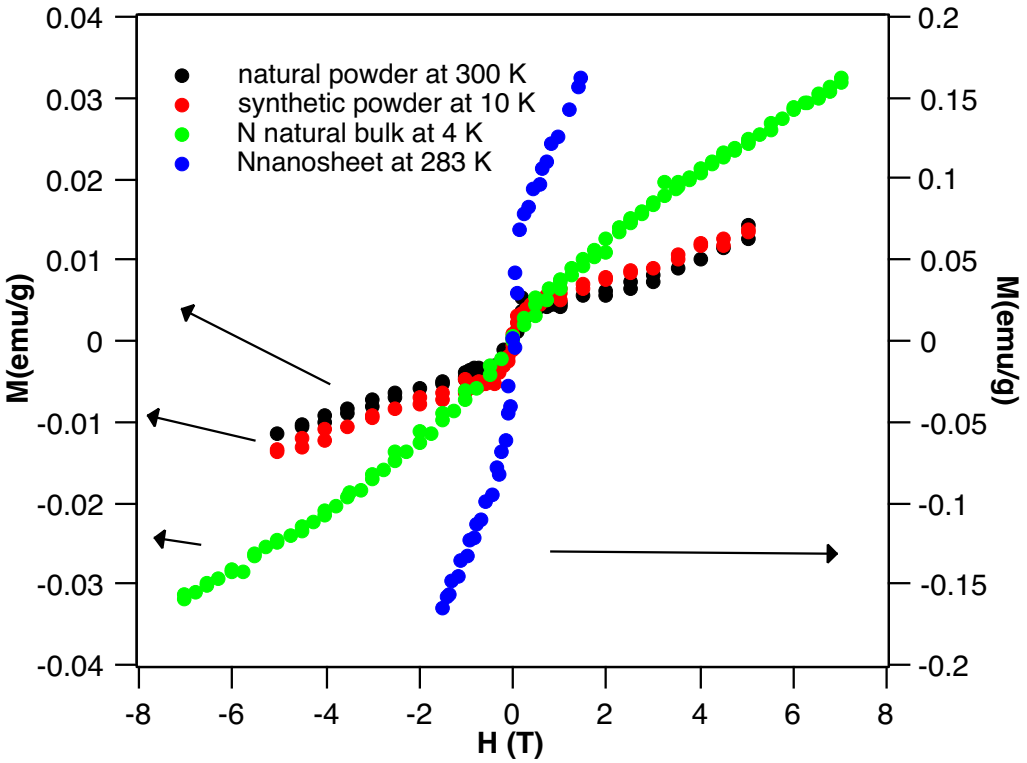

Figure 6.7: The M(H) curve of synthetic powder samples, natural bulk and powder samples, and nanosheet samples. The nanosheet samples has the largest magnetic signal.

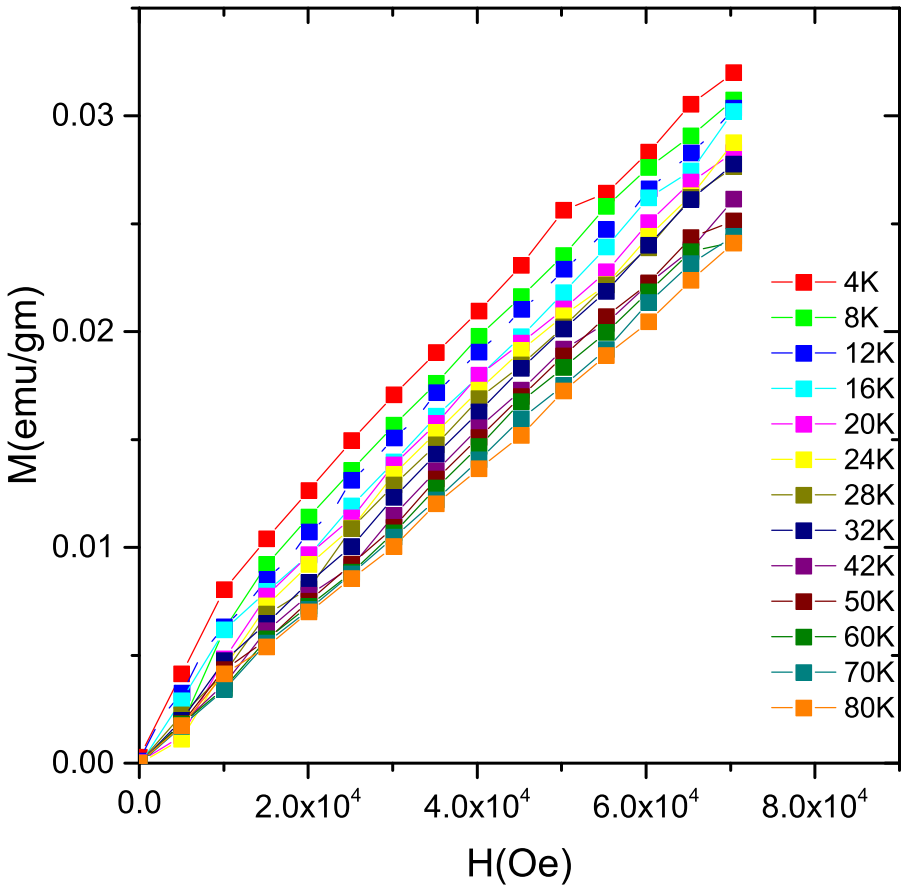

Figure 6.8: The magnetic isotherm of natural maucherite from 4K to 80K

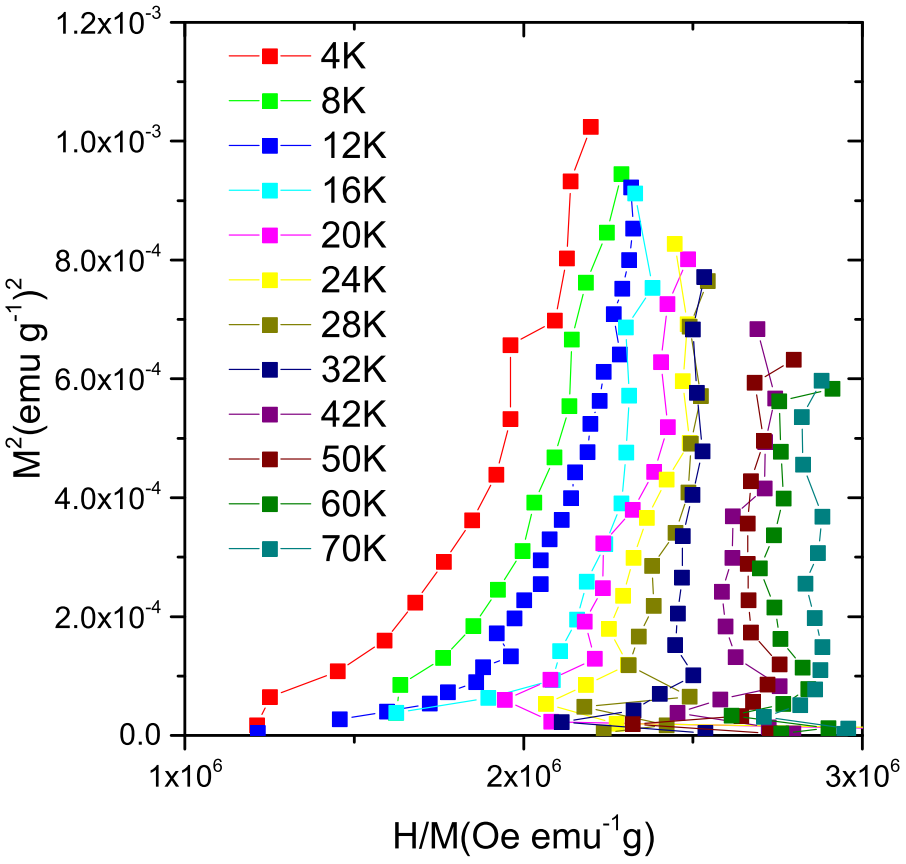

Figure 6.9: Arrott plots (M^2 with H/M) of maucherite sample. The positive slope above the transition temperature indicates a second order transition

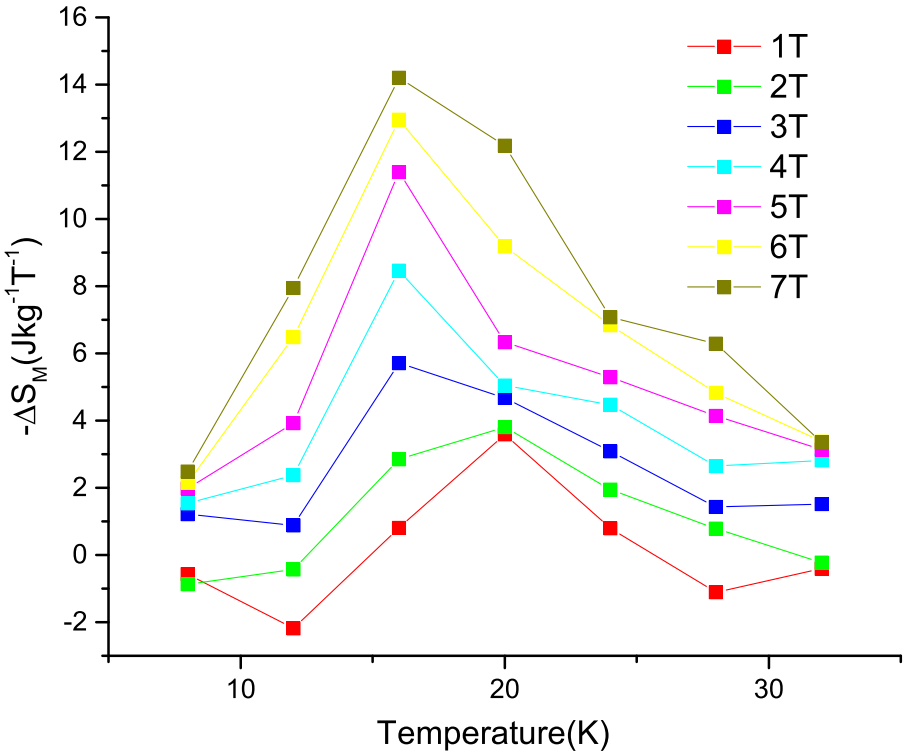

Figure 6.10: Magnetic entropy change(Δ_M) of maucherite samples from 8K to 32K, the data were calculated with the method mentioned in this chapter.

(FE) of -11.40 eV with small DOS right above EF. The previous band structure calculation is consistent with our transport data. Another remarkable character of the DOS is that there is a narrow band centered at -14.10 eV below the EF which can be viewed as the contribution of Ni atoms because the projected DOS of Ni atoms almost fills all of the total DOS narrow band. This energy of DOS maximum is slightly greater than the ionization potential of Ni 3d electron (-14.20 eV) which indicates that this narrow band localizes in the Ni 3d atomic orbitals. Since the Ni atoms have unpaired 3d electrons which are also localized in $Ni_{11}As_8$ tetragonal lattice, it is possible that the localized electron configuration is one of the factors of the observed weak ferromagnetic transition at around 20K.

The magnetic entropy change can be evaluated using the Maxwell relation,

$$\Delta S_M = \int_0^H \left(\frac{\partial S}{\partial M}\right)_T dH = \int_0^H \left(\frac{\partial M}{\partial T}\right)_H dH \tag{6.2}$$

In our magnetization measurements, I calculated the magnetic entropy change with approximation,

$$\Delta S_M \left(\frac{T_i + T_{i+1}}{2}\right) = \sum \frac{M_{i+1} - M_i}{T_{i+1} - T_i} \Delta H_i \tag{6.3}$$

As shown in Figure 6.10, the magnetic entropy change under different field are plotted with temperature from 1T to 7T. The magnetic entropy change has the maximum right around the transition temperature. The magnetocaloric effect (MCE) of 14 $mJkg^{-1}T^{-1}$ can be estimated with the maximum value of the magnetic entropy change. The magnetocaloric effect is relatively small compared with other ferromagnetic transition metal arsenide materials.

6.3.6 Grinding study

To confirm our guess, we study the crystalline size effect with grinding both the natural samples and the synthetic powder samples for different periods of time. We broke both the natural and synthetic samples into powder roughly into powder and then measure the X-ray diffraction pattern. Since the synthetic materials are very fragile as I mentioned, we didn't spend a long time grinding them. They broke into powder just by being touched by a tweezer. After the first measurement, we kept rubbing both samples for another 30 minutes and measure them again.

The results were calibrated the instrument broadening using LaB_6 standard. After correction and refinement, the crystallite sizes for the synthetic samples is 202±7 nm at the beginning; and sizes for samples ground for 30 minutes for natural and synthetic ones are 146±7 nm and 127±3nm respectively. As shown in Figure 6.11, we can see that the structure of the sample didn't change. Figure 6.12 presents the zoomed X-ray diffraction pattern, as we can see, the peaks show broadening visually.

TEM results further support our conclusion. For the synthetic sample, the samples without 30 minutes' grinding have very good crystallite and single nanocrystalline electron diffraction pattern as shown in Figure 6.13 (a) and (c). After grinding for 30 min, significant twinning (or dislocation) can be seen on TEM pattern as shown in Figure 6.13 (b), and on the sides of its twinning axis, we can see multiple spots for each reflection (Figure 6.13 (d)). This is proof that after grinding the coherent length was reduced to 5-10 nm, which significantly limited the magnetic

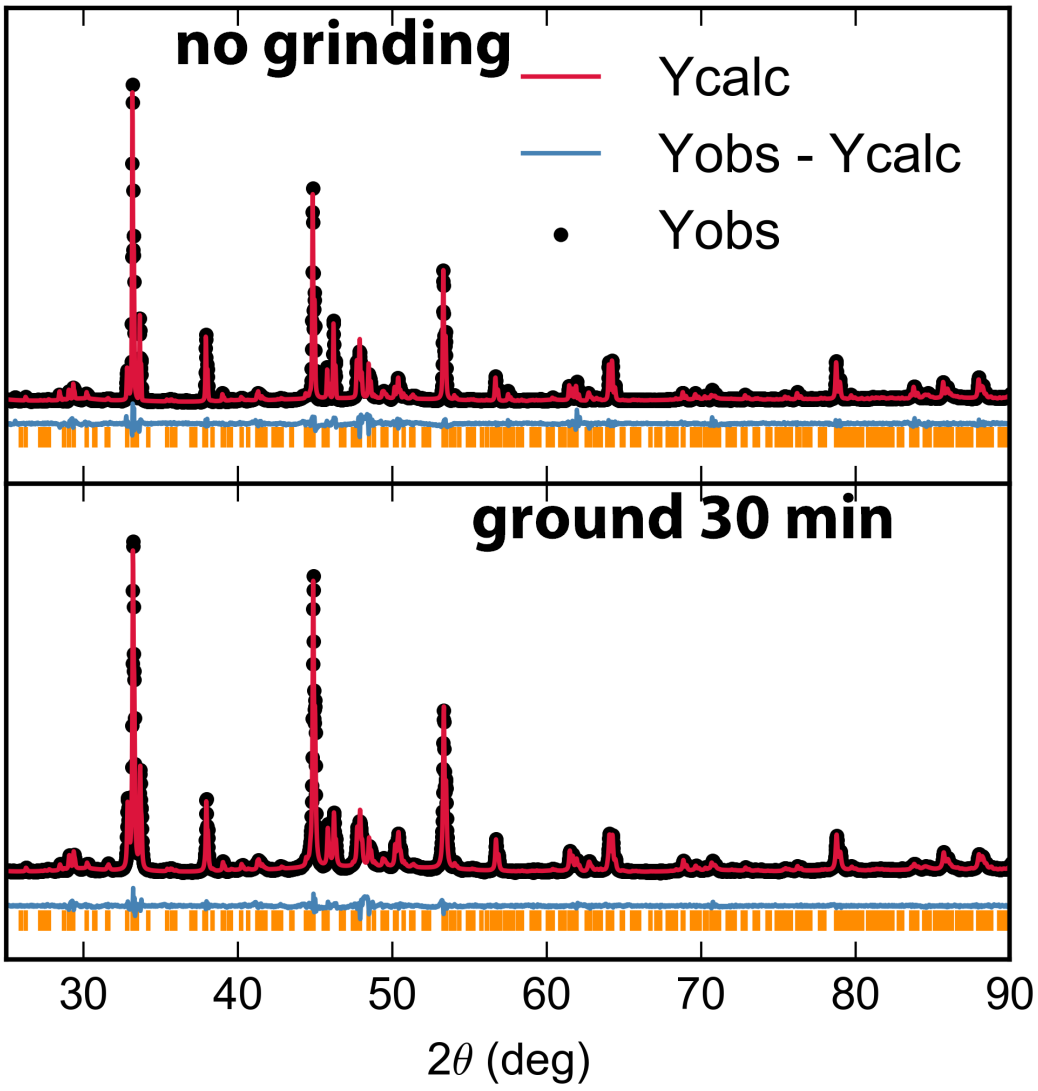

Figure 6.11: The X-ray diffraction patterns of synthetic $Ni_{11}As_8$. The structure didn't change after grinding.

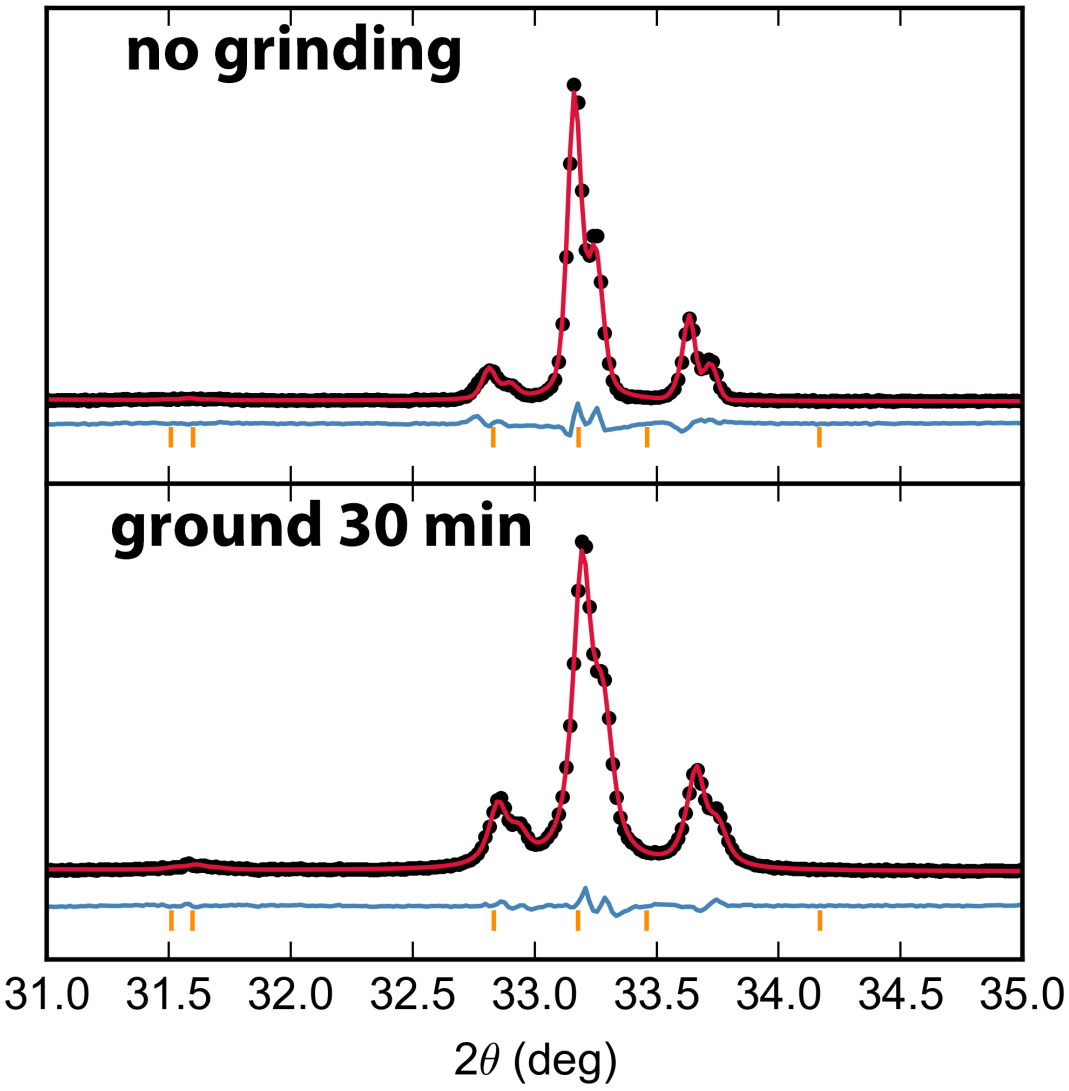

Figure 6.12: The zoomed X-ray diffraction patterns of synthetic $Ni_{11}As_8$. The peacks become broader due to the decreasing size of the nano crystalline.

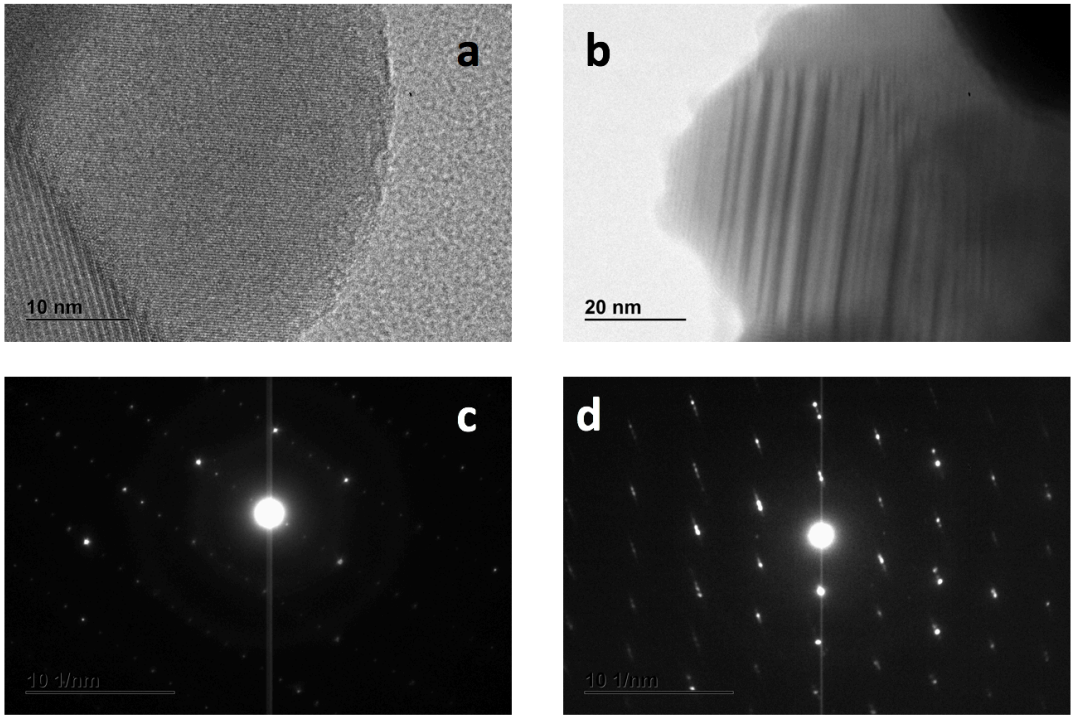

Figure 6.13: TEM patterns of synthetic $Ni_{11}As_8$.

domains.

6.4 Conclusion

In summary, I did several magnetic and transport measurements with natural maucherite poly-crystal samples as well as synthetic poly-crystal powder. A ferromagnetic-like transition is reported in susceptibility data at around 20 K. The negative Curie temperature may due to some antiferromagnetic interactions in the system. Comparing the susceptibility data of natural maucherite, synthetic samples, and previous nanosheet maucherite samples, maucherite show some finite-size scaling properties and is worthy of further investigation. I also study the magnetic

isotherm and found the transition second order. Resistivity and heat capacity were also measured. The magnetic order and transport property are well consistent with the prediction of previous tight-binding band structure calculation. Neutron diffraction experiment was conducted as well on natural materials, but we didnt see any obvious magnetic peaks in the results. It may because the magnetic moment is too weak.

Chapter 7: Other magnetic transitions in natural mineral samples

In this chapter, I will briefly present other mineral samples with magnetic transitions in our measurements. Some of the magnetic transitions are not reported before and are of great interest for further research. Some of the magnetic transitions are published previously but not well studied. Transition metal mineral compounds is a very significant family of compounds for physicists to study. All the samples were characterized by X-ray diffraction, and the magnetic susceptibility measurements have been repeated for at least two times.

7.1 Pyrrhotite (Fe_7S_8)

The natural iron-sulfur compound Pyrrhotite (Fe_7S_8) was extensively investigated during the last several years due to its ferromagnetic phase at room temperature. Another abrupt drop of susceptibility at around 34K was reported fifty years ago, which was used to characterize the mineral [78]. Mössbauer and neutron diffraction experiment has been done, but the magnetic structure of it is still not clear.

The sudden decrease of two orders of magnetization at 34 K (Figure 7.1) was also found in our pyrrhotite sample, like the Verwey transition in Magnetite-

Fe_3O_4 [79]. But the reason for the transition was not well studied. We investigate the transition with transport measurement and found a field independent insulator-metal transition (Figure 7.2) at the transition temperature. The abrupt drop of magnetization is probably due to a superexchange induced ferromagnetic-to-antiferromagnetic transition, which leads to an insulator-metal transition as well. But more experiment has to be done to confirm this assumption. We also measured the magnetization with field under different temperature, which shows some unconventional magnetic order (Figure 7.3). The behavior is similar to the colossal magnetoresistance (CMR) materials.

The neutron scattering and heat capacity measurement was also conducted and confirmed the magnetic transition [80]. Also, the lattice parameter changes dramatically with temperature decreasing. So it is worthy of doing some pressure study and first principle calculation with this material.

7.2 Wittichenite (Cu_3BiS_3)

Wittichenite is an essential material in photovoltaic industry [81], thin films of Cu_3BiS_3 were well applied in solar cells [82]. But the low-temperature properties have not been studied.

We observed an antiferromagnetic transition at 50 K and the susceptibility starts increasing at a lower temperature (Figure 7.4). Above the antiferromagnetic transition, wittichenite is an ordinary insulator, will the resistance saturated below the transition. We made some synthetic ploy-crystalline samples with molten metal

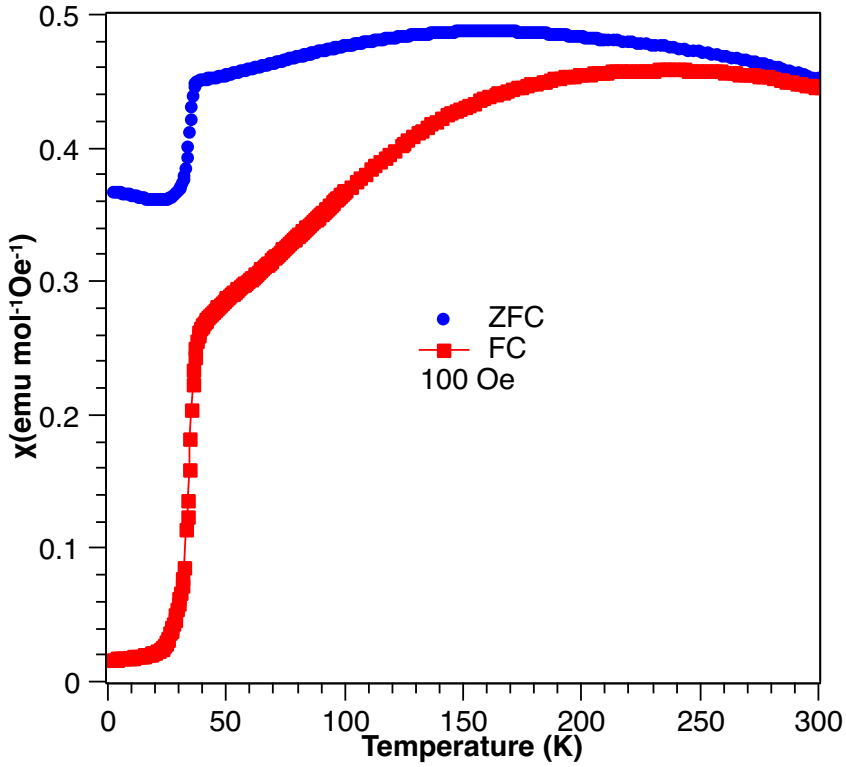

Figure 7.1: The antiferromagnetic transition in our natural pyrrhotite sample. The sudden drop in susceptibility suggests a magnetic order transition.

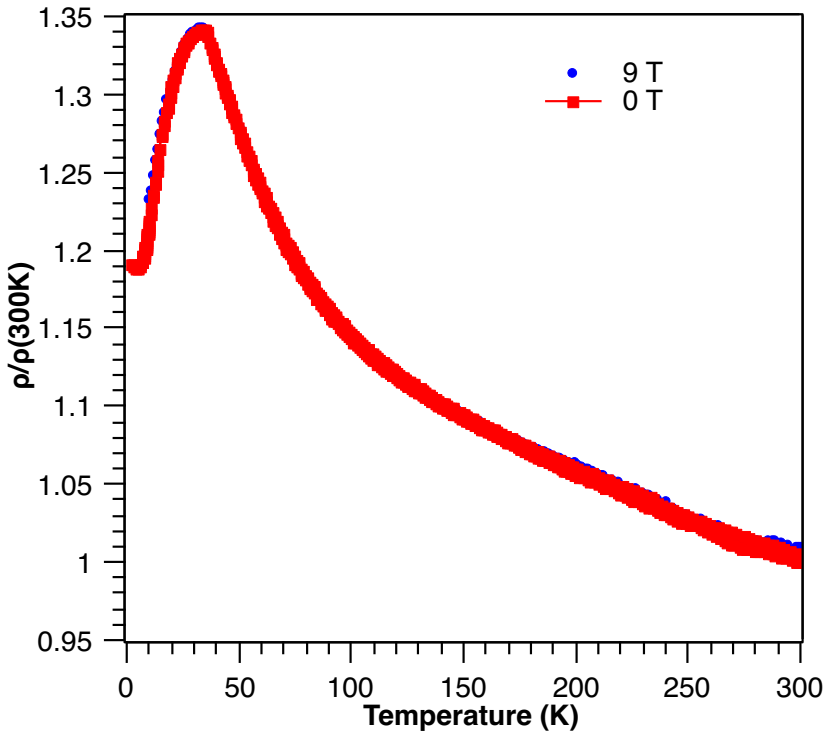

Figure 7.2: Normalized resistance of natural pyrrhotite. There exist an insulator-metal transition around 34 K which is same as the magnetic transition temperature. The transition indicates the itinerant electrons getting rid of the ferromagnetic charge-ordered state, which is very similar to Verwey transition.

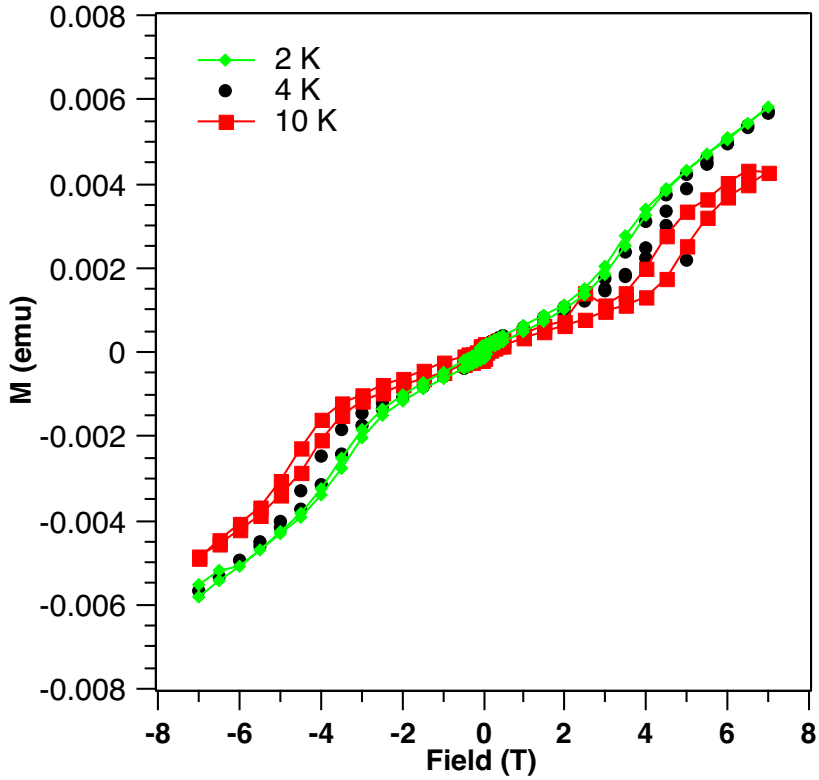

Figure 7.3: Hysteresis scan for a 13.6 mg pyrrhotite sample, the results show some magnetic transition at high field.

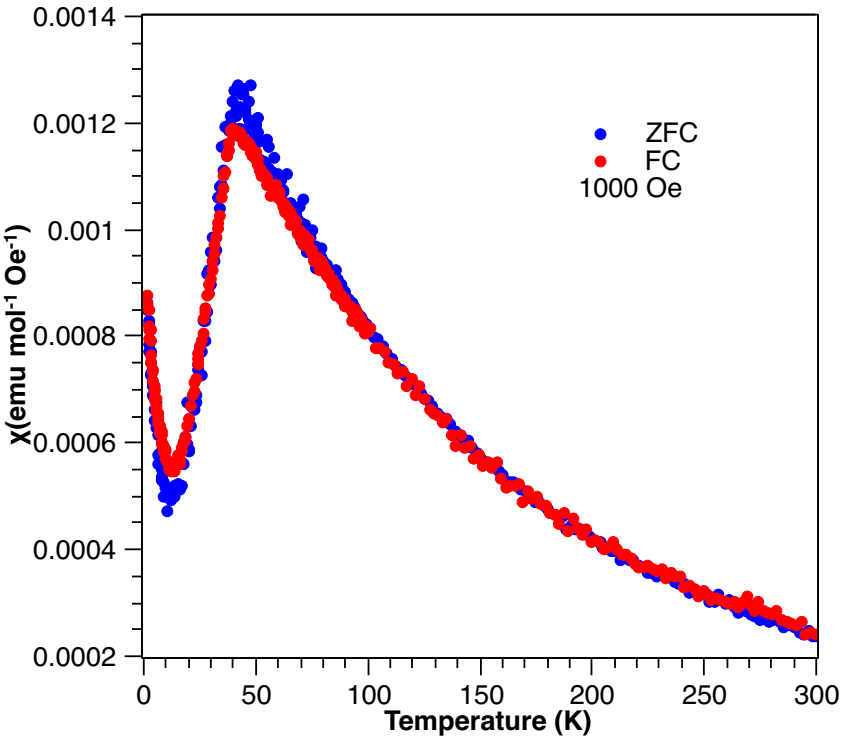

Figure 7.4: Magnetic susceptibility of natural wittichenite.

flux method, but the susceptibility of the synthetic sample followed paramagnetic behavior, and the resistivity was just a typical insulator. The difference between two samples needs to be investigated in the future.

7.3 Chalcostibite $CuSbS_2$

$CuSbS_2$ is also a promising photoelectric material [83]. A lot of experiments have been done on thin film sample in room temperature range, while the low-temperature behavior of bulk sample has not been investigated. We measured susceptibility with changing temperature and observed a magnetic transition at around 25 K (Figure 7.5). The transition hasnt been reported, while no magnetic order was

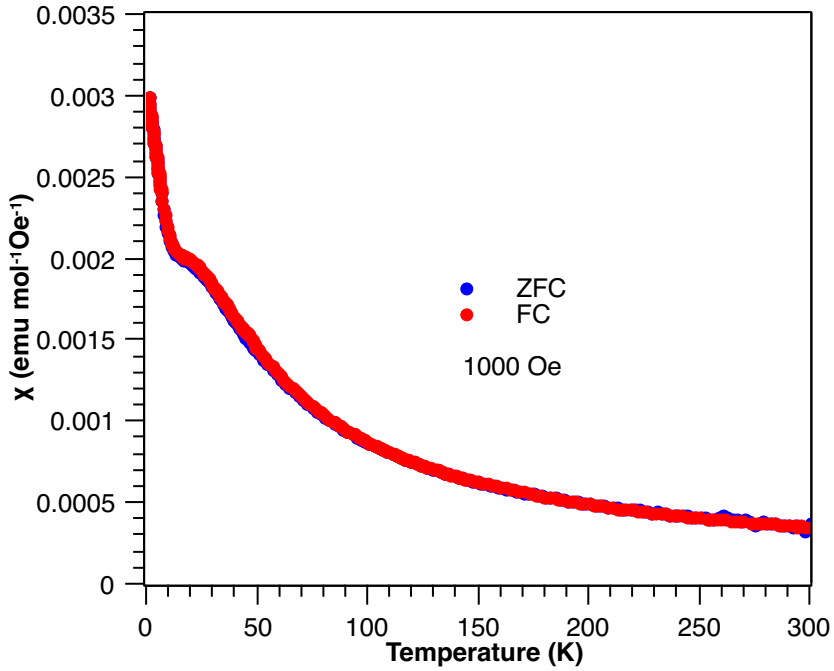

Figure 7.5: Magnetic susceptibility of chalcostibite samples. A small abnormal at around 25 K suggests some unconventional magnetic order.

expected in this material. The resistivity of the mineral shows insulating behavior.

7.4 Akinite ($PbCuBiS_3$)

Akinite ($PbCuBiS_3$) is Copper-Bismuth sulfide with orthorhombic structure and *Pnma* space group. The structure has been confirmed in the 1970s. We measured the susceptibility and resistivity of this mineral sample. The samples show a broad antiferromagnetic peak at around 100K in the susceptibility and metallic behavior in resistivity. Also, we calculated the band structure of akinite, like many other Bi-S materials, akinite may also be a good candidate for photovoltaic material

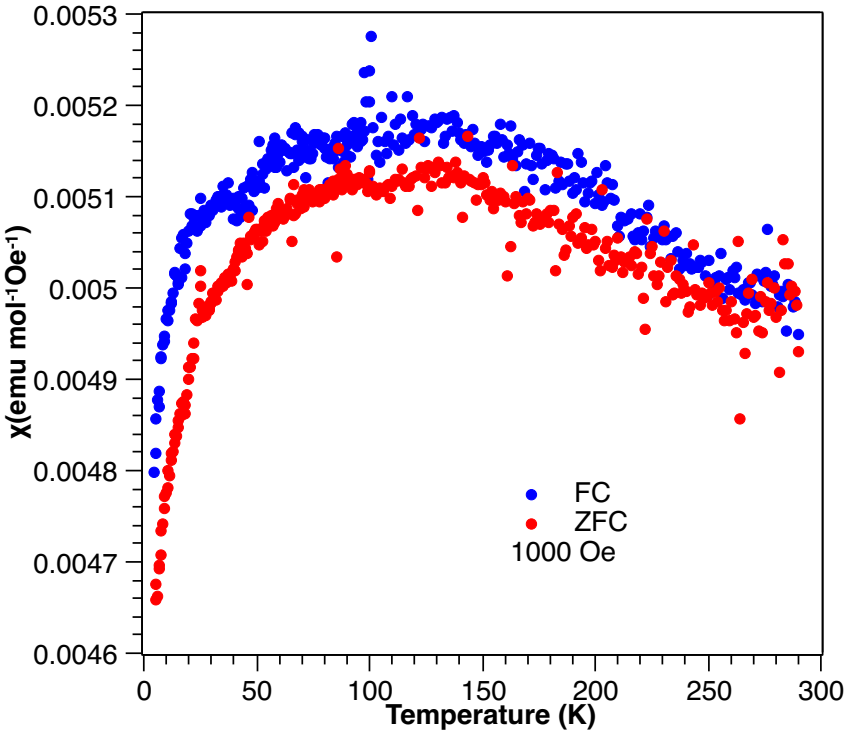

Figure 7.6: Magnetic susceptibility of akinite samples.

similar to Cu_3BiS_3.

7.5 Jamesonite ($Pb_4FeSb_6S_{14}$)

Jamesonite ($Pb_4FeSb_6S_{14}$) was reported as a quasi-one-dimensional spin two Heisenberg chain with monoclinic structure [84, 85]. This system can be regarded as a diluted berthierite ($FeSb_2S_4$). We measure the susceptibility temperature dependence and found an antiferromagnetic transition at 34 K and another two abnormalities at 3 K and 8 K. Our result is consistent with previous research. The 3 K and 8 K transitions havent been well investigated. We measured the resistivity from 150K to 300K which is just normal insulator behavior. According to the the-

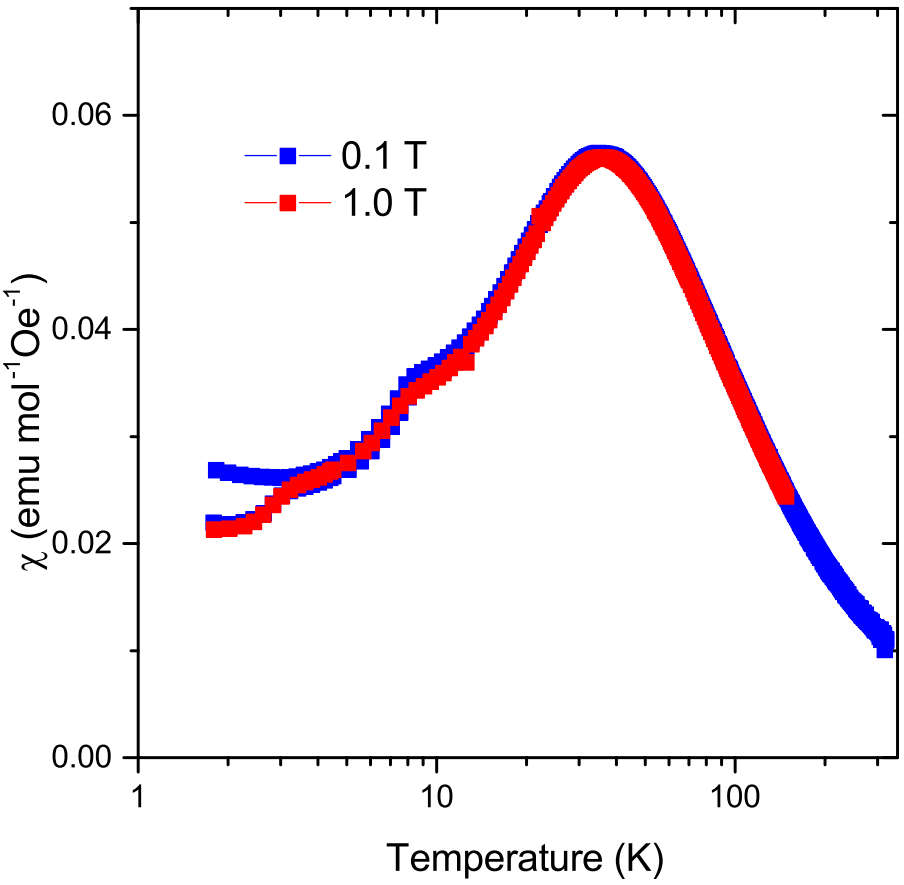

Figure 7.7: Magnetic susceptibility of natural jamesonite in log scale, two other small abnormalities can be found at 3 K and 8 K, the low temperature transitions were not well studied.

ory, jamesonite may also have frustrated magnetic properties. So the heat capacity measurement, M-H curves may reveal more about the 3 K and 8 K abnormalities and the frustrated magnetic properties. Also, neutron diffraction experiment may help us have a better understanding of the two low-temperature transitions.

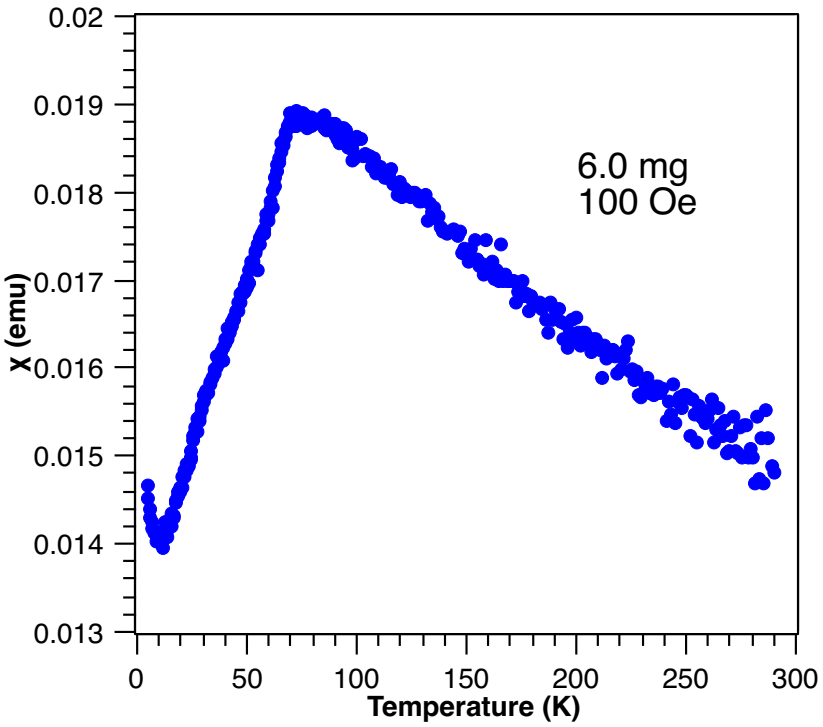

Figure 7.8: Magnetic susceptibility of colusite. Similar to bornite mentioned in chapter 3, colusite also has a antiferromagnetic transition at around 75K.

7.6 Colusite $Cu_{26}V_2(As,Sn,Sb,Ge)_6S_{32}$

Colusite ($Cu_{26}V_2(As,Sn,Sb,Ge)_6S_{32}$) is a natural copper sulfide forms in cubic structure. We discovered an unreported antiferromagnetic transition similar to bornite (Cu_5FeS_4). The magnetic structure of this compound has not been determined. More transport experiments, as well as neutron scattering experiment, will be conducted in the future.

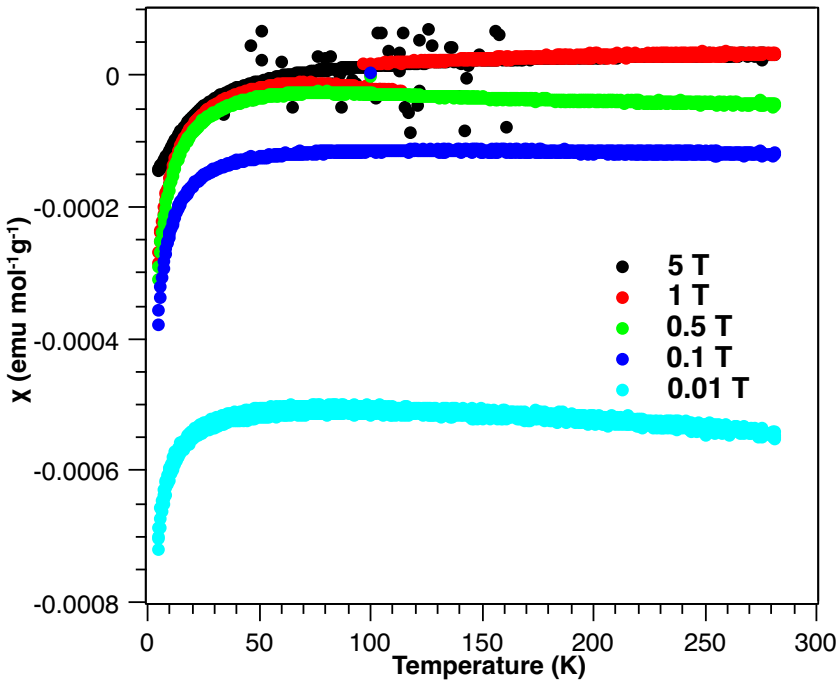

Figure 7.9: Magentic susceptibility of aramayoite under different fields.

7.7 Aramayoite ($Ag(Sb,Bi)S_2$)

Aramayoite is a silver sulfide with triclinic structure. The physical properties of this material have not been studied. We studied the magnetic susceptibility temperature dependence of aramayoite under a different field. We found some field dependence and diamagnetic transition at around 10K. Such transitions were discovered in some sulfides as well, and some of them also have transitions in transport at the corresponding temperature. Only the structure of this material has been reported. There are plenty of experiments to be done for this mineral.

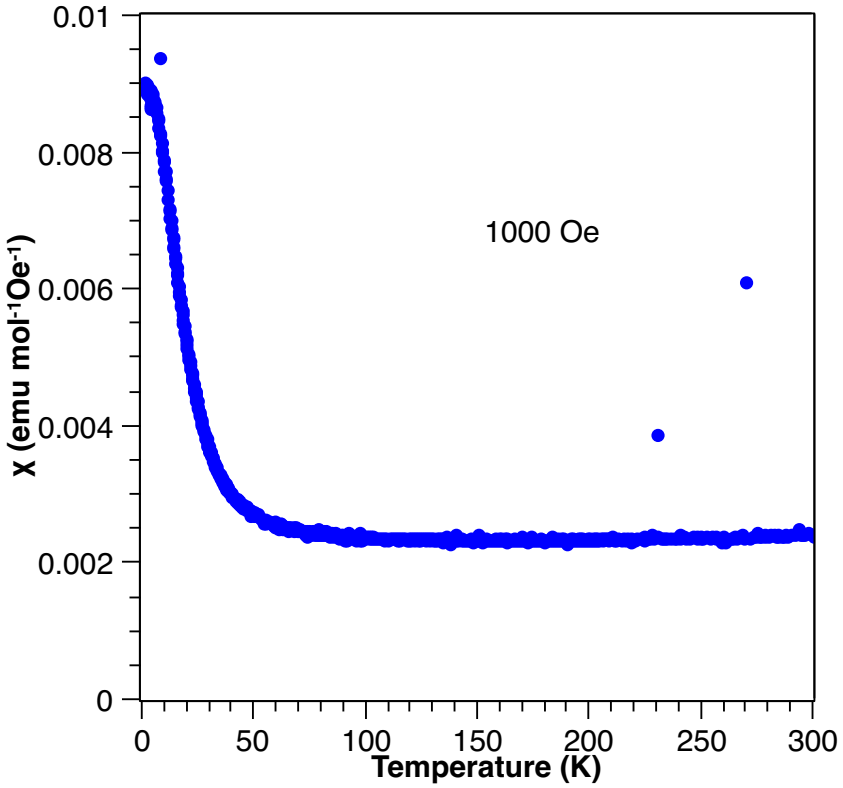

Figure 7.10: Magnetic susceptibility of bismuthnite. The pure Bi_2S_3 are suppose to be non-magnetic, the ferromagnetic may due to some impurities in the mineral samples.

7.8 Bismuthnite (Bi_2S_3)

Bismuthinite (Bi_2S_3) is a bismuth sulfide with orthorhombic structure. We discovered an unexpected ferromagnetic order in a low-temperature range. It may occur due to some impurities in the mineral.

7.9 Cubanite ($CuFe_2S_3$)

Cubanite ($CuFe_2S_3$) is a yellow mineral with orthorhombic structure. We didn't get very nice susceptibility temperature dependence for this mineral, while we discovered a typical ferromagnetic M-H curve at low temperature (below 20 K). The mineral is known as a room temperature ferromagnet [86]. More experiments will be proposed.

7.10 Chalcopyrite ($CuFeS_2$)

Chalcopyrite was reported as a room temperature AFM semiconductor [87]. The magnetic properties have been studied by using DFT calculation. According to the DFT calculation, chalcopyrite is an antiferromagnetic semiconductor. But our susceptibility result is not consistent with the previous computational research. Instead, we found a weak upturn of susceptibility at low temperature. According to the DFT calculation, the system may have some anisotropic phenomenon. More transport experiments will be conducted in the future.

7.11 Stephanite (Ag_5SbS_4)

Stephanite (Ag_5SbS_4) has been studied by NQR spectroscopy from 4.2K to 300 K, and a transition at 140K has been reported [88]. We didnt see the corresponding transition at 140K clearly but found a diamagnetic drop at around 4K.

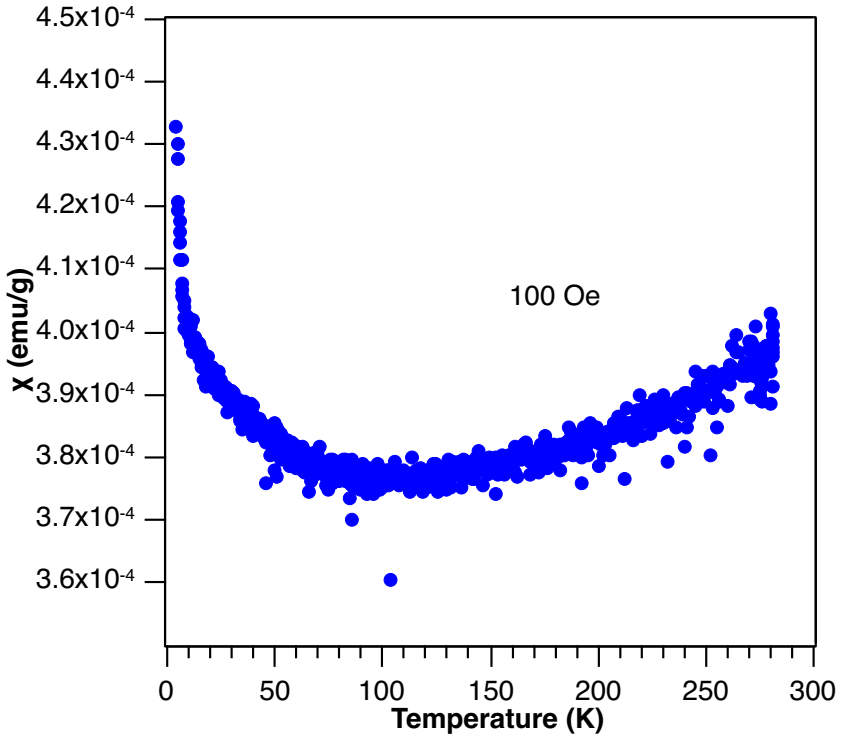

Figure 7.11: Magnetic susceptibility of chalcopytite. A weak increasing is shown in the magnetization when temperature is below 75 K.

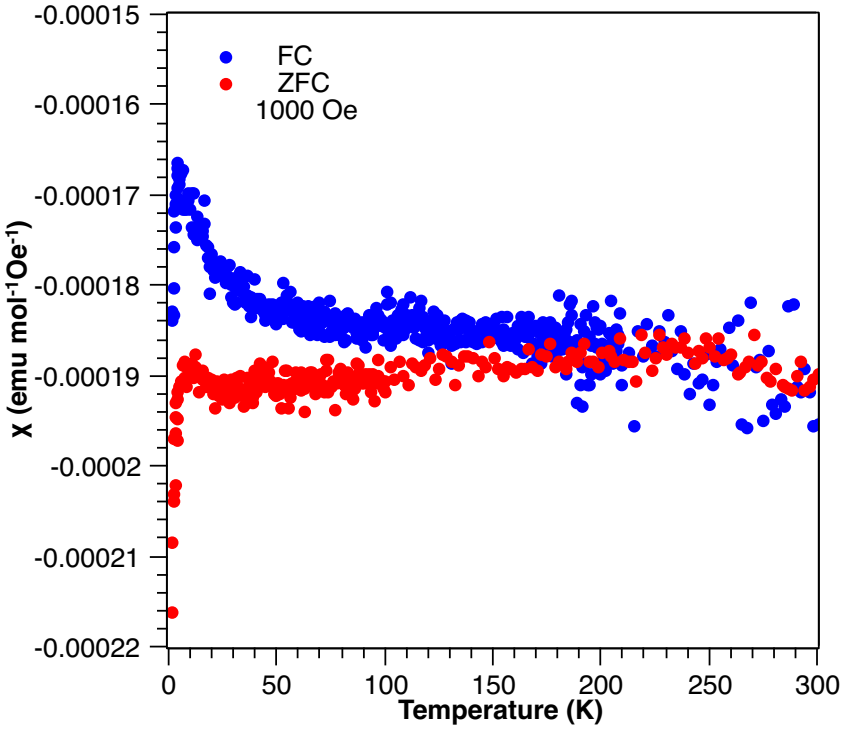

Figure 7.12: Magnetic susceptibility of stephanite. The material is diamagnetic material. The further diamagnetic drop is not clear yet.

7.12 Pseudobrookite (Fe_2TiO_5)

Pseudobrookite is an iron-titanium oxide with orthorhombic structure. We discovered an abnormal drop at around 180K in susceptibility. The magnetic structure has not been well studied.

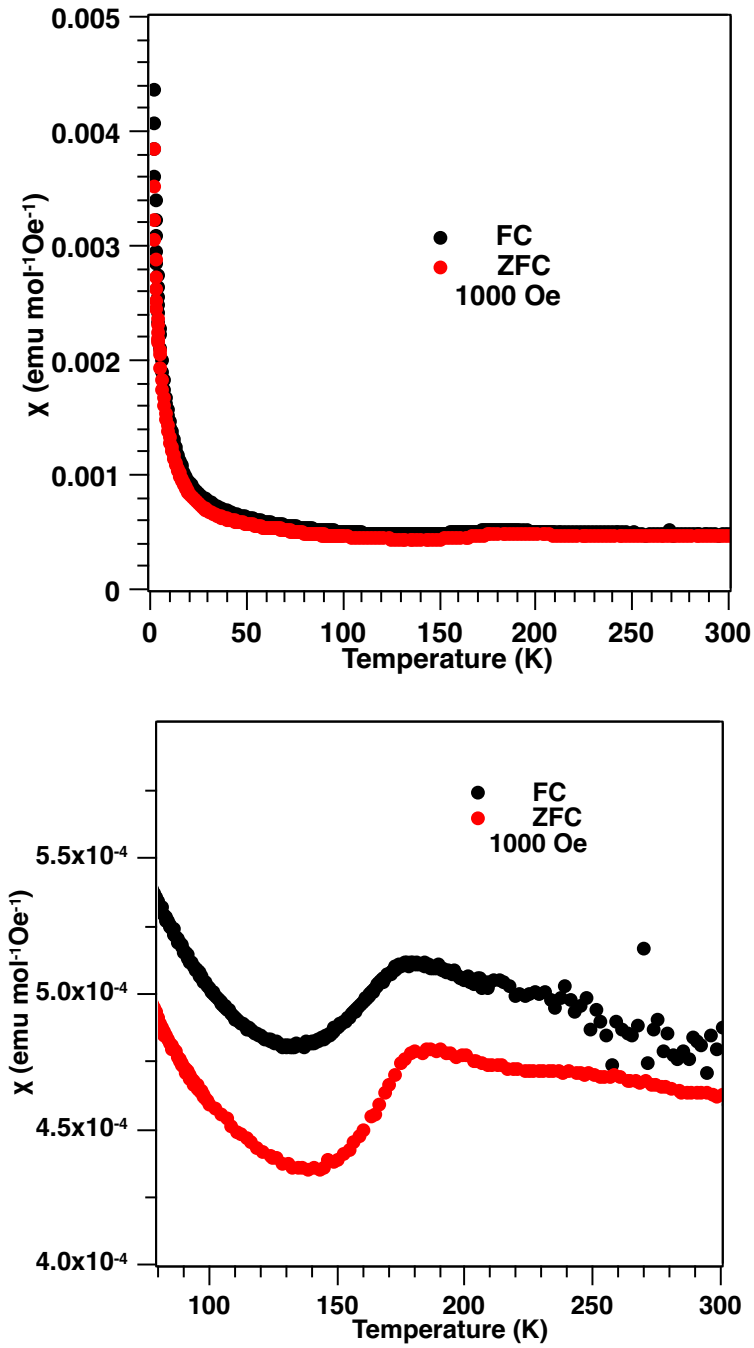

Figure 7.13: Magnetic susceptibility of pseudobrookite. A small drop at around 175 K was detected. There is no report about it.

Chapter 8: Summary and outlook

This chapter attempts to provide a summary of our work. We will make a comparison between our transition metal sulfides and transition metal oxides. We will also present a list of natural minerals that may be worthy of investigation based on our research experience.

8.1 Summary

In summary, we have measured more than 40 mineral samples from Department of Mineral Science, Smithsonian Museum. Over 1/3 of the samples show some magnetic transition. Most of the minerals are transition metal sulfides and arsenides. As the four mineral materials, we discussed in detail in previous sections, as well as the other minerals we presented in the previous section, naturally occurring samples is a fascinating family of materials in many aspects. Besides lots of new magnetic transitions, some of the materials have low dimensional property, some of them show some relation between modern physics concept. Also, the physical properties of the natural compound may be very different from synthetic compounds. More attention should be paid to this family of compounds.

In table 8.1, we make a summary of the magnetic transitions we found in

natural compounds. In table 8.2, we also put the non-magnetic compounds we studied together.

Name	Formula	Structure	Features	Previous work
Bornite	Cu_5FeS_4	orthorhombic	AFM and semiconductor-insulator transition at 74 K	Magnetic structure was studied.
Pyrrhotite	Fe_7S_8	monoclinic	AFM at 34 K	Magnetic structure was studied.
Wittichenite	Cu_3BiS_3	orthorhombic	AFM at 50 K	No research.
Berthierite	$FeSb_2S_4$	orthorhombic	AFM at 70K	Magnetic structure was studied.
Chalcostibite	$CuSbS_2$	orthorhombic	Transition at 25 K	No research.
Nagyagite	$Pb5Au(Te,Sb)_4S_{4-8}$	monoclinic	FM at 37 K	No research.
Akinite	$PbCuBiS_3$	orthorhombic	AFM at 100 K	No research.
Jamesonite	$Pb_4FeSb_6S_{14}$	monoclinic	AFM at 34 K, Transitions at 3 K and 8K	Magnetic structure was studied
Colusite	$Cu_{26}V_2(As,Sn,Sb,Ge)_6S_{32}$	cubic	AFM at 75 K	Not reported.
Aramayoite	$Ag(Sb,Bi)S_2$	triclinic	Diamagnetic drop	Not reported.
Bismuthnite	Bi_2S_3	orthorhombic	FM order	Not reported.
Cubanite	$CuFe_2S_3$	orthorhombic	FM order	Magnetic structure was studied.
Chalcopyrite	$CuFeS_2$	tetragonal	AFM order	Not reported
Stephanite	Ag_5SbS_4	orthorhombic	AFM at 4 K	Not reported
Maucherite	$Ni_{11}As_8$	tetragonal	FM at 20 K	Nanosheet were studied.
Pseudobrookite	Fe_2TiO_5	orthorhombic	AFM at 175 K	Not reported

Table 8.1: A summary of the magnetic transition in the mineral samples we measured.

8.2 Outlook and Future Work

In our measured samples, there are still several new reported magnetic transitions as well as some other interesting materials. More work should be done with these materials. Besides the measured material. We also make a list of mineral compounds that is worthy of investigation.

Arsenosulvanite (Cu_3(As, V)S_4), the structure of arsenosulvanite is very similar to colusite, which has an AFM transition at around 70 K in our experiment.

Mineral Name	Formula	Structure	μ_{eff} (μB)
Pyrargyrite	Ag_3SbS_3	Hexagonal	0.035
Canfieldite	$Ag_8(Ge,Sn)S_6$	Orthorhombic	0.007
Argyrodite	Ag_8GeS_6	Orthorhombic	0.514
Andorite	$AgPbSb_3S_5$	Orthorhombic	0.598
Guanajuatite	$Bi_2(S,Se)_3$	Orthorhombic	0.586
Tetradymite	Bi_2Te_2S	Trigonal	0.578
Enargite	Cu_3AsS_4	Orthorhombic	0.154
Skinnerite	Cu_3SbS_3	Monoclinic	0.389
Pyrite	FeS_2	Isometric	0.049
Metacinnabar	HgS	Cubic	0.059
Millerite	NiS	Trigonal	0.122
Stibnite	Sb_2S_3	Orthorhombic	0.024

Table 8.2: A summary of nonmagnetic natural minerals we measured.

Carrollite ($CuCo_2S_4$) exhibits an antiferromagnetic transition with the Néel temperature at 17 K. The transport property has not been well studied. This mineral is also a good candidate for searching natural superconductivity by chemical doping and pressure because of the similarity with $CuRh_2S_4$, $CuRh_2Se_4$ and CuV_2S_4.

Chromite ($FeCr_2O_4$) is mix-valenced antiferromagnet, and there was not enough research on its transport properties. It is also worthy of a high-pressure experiment.

Coulsonite (FeV_2O_4) is similar to chromite ($FeCr_2O_4$).

Crednerite ($CuMnO_2$) has Mn^{2+} in the system which may have some magnetic

order.

Cuproiriosite ($CuIr_2S_4$) also has a metal insulator transition and is similar to carrollite ($CuCo_2S_4$).

Cuprospinel ($CuFe_2O_4$) is a $A_1B_2O_4$ material with mix-valanced transition metal element.

Daubreelite ($FeAs_2S_4$) is a $A_1B_2S_4$ material similar to $FeSb_2S_4$. The distance between the Fe chain are expected be larger than the distance of $FeSb_2S_4$. It may also exist some low dimensional properties.

Fletcherite ($Cu(Ni, Co)_2S_4$) is a $A_1B_2O_4$ material with mix-valanced transition metal element.

Germanite ($Cu_{26}Ge_4Fe_4S_{32}$) is similar to colusite ($Cu_{26}V_2(As, Sn, Sb)_6S_{32}$) which has a AFM transition.

Gersdorffite (NiAsS) has a similar structure with $PbAs_2$, $NiAs_2$.

Hakite ($(Cu,Hg)_3(Sb,As)(Se,S)_3$) may be good photovoltaic material with similar structure of Cu_3BiS_3.

Hemusite (Cu_6SnMoS_8) may be useful photovoltaic material.

Indite ($FeIr_2S_4$) is a $A_1B_2S_4$ material similar to $FeSb_2S_4$. The distance between the Fe chain are expected be larger than the distance of $FeSb_2S_4$. It may also exist some low dimensional properties.

Kalininite ($CuZn_2S_4$) has the same structure of $CuIr_2S_4$ and $CuCo_2S_4$. An antiferromagnetic transition accompanied with metal-insulator transition may also exist in the material.

Langbanite ($Mn_{13}SbO_{16}(SiO_4)_2$) is a mixe-valenced transition metal compound.

Malanite ($Cu(Pt, Ir)_2S_4$) is similar to the CuX_2S_4 compounds, where X can be Ir, Co, Zn.

Museumite ($Pb_2(Pb,Sb)_2S_8[Te,Au]_2$) has 2-dimensional AuTe layers similar to Nagyagite.

Majakite (PbNiAs) is similar to $PbAs_2$.

Hollandite ($BaMn_8O_{16}$) is a mix-valenced transition metal compounds.

Laihunite ($Fe3(SiO_4)_2$) is a mixed-valenced transition metal compounds.

Garavellite ($FeSbBiS_4$) has similar structure with $FeSb_2S_4$.

Haycockite ($Cu_4Fe_5S_8$) is similar to bornite (Cu_5FeS_4).

The above mineral samples are only small part of all kinds of minerals and even a small part of transition metal sulfide minerals. We pick them out here because they all have very similar properties with the samples we measured.

Also the vast amount of data we collected remind us to study the mineral samples from a statistical approach by using the recently prevalent concept machine learning. There were several significant results about this crossing area. These attempts become very popular recently, especially in some engineering materials. Perhaps in the future, these methods will provide us a better understanding of the relations between minerals and make some predictions about the physical properties of a particular mineral. To use the data more efficiently and to make the project well organized, a mineral physical properties database is also under construction, which will keep records of the name, chemical composition, origin, photos and other experimental results.

Bibliography

[1] Herta Effenberger, Werner H. Paar, Dan Topa, Franz J. Culetto, and Gerald Giester. Toward the crystal structure of nagyagite, [pb(pb,sb)s 2][(au,te)]. *American Mineralogist*, 84(4):669–676, 1999.

[2] WH Paar and TT Chen. Telluride in erzen der gold-lagerstätte schellgaden und vom katschberg-autobahntunnel nord. *Der Karinthin*, 87:371–381, 1982.

[3] CJ Stanley, AC Roberts, and DC Harris. New data for nagyagite. *Mineralogical Magazine*, 58(3):479–482, 1994.

[4] Helmer Fjellvag, Fredrik Grenvøld, Svein Stølen, Arne F Andresen, Reinhold Müller-Käfer, and Arndt Simon. Low-temperature structural distortion in cus. *Zeitschrift für Kristallographie-Crystalline Materials*, 184(1-4):111–122, 1988.

[5] Fritz London and Heinz London. The electromagnetic equations of the supraconductor. In *Proceedings of the Royal Society of London A: Mathematical, Physical and Engineering Sciences*, volume 149, pages 71–88. The Royal Society, 1935.

[6] J. Bardeen, L. N. Cooper, and J. R. Schrieffer. Microscopic Theory of Superconductivity. *Physical Review*, 106:162–164, April 1957.

[7] J. G. Bednorz and K. A. Müller. Possible hightc superconductivity in the balacuo system. *Zeitschrift für Physik B Condensed Matter*, 64(2):189–193, 1986.

[8] M. K. Wu, J. R. Ashburn, C. J. Torng, P. H. Hor, and R. L. Meng. Superconductivity at 93 K in a new mixed-phase Y-Ba-Cu-O compound system at ambient pressure. *Physical Review Letters*, 58:908–910, March 1987.

[9] Yoichi Kamihara, Takumi Watanabe, Masahiro Hirano, and Hideo Hosono. Iron-based layered superconductor la [o1-x f x] feas (x= 0.05- 0.12) with t c= 26 k. *Journal of the American Chemical Society*, 130(11):3296–3297, 2008.

[10] Francesco Di Benedetto, Miria Borgheresi, Andrea Caneschi, Guillaume Chastanet, Curzio Cipriani, Dante Gatteschi, Giovanni Pratesi, Maurizio Romanelli, and Roberta Sessoli. First evidence of natural superconductivity. *European journal of mineralogy*, 18(3):283–287, 2006.

[11] Rikio Settai, Keisuke Katayama, Hiroshi Muranaka, Tetsuya Takeuchi, Arumugam Thamizhavel, Ilya Sheikin, and Y Ōnuki. Superconducting properties in rh 17 s 15 under magnetic field and pressure. *Journal of Physics and Chemistry of Solids*, 71(4):700–703, 2010.

[12] Kazutaka Kudo, Hiroyuki Ishii, Masaya Takasuga, Keita Iba, Seiya Nakano, Jungeun Kim, Akihiko Fujiwara, and Minoru Nohara. Superconductivity induced by breaking te2 dimers of aute2. *Journal of the Physical Society of Japan*, 82(6):063704, 2013.

[13] Johnpierre Paglione and Richard L. Greene. High-temperature superconductivity in iron-based materials. *Nat Phys*, 6(9):645–658, Sep 2010.

[14] M. T. Atanasova, A. M. Strydom, C. J. H. Schutte, L. C. Prinsloo, and W. W. Focke. Crystal structure and magnetic properties of cusb2o4. *Journal of Materials Science*, 49(9):3497–3510, 2014.

[15] Honore Djieutedjeu, Pierre F. P. Poudeu, Nathan J. Takas, Julien P. A. Makongo, Aurelian Rotaru, Kulugammana G. S. Ranmohotti, Clarence J. Anglin, Leonard Spinu, and John B. Wiley. Structural-distortion-driven cooperative magnetic and semiconductor-to-insulator transitions in ferromagnetic fesb2se4. *Angewandte Chemie International Edition*, 49(51):9977–9981, 2010.

[16] Honore Djieutedjeu, Julien P. A. Makongo, Aurelian Rotaru, Andriy Palasyuk, Nathan J. Takas, Xiaoyuan Zhou, Kulugammana G. S. Ranmohotti, Leonard Spinu, Ctirad Uher, and Pierre F. P. Poudeu. Crystal structure, charge transport, and magnetic properties of mnsb2se4. *European Journal of Inorganic Chemistry*, 2011(26):3969–3977, 2011.

[17] Shanming Li, Huaizhou Zhao, Han Zhang, Guangkun Ren, Ning Liu, Dandan Li, Chuansen Yang, Shifeng Jin, Dashan Shang, Wenhong Wang, Yuanhua Lin, Lin Gu, and Xiaolong Chen. Enhancement of the thermoelectric properties of mnsb2se4 through cu resonant doping. *RSC Adv.*, 5:99065–99073, 2015.

[18] A.D. Mukherjee D.G. Nicholson J.T. Southern J.D. Donaldson, A. Kjekshus. *Acta Chem. Scand.*, 26:4063, 1972.

[19] I.G. Kerimov K.K. Mamedov F.Yu. Aliev, A.I. Dzhabbarov.

[20] M. Wintenberger and G. Andr. Magnetic structure of the mineral berthierite fesb2s4. *Physica B: Condensed Matter*, 156:315 – 317, 1989.

[21] T. Hahn M.J. Buerger. *Am. Mineral.*, 40:226, 1955.

[22] Takehiko Oguchi. Exchange interactions in $cu(NH_3)_4so_4{\cdot}h_2o$. *Phys. Rev.*, 133:A1098–A1099, Feb 1964.

[23] T. Ami, M. K. Crawford, R. L. Harlow, Z. R. Wang, D. C. Johnston, Q. Huang, and R. W. Erwin. Magnetic susceptibility and low-temperature structure of the linear chain cuprate sr_2cuo_3. *Phys. Rev. B*, 51:5994–6001, Mar 1995.

[24] K. Caslin, R. K. Kremer, F. S. Razavi, A. Schulz, A. Muñoz, F. Pertlik, J. Liu, M.-H. Whangbo, and J. M. Law. Characterization of the spin-$\frac{1}{2}$ linear-chain ferromagnet $cuas_2o_4$. *Phys. Rev. B*, 89:014412, Jan 2014.

[25] P. Hohenberg and W. Kohn. Inhomogeneous electron gas. *Phys. Rev.*, 136:B864–B871, Nov 1964.

[26] W. Kohn and L. J. Sham. Quantum density oscillations in an inhomogeneous electron gas. *Phys. Rev.*, 137:A1697–A1705, Mar 1965.

[27] G. Kresse. *Title*. PhD thesis, Technische Universiät Wien, 1993.

[28] G. Kresse and J. Hafner. *Ab initio* molecular dynamics for liquid metals. *Phys. Rev. B*, 47:558–561, January 1993.

[29] G. Kresse and J. Furthmüller. Efficiency of ab-initio total energy calculations for metals and semiconductors using a plane-wave basis set. *Comput. Mater. Sci.*, 6(1):15 – 50, 1996.

[30] G. Kresse and J. Furthmüller. Efficient iterative schemes for *ab initio* total-energy calculations using a plane-wave basis set. *Phys. Rev. B*, 54:11169–11186, October 1996.

[31] P. E. Blöchl. Projector augmented-wave method. *Phys. Rev. B*, 50:17953–17979, December 1994.

[32] John P. Perdew, Kieron Burke, and Matthias Ernzerhof. Generalized gradient approximation made simple. *Phys. Rev. Lett.*, 77:3865–3868, October 1996.

[33] Hendrik J. Monkhorst and James D. Pack. Special points for brillouin-zone integrations. *Phys. Rev. B*, 13:5188–5192, June 1976.

[34] M. Y. Choi, P. M. Chaikin, S. Z. Huang, P. Haen, E. M. Engler, and R. L. Greene. Effect of radiation damage on the metal-insulator transition and low-temperature transport in the tetramethyltetraselenofulvalinium pf_6 salt $[(TMTSF)_2pf_6]$. *Phys. Rev. B*, 25:6208–6217, May 1982.

[35] S. S.P. Parkin, D. Jerome, and K. Bechgaard. Pressure dependence of the metal-insulator and superconducting phase transitions in (tmtsf)2 reo4. *Molecular Crystals and Liquid Crystals*, 79(1):569–580, 1982.

[36] Masatoshi Imada, Atsushi Fujimori, and Yoshinori Tokura. Metal-insulator transitions. *Rev. Mod. Phys.*, 70:1039–1263, Oct 1998.

[37] Nevill Francis Mott and L Friedman. Metal-insulator transitions in vo2, ti2o3 and ti2-x v x o3. *Philosophical Magazine*, 30(2):389–402, 1974.

[38] M. Marezio, D.B. McWhan, P.D. Dernier, and J.P. Remeika. Structural aspects of the metal-insulator transitions in ti4o7. *Journal of Solid State Chemistry*, 6(2):213 – 221, 1973.

[39] Shoichi Nagata, Takatsugu Hagino, Yoshitaka Seki, and Teruo Bitoh. Metal-insulator transition in thiospinel cuir2s4. *Physica B: Condensed Matter*, 194:1077 – 1078, 1994.

[40] Pankaj Poddar, Tcipi Fried, and Gil Markovich. First-order metal-insulator transition and spin-polarized tunneling in fe_3o_4 nanocrystals. *Phys. Rev. B*, 65:172405, Apr 2002.

[41] FA Chudnovskii, LL Odynets, AL Pergament, and GB Stefanovich. Electroforming and switching in oxides of transition metals: The role of metal–insulator transition in the switching mechanism. *Journal of Solid State Chemistry*, 122(1):95–99, 1996.

[42] M. S. Jagadeesh, H. M. Nagarathna, P. A. Montano, and M. S. Seehra. Magnetic and mössbauer studies of phase transitions and mixed valences in bornite ($cu_{4.5}fe_{1.2}s_{4.7}$). *Phys. Rev. B*, 23:2350–2356, Mar 1981.

[43] M. F. Collins, G. Longworth, and M. G. Townsend. Magnetic structure of bornite, cu5fes4. *Canadian Journal of Physics*, 59(4):535–539, 1981.

[44] N Morimoto. Structure of two polymorphic forms of cu5fes4. *Acta Crystallographica*, 17(4):351–360, 1964.

[45] KICHIRO Koto and NOBUO Morimoto. Superstructure investigation of bornite, cu5fes4, by the modified partial patterson function. *Acta Crystallographica Section B: Structural Crystallography and Crystal Chemistry*, 31(9):2268–2273, 1975.

[46] Y Kanazawa, K Koto, and N Morimoto. Bornite (cu 5 fes 4); stability and crystal structure of the intermediate form. *The Canadian Mineralogist*, 16(3):397–404, 1978.

[47] Richard A Robie, Robert R Seal, and Bruce S Hemingway. Heat capacity and entropy of bornite (cu 5 fes 4) between 6 and 760 k and the thermodynamic properties of phases in the system cu-fe-s. *The Canadian Mineralogist*, 32(4):945–956, 1994.

[48] Sasikala Devi Assa Aravindh, Udo Schwingenschloegl, and Iman S Roqan. Defect induced d0 ferromagnetism in a zno grain boundary. *The Journal of Chemical Physics*, 143(22):224703, 2015.

[49] W Prellier, A Fouchet, and B Mercey. Oxide-diluted magnetic semiconductors: a review of the experimental status. *Journal of Physics: Condensed Matter*, 15(37):R1583, 2003.

[50] Siddhartha Mal, Tsung-Han Yang, Chunming Jin, Sudhakar Nori, J. Narayan, and J.T. Prater. d0 ferromagnetism in undoped zno thin films: Effect of thickness, interface and oxygen annealing. *Scripta Materialia*, 65(12):1061 – 1064, 2011.

[51] J.M.D. Coey. ferromagnetism. *Solid State Sciences*, 7(6):660 – 667, 2005. A tribute to Erwin Felix Bertaut.

[52] K. v. Klitzing, G. Dorda, and M. Pepper. New method for high-accuracy determination of the fine-structure constant based on quantized hall resistance. *Phys. Rev. Lett.*, 45:494–497, Aug 1980.

[53] Markus König, Steffen Wiedmann, Christoph Brüne, Andreas Roth, Hartmut Buhmann, Laurens W. Molenkamp, Xiao-Liang Qi, and Shou-Cheng Zhang. Quantum spin hall insulator state in hgte quantum wells. *Science*, 318(5851):766–770, 2007.

[54] Lei Fang, Jino Im, Constantinos C. Stoumpos, Fengyuan Shi, Vinayak Dravid, Maxime Leroux, Arthur J. Freeman, Wai-Kwong Kwok, Duck Young Chung, and Mercouri Kanatzidis. Two-dimensional mineral [pb2bis3][aute2]: High-mobility charge carriers in single-atom-thick layers. *Journal of the American Chemical Society*, 137(6):2311–2317, 2015. PMID: 25612093.

[55] DeGottardi W et al. Fang L, Im J. Large spin-orbit coupling and helical spin textures in 2d heterostructure [pb2bis3][aute2]. *Scientific Reports*, 6:35313, 2016.

[56] Gareth L. Nealon, Bertrand Donnio, Romain Greget, Jean-Paul Kappler, Emmanuel Terazzi, and Jean-Louis Gallani. Magnetism in gold nanoparticles. *Nanoscale*, 4:5244–5258, 2012.

[57] B. K. Banerjee. On a generalised approach to first and second order magnetic transitions. *Physics Letters*, 12:16–17, September 1964.

[58] Yoichi Kamihara, Takumi Watanabe, Masahiro Hirano, and Hideo Hosono. Iron-based layered superconductor la[o1-xfx]feas (x = 0.050.12) with tc = 26 k. *Journal of the American Chemical Society*, 130(11):3296–3297, 2008. PMID: 18293989.

[59] Hiroki Takahashi, Kazumi Igawa, Kazunobu Arii, Yoichi Kamihara, Masahiro Hirano, and Hideo Hosono. Superconductivity at 43[thinsp]k in an iron-based layered compound lao1-xfxfeas. *Nature*, 453(7193):376–378, May 2008.

[60] Bayrammurad Saparov, Jonathan E Mitchell, and Athena S Sefat. Properties of binary transition-metal arsenides (t as). *Superconductor Science and Technology*, 25(8):084016, 2012.

[61] D. J. Campbell, C. Eckberg, K. Wang, H. Hodovanets, D. Graf, D. Parker, and J. Paglione. Quantum Oscillations in the Anomalous Spin Density Wave State of FeAs. *ArXiv e-prints*, March 2017.

[62] A. Kallel, H. Boller, and E.F. Bertaut. Helimagnetism in mnp-type compounds: Mnp, fep, cras and cras1xsbx mixed crystals. *Journal of Physics and Chemistry of Solids*, 35(9):1139 – 1152, 1974.

[63] Wei Wu, Jinguang Cheng, Kazuyuki Matsubayashi, Panpan Kong, Fukun Lin, Changqing Jin, Nanlin Wang, Yoshiya Uwatoko, and Jianlin Luo. Superconductivity in the vicinity of antiferromagnetic order in cras. *Nature Communications*, 5:5508 EP –, Nov 2014. Article.

[64] Leticia Tocado, E. Palacios, and R. Burriel. Adiabaticmeasurement of the giant magnetocaloric effect in mnas. *Journal of Thermal Analysis and Calorimetry*, 84(1):213–217, 2006.

[65] Daigorou Hirai, Tomohiro Takayama, Daisuke Hashizume, and Hidenori Takagi. Metal-insulator transition and superconductivity induced by rh doping in the binary pnictides ru*pn* (*pn* = P, as, sb). *Phys. Rev. B*, 85:140509, Apr 2012.

[66] Hongming Weng, Chen Fang, Zhong Fang, B. Andrei Bernevig, and Xi Dai. Weyl semimetal phase in noncentrosymmetric transition-metal monophosphides. *Phys. Rev. X*, 5:011029, Mar 2015.

[67] R. A. Yund. Phase relations in the system ni-as. *Economic Geology*, 56(7):1273, 1961.

[68] Shuo Wei, Jun Lu, Weichao Yu, Houbo Zhang, and Yitai Qian. Ni11as8 single-crystalline nanosheets via hydrothermal redox route. *Inorganic Chemistry*, 44(11):3844–3849, 2005. PMID: 15907109.

[69] Michael E. Fleet. The crystal structure of maucherite (ni11as8). *American Mineralogist*, 58:203–210, 1973.

[70] Emil Makovicky and Stefano Merlino. Od (order-disorder) character of the crystal structure of maucherite ni8as11. *European Journal of Mineralogy*, 21(4), 2009.

[71] Z. X. Tang, C. M. Sorensen, K. J. Klabunde, and G. C. Hadjipanayis. Size-dependent curie temperature in nanoscale $mnfe_2o_4$ particles. *Phys. Rev. Lett.*, 67:3602–3605, Dec 1991.

[72] J. P. Chen, C. M. Sorensen, K. J. Klabunde, G. C. Hadjipanayis, E. Devlin, and A. Kostikas. Size-dependent magnetic properties of mnfe$_2$o$_4$ fine particles synthesized by coprecipitation. *Phys. Rev. B*, 54:9288–9296, Oct 1996.

[73] Yinglin Liu, Zainovia Lockman, Azizan Aziz, and Judith MacManus-Driscoll. Size dependent ferromagnetism in cerium oxide (ceo 2) nanostructures independent of oxygen vacancies. *Journal of Physics: Condensed Matter*, 20(16):165201, 2008.

[74] Won Seok Seo, Hyong Hoon Jo, Kwangyeol Lee, Bongsoo Kim, Sang Jun Oh, and Joon T. Park. Size-dependent magnetic properties of colloidal mn3o4 and mno nanoparticles. *Angewandte Chemie*, 116(9):1135–1137, 2004.

[75] L. Vitos, B. Johansson, and J. Kollár. Size-dependent paramagnetic-ferromagnetic phase transition in palladium clusters. *Phys. Rev. B*, 62:R11957–R11960, Nov 2000.

[76] Xiaoyong Xu, Chunxiang Xu, Jun Dai, Jingguo Hu, Fengji Li, and Sam Zhang. Size dependence of defect-induced room temperature ferromagnetism in undoped zno nanoparticles. *The Journal of Physical Chemistry C*, 116(15):8813–8818, 2012.

[77] Michael E. Fisher and Michael N. Barber. Scaling theory for finite-size effects in the critical region. *Phys. Rev. Lett.*, 28:1516–1519, Jun 1972.

[78] Pierre Rochette, Gérard Fillion, Jean-Luc Mattéi, and Marinus J Dekkers. Magnetic transition at 30–34 kelvin in pyrrhotite: insight into a widespread occurrence of this mineral in rocks. *Earth and Planetary Science Letters*, 98(3-4):319–328, 1990.

[79] Ricardo Aragón, Douglas J. Buttrey, John P. Shepherd, and Jurgen M. Honig. Influence of nonstoichiometry on the verwey transition. *Phys. Rev. B*, 31:430–436, Jan 1985.

[80] Anthony V Powell, Paz Vaqueiro, Kevin S Knight, Laurent C Chapon, and Rodolfo D Sánchez. Structure and magnetism in synthetic pyrrhotite fe 7 s 8: A powder neutron-diffraction study. *Physical Review B*, 70(1):014415, 2004.

[81] Mukesh Kumar and Clas Persson. Cu3bis3 as a potential photovoltaic absorber with high optical efficiency. *Applied Physics Letters*, 102(6):062109, 2013.

[82] M.V. Yakushev, P. Maiello, T. Raadik, M.J. Shaw, P.R. Edwards, J. Krustok, A.V. Mudryi, I. Forbes, and R.W. Martin. Electronic and structural characterisation of cu3bis3 thin films for the absorber layer of sustainable photovoltaics. *Thin Solid Films*, 562:195 – 199, 2014.

[83] Bo Yang, Liang Wang, Jun Han, Ying Zhou, Huaibing Song, Shiyou Chen, Jie Zhong, Lu Lv, Dongmei Niu, and Jiang Tang. Cusbs2 as a promising

earth-abundant photovoltaic absorber material: a combined theoretical and experimental study. *Chemistry of Materials*, 26(10):3135–3143, 2014.

[84] N NIIZEKI and MJ Buerger. The crystal structure of jamesonite, fepb4sb6s14. *Zeitschrift für Kristallographie-Crystalline Materials*, 109(1-6):161–183, 1957.

[85] Yoshitaka Matsushita and Yutaka Ueda. Structure and physical properties of 1d magnetic chalcogenide, jamesonite (fepb4sb6s14). *Inorganic chemistry*, 42(24):7830–7838, 2003.

[86] T Szymański. A refinement of the structure of cubanite, cufe2s3. *Zeitschrift für Kristallographie-Crystalline Materials*, 140(3-4):218–239, 1974.

[87] Sergio Conejeros, Pere Alemany, Miquel Llunell, Iberio de PR Moreira, Vıctor Sanchez, and Jaime Llanos. Electronic structure and magnetic properties of cufes2. *Inorganic chemistry*, 54(10):4840–4849, 2015.

[88] A Yu Orlova, RR Gainov, AV Dooglav, IN Penkov, and EA Korolev. Structure and transport properties of stephanite (ag 5 sbs 4) according to antimony nuclear quadrupole resonance. *JETP letters*, 96(6):370–374, 2012.